DARK MATTER IN THE MILKY WAY DISC

Dissertation

zur

Erlangung der naturwissenschaftlichen Doktorwürde
(Dr. sc. nat.)

vorgelegt der

Mathematisch-naturwissenschaftlichen Fakultät

der

Universität Zürich

von

Silvia Garbari

aus

Italien

Promotionskomitee

Prof. Dr. George Lake (Vorsitz)
Prof. Dr. Justin I. Read
Dr. Prasenjit Saha

Zürich, 2012

Contents

Summary

The local dark matter density ($\rho_{\rm dm}$) is the average density in a small volume around the Sun. This quantity is interesting for two key reasons: to predict the flux of dark matter particles in laboratory detectors and – in combination with the rotation curve – to provide constraints on the Galactic halo shape, giving constraints on cosmology and on the assembly history of the Milky Way.

We use – for the first time – a high resolution N-body simulation of a Milky Way like galaxy to find systematic errors in determining the local dark matter density from the vertical kinematics of stars. We find that the techniques in the literature – based on the hypothesis of a separable distribution function for the stars – are highly biased. We introduce a new method that uses moments of the Jeans equations and marginalises over the unknown parameters. Given sufficiently good data, we show that it recovers the correct local dark matter density even in the face of disc inhomogeneities, non-isothermal tracers and a non-separable distribution function.

We apply our new method to rejuvenated data from the literature, obtaining a new determination of the local dark matter density: $\rho_{\rm dm} = 0.022^{+0.015}_{-0.013}$ $\rm M_{\odot}pc^{-3}$ ($0.85^{+0.57}_{-0.50}\,\rm GeV\,cm^{-3}$). We perform a series of tests to demonstrate insensitivity to plausible systematic errors in our distance calibration. We find that $\rho_{\rm dm}$ is larger than the canonical value, and mildly in tension with extrapolations from the rotation curve that assume a spherical halo. Despite our large error bars, our new value for $\rho_{\rm dm}$ has interesting implications. It implies a larger flux of dark matter particles and therefore a greater chance of detection. Also, if confirmed by better data, this large value of $\rho_{\rm dm}$ means that the halo of our Galaxy is oblate and/or that we have a disc of dark matter in the Galaxy, as predicted by recent cosmological simulations.

Finally we present an ongoing project, aiming to map the dark matter density at different position in the Milky Way disc. We use N-body simulations of galaxy mergers to test the performance of our new method at different radial positions in the Galactic disc and to study the detectability of the possible presence of a dark matter disc. Then we present a suitable sample of tracers that will be analysed to map $\rho_{\mathrm{dm}}(R)$. We choose Red Clump stars from the the PPMXL catalogue, since these are good natural distance indicators. The preliminary analysis of the simulations shows that the method recovers the dark matter density in the Galactic even at larger radii, where the disc is more affected by the presence of non-equilibrium features (flares and warps) and is more sensitive to the presence of a dark disc.

Zusammenfassung

Die lokale Dichte Dunkler Materie (ρ_{dm}) ist die durchschnittliche Dichte an Dunkler Materie in einem kleinen Volumen um die Sonne. Diese Grösse ist aus zwei wichtigen Gründen interessant: um den Fluss von Teilchen Dunkler Materie in Laborexperimenten vorherzusagen, und um – in Kombination mit der Rotationskurve – Einschränkungen zur Form des galaktischen Halos und daraus zur Kosmologie und der Aufbaugeschichte der Milchstrasse zu erhalten.

Wir nutzen – zum ersten Mal – eine hochaufgelöste N-Körper-Simulation einer Galaxie ähnlich der Milchstrasse um systematische Fehler zu bestimmen, die auftreten, wenn die lokale Dichte Dunkler Materie aus der Bewegung von Sternen vertikal zur Milchstrassenscheibe berechnet wird. Wir finden, dass die Techniken in der Literatur – basierend auf der Annahme, dass die Sterne eine separierbare Distributionsfunktion besitzen – in hohem Masse verzerrt sind. Wir führen eine neue Methode ein, welche Momente der Jeans-Gleichungen benutzt und über die unbekannten Parameter marginalisiert. Wir zeigen, dass sie mit genügend qualitativen Daten die korrekte lokale Dichte Dunkler Materie zurückgewinnt, auch unter erschwerten Bedingungen wie Scheiben-Inhomogenitäten, nicht isothermalen Indikatorsternen und einer nicht separierbaren Distributionsfunktion.

Wir wenden unsere neue Methode auf regenerierte Daten aus der Literatur an, und bestimmen damit die lokale Dichte Dunkler Materie neu: $\rho_{\mathrm{dm}} = 0.022^{+0.015}_{-0.013}$ $\mathrm{M}_{\odot}\mathrm{pc}^{-3}$ ($0.85^{+0.57}_{-0.50}\,\mathrm{GeV\,cm}^{-3}$). Wir führen eine Reihe von Tests durch, um die Unempfindlichkeit gegenüber plausiblen systematischen Fehlern in der Abstandskalibration zu demonstrieren. Wir finden, dass ρ_{dm} grösser ist als der allgemein akzeptierte Wert, und leicht unterschiedlich von Extrapolationen der Rotationskurve, wenn ein sphärischer Halo angenommen wird. Trotz der grossen Fehler hat unser neuer Wert für ρ_{dm} interessante Auswirkungen. Er impliziert einen grösseren Fluss von Teilchen Dunkler Materie und damit eine grössere Wahrscheinlichkeit für Detektionen. Darüberhinaus, wenn dieser Wert von besseren Daten bestätigt wird, bedeutet dieser hohe Wert von $\rho_{\rm dm}$, dass der Halo unserer Galaxie eine oblate Gestalt annimmt und/oder dass eine Scheibe aus Dunkler Materie in der Milchstrasse existiert, wie von jüngsten kosmologischen Simulationen vorhergesagt wird.

Schlussendlich präsentieren wir ein laufendes Projekt, das darauf abzielt, die Dichte Dunkler Materie an verschiedenen Orten der Milchstrassen-Scheibe zu bestimmen. Wir benutzen N-Körper-Simulationen von Galaxienfusionen um die Effizienz unserer neuen Methode an verschiedenen Orten der galaktischen Scheibe und die Detektierbarkeit einer möglichen Scheibe aus Dunkler Materie zu untersuchen. Wir präsentieren anschliessend eine passende Auswahl von Indikatorsternen, die analysiert werden, um $\rho_{\rm dm}$ zu kartografieren. Wir wählen Rote-Haufen-Sterne aus dem PPMXL-Katalog, da diese gute natürliche Distanzindikatoren darstellen. Die vorläufige Analyse der Simulationen zeigt, dass unsere Methode die Dichte Dunkler Materie in der galaktischen Scheibe sogar bei grösseren Radien wiedergewinnt, wo die Scheibe eher von Nicht-Gleichgewichts-Phänomenen (Flares und Warps) beeinflusst wird und empfindlicher gegenüber der Präsenz einer Dunklen Scheibe ist.

Chapter 1

Introduction

Dark matter constitutes about the 80% of all the gravitating matter in the Universe. It plays a central role in structure formation and galaxy evolution and its existence is inferred by its dynamical influence on a wide range of scales (see Section 1.1.1). While its nature remains elusive, dark matter is most likely a new particle of nature (see Section 1.1.2), rather than a modification of Newtonian gravity (see Section 1.1.3). Several experiments are currently underway to detect dark matter particles both directly and indirectly (e.g. Aprile et al., 2005; CDMS Collaboration, 2009; Bernabei et al., 2008).

This thesis focuses on the measurement of the dark matter density in the Milky Way disc. Turning a detected dark matter signal into particle properties requires the very local dark matter density (ρ_{dm}), and in some cases also the dark matter velocity distribution. Furthermore the precise knowledge of the the dark matter distribution in the disc of our Galaxy is important to understand its structure, constraining the shape of the dark matter halo and the possible presence of a dark matter disc (Lake, 1989; Read et al., 2008; Read et al., 2009, see Section 1.2).

This thesis aims to measure the dark matter density using the kinematics of local stellar tracers to constrain the disc potential. I introduce the topic of this thesis, describing the main evidences for dark matter (Section 1.1.1), the most likely candidates for dark matter particles (Section 1.1.2) and the possible alternative to dark matter (Section 1.1.3); I then assess the current knowledge of the dark matter distribution in our Galaxy (Section 1.2) and review the literature on various measurements of the local dark matter density (Section 1.2.1). Finally, I review the theory of measuring of the dark matter density in the Galactic disc from kinematics of local stellar tracers (Section 1.2.2).

1.1 Dark matter in the Universe

1.1.1 Evidences for dark matter

According to the Lambda Cold Dark Matter (ΛCDM) cosmological model, most of the Universe is dark (e.g. Komatsu, 2011), $\sim$ 72% of it being composed of dark energy, $\sim$ 22% of dark matter and $\sim$ 4% of baryonic matter. Dark matter is the dominant component by gravitating mass. Although dark matter – not emitting any light – can not be observed directly, its presence is inferred from its gravitational influence on the motion of observable astronomical objects on all scales, from stars to galaxies and cluster of galaxies. In this section I will review the main evidences for the existence of dark matter.

1.1.1.1 Galaxy clusters

Dark matter was first proposed by the Swiss astronomer Fritz Zwicky in the 1930s. Zwicky estimated the total mass of the *Coma cluster* – one of the densest known galaxy collections in the Universe (see figure 1.1) – and compared it to the mass of the observed luminous matter, finding a large mismatch between the two (Zwicky, 1933, 1937). He used the *virial theorem* to calculate the mass of the cluster dynamically. The virial theorem is

$$2T + V = \frac{1}{2}\ddot{I} = 0 \tag{1.1}$$

where $V = \sum_i \mathbf{F}_i \cdot \mathbf{r}_i$ is the total potential energy of the cluster, $T = \frac{1}{2}\sum_i m_i \dot{r}_i^2$ is the total kinetic energy and $I = \sum_i m_i r_i^2$ is moment of inertia. The last equality is valid assuming that the cluster is in equilibrium.

The virial theorem allows to measure the mass of the cluster in terms of the average velocity dispersions of the single galaxies; under the hypothesis that the galaxies are uniformly distributed inside a sphere of radius R – corresponding to the size of the cluster – one can roughly estimate the potential energy of the cluster as $V \sim -\frac{3GM^2}{5R}$ (Zwicky, 1937) – where M is the total mass of the cluster and G is the gravitational constant – and the kinetic energy as $T \sim \frac{1}{2}M3\sigma^2$ – where $\sigma^2 = \overline{v^2} - \overline{v}^2$ is the line of sight velocity dispersion. So, using equation

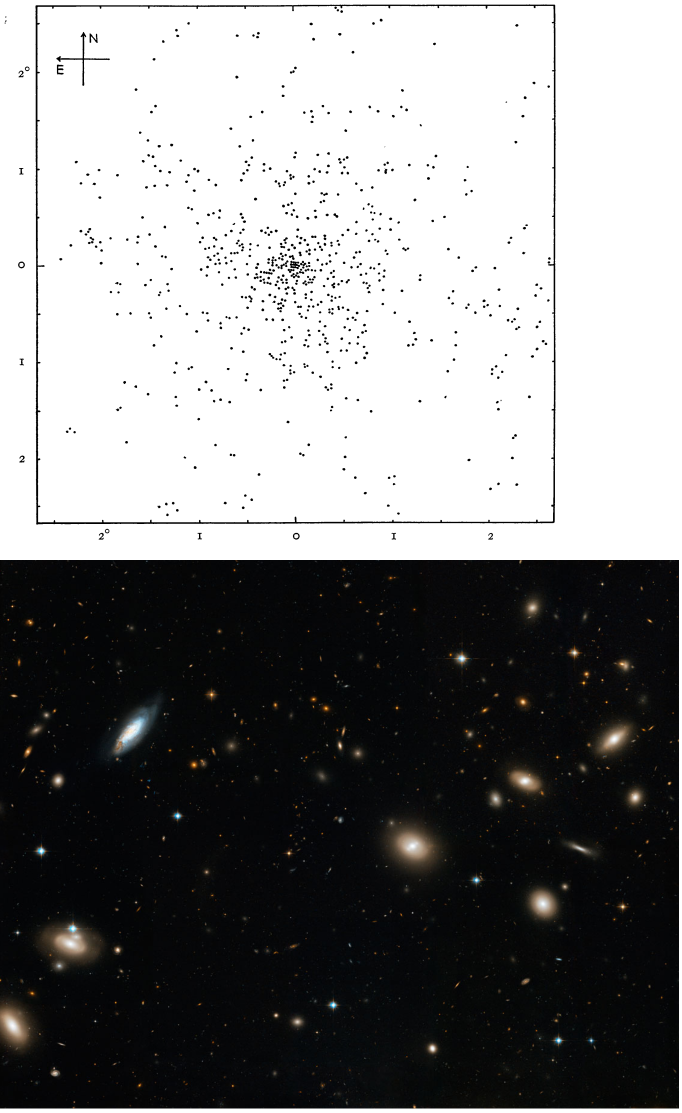

Figure 1.1: The Coma cluster. *Upper Panel:* as seen by Zwicky (Zwicky, 1937); *Lower Panel:* as seen by the Hubble Space telescope. Credits: NASA, ESA, and the Hubble Heritage Team (STScI/AURA).

1.1, one can approximately estimate the mass of the cluster as $M \sim 5\sigma^2 R/(3G)$. Zwicky showed that even if the uniformity assumption is quite rough and the velocity dispersion is not very well determined, the virial theorem gives a robust estimate for the order of magnitude for the cluster's mass. Using the values of σ^2 and R available at his time, Zwicky estimated the dynamical mass of the Coma cluster to be $M \gtrsim 4.5 \times 10^{13}\,\mathrm{M}_\odot$. Comparing this value with the estimate from the luminous mass, Zwicky inferred for the first time the existence of unseen matter, which he referred to as *dark matter*.

More modern determinations of the clusters' mass come also from the X-ray observations of the hot intracluster gas – if the density and the temperature of the gas are known, assuming that the cluster is in hydrostatic equilibrium. This method has several advantages: firstly the gas is a collisional fluid and the gas particles' velocities are isotropically distributed, differently from the galaxies used as test particles in clusters; secondly this method allows to measure the mass as a function of radius, instead of the average mass of the whole cluster. X-ray observations of clusters confirm that the gas is in hydrostatic equilibrium (e.g. Rosati et al., 2002). Measurement of cluster masses using Einstein X-ray satellite (e.g. Bahcall & Sarazin, 1977) and Chandra (e.g. Rasia et al., 2006; Ettori et al., 2010) confirm the mass estimates made with the virial theorem, supporting the presence of dark matter. Notice that Zwicky's estimate of the baryonic mass of Coma was very low: he underestimated the stellar mass by a large factor and he could not constrain the gas mass. Using X-ray gas observations we now know that Coma has a mass to light ratio very close to the cosmic value with most of the baryons in X-ray emitting gas.

1.1.1.2 Rotation curves of galaxies

The observation of the rotation curves of galaxies, i.e. the variation of the orbital velocity as a function of the galactocentric distance, is strong evidence for the presence of unobserved matter: low surface brightness and giant spiral galaxies rotate too fast to be supported by their stars and gas alone, betraying the presence of dark matter around them (de Blok et al., 2001; Simon et al., 2005; Borriello & Salucci, 2001; Klypin et al., 2002). Since the earliest studies – e.g. Freeman (1970), Rubin et al. (1980) and van Albada et al. (1985) – we have known that the potential due to luminous matter alone was not sufficient to support the fast rotation of disc galaxies at large radii (see figure 1.2).

The circular velocity of galaxies can be easily determined measuring the velocity of gas, moving in nearly circular orbits in the discs. Galactic discs contain large amounts of neutral hydrogen (HI) and the velocity of this gas can be easily determined using the relative Doppler shift of the 21 cm spectral line of hydrogen.

The observed flat rotation curves of galaxies suggest that the radial density distribution in galaxies must be approximately isothermal $\rho(r) \sim r^{-2}$ (where r is the radial distance from the centre in spherical coordinate). To balance the

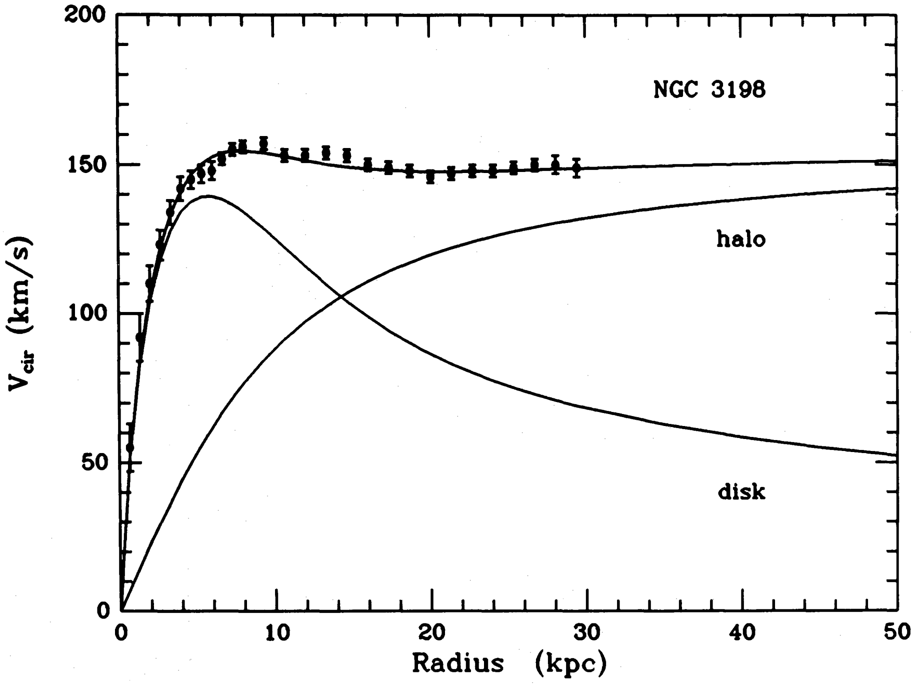

Figure 1.2: Fit of the observed rotation curve (data points with error bars) of NGC 3198 by van Albada et al. (1985), assuming an exponential disc having a scale length corresponding to that of the luminous matter and a spherical dark matter halo. This figure is taken from van Albada et al. (1985).

centripetal force and gravity, the circular velocity V_c is given by:

$$\frac{V_c^2}{r} = -\frac{\partial \Phi}{\partial r}, \tag{1.2}$$

where Φ is the gravitational potential. The gravitational potential is in turn related to the total density through (the radial component of) the Poisson equation:

$$\frac{\partial^2 \Phi}{\partial r^2} = 4\pi G \rho(r) \tag{1.3}$$

which, for a flat rotation curve $V_c =$constant, is

$$\rho(r) \sim \frac{\partial (V_c/r)}{\partial r} \sim \frac{V_c}{r^2}. \tag{1.4}$$

However the observed luminous mass density decreases almost exponentially with increasing r, with a scale length of few kpc (solid line, labeled 'disc' in figure 1.2). This discrepancy can be explained by the presence of a large amount of unseen dark matter in the galaxies.

1.1.1.3 Gravitational lensing

The mass of galaxy clusters, galaxies and even stars is so large that they can bend and focus the light coming from more distant objects through a relativistic phenomenon called *gravitational lensing*. Lensing can be used to measure the mass distribution of the lens. Gravitational lensing was proposed by Chwolson (1924), but the first real calculation was accomplished by Einstein (1936). However at that time – with the only exeption of Zwicky (1937) – it was thought that this effect could not be observed. Later in the 1960s, Refsdal (1964a) laid the foundation for the modern gravitational lensing theory; the first gravitational lens was finally discovered by Walsh et al. (1979).

There are three different regimes of lensing, depending on the gravitational potential of the lensing objects which bends the light coming form a background source and on the relative position of the lens and the source:

Strong lensing: Image distortions such as Einstein rings, arcs and multiple images are easily visible (see figure 1.3). Strong gravitational lensing happens when the mass in the lensing foreground object is large; it is visible when the background source and the lensing foreground object are in good alignment. It

Figure 1.3: This image shows the full overview of the galaxy cluster Abell 2218 and its gravitational lenses. The cluster is so massive that its gravity bends the light from several background galaxies which look distorted into arcs or multiplied. This image was taken by Hubble in 1999 during the Early Release Observations made immediately after the Hubble Servicing Mission 3A. Credit: NASA, ESA, A. Fruchter and the ERO Team (STScI, ST-ECF).

is observed in clusters and massive galaxies, whose gravitational field distorts the images of single background objects, such as quasars. The strong lensing allows to determine the distribution of gravitating mass in galaxy clusters: the observed gravitationally lensed images from giant elliptical galaxies and galaxy clusters requires a diffuse mass distribution of non luminous matter in the lensing system to explain the observed image distributions (e.g. Refsdal, 1964b; Bourassa & Kantowski, 1975; Walsh et al., 1979; Soucail et al., 1987; Clowe et al., 2006). This confirms the results obtained using the virial theorem and the X-ray data (see Section 1.1.1.1).

Weak lensing: The lens is less strong and the distortions of single background sources are much less visible than in the strong lensing regime; the distortion can only be detected through the statistical analysis of a large number of objects. Weak lensing can produce a measurable effect in two ways: i) when background galaxies are weakly lensed by foreground structure, either large scale structures or foreground galaxy clusters (e.g. Villumsen et al., 1997); ii) when the weak magnification effect changes the observed number density of source background galaxies or change the size of images of a given surface brightness (e.g. Schneider, 2006). By measuring the positions, the shapes and the orientations of large numbers of distant galaxies, it is possible to reconstruct the mass distribution – and so the dark matter distribution – in the area. Weak lensing measurement are in this way important dark matter probes.

Microlensing: Microlensing is unresolved strong lensing; what is visible is a change in the magnification of a source in time. In practice, microlensing events can be observed as a lens and source move in and then out of alignment. This results in an achromatic (i.e. it is the same at all the wavelengths) magnification and then demagnification of the source that has a characteristic shape called the light curve. The lens and source must be very close together and microlensing is typically observed from stars (or compact objects) lensing stars within a galaxy. Microlensing is used to detect the so called MACHOs (Massive Compact Halo Objects): MACHOs are small objects such as planets, dead stars (white dwarfs) or brown dwarfs, emitting so little light that they are invisible most of the time, but can be detected while passing in front of a star. These objects has been considered as possible baryonic candidate for the missing dark matter. Several groups have searched for microlensing events to hunt for the baryonic dark matter. However the results from these studies prove that dark matter cannot comprise massive compact objects in the mass range $0.6 \times 10^{-7} \lesssim M/M_\odot \lesssim 15$ (Gates et al., 1995; Tisserand et al., 2007; Wyrzykowski et al., 2011) and the observations from the Hubble space telescope (Graff & Freese, 1996) show that MACHOs are not a significant fraction of dark mass in our Galaxy.

1.1.1.4 Dwarf galaxies

Dwarf galaxies are the most dark matter dominated objects in the Universe. The first evidence for dark matter in dwarf galaxies came from the velocity dispersion measurement (using just three stars) by Aaronson (1983) in Draco: he found a global mass-to-light ratio of $[M/L_V] \geq 10[M/L_V]_\odot$. Following studies confirmed that Draco has a mass-to-light ratio in the range $10[M/L_V]_\odot \leq [M/L_V] \leq 100[M/L_V]_\odot$ (Mateo, 1998). The study of motions of stars or gaseous clouds in many nearby dwarf galaxies finds that all these objects are dark matter dominated even in their central regions (e.g. Simon & Geha, 2007; Martin et al., 2007; Walker et al., 2007).

In recent years, the advent of deep photometric surveys, including the Sloan Digital Sky Survey (Abazajian et al., 2009), made it possible to discover several new *ultra faint* dwarf galaxies in the Milky Way vicinity (e.g. Willman et al., 2005; Belokurov et al., 2006; Zucker et al., 2006); these objects have been found to be very under-luminous but equally massive as the previously known nearby dwarf galaxies: this makes them very good candidates for extreme dark matter dominated objects, with mass to light ratios approaching $M/L_V \sim 10^4$ (Geha et al., 2009).

1.1.1.5 The role of dark matter in cosmology

Dark matter is a fundamental ingredient in the current cosmological model of the Universe, providing a simple solution to several issues. In this section I review the main ones.

The cosmic microwave background All the structures in the Universe formed via gravitational clustering, starting from initial small fluctuations of the matter density. To form large structures, the amplitude of the initial density fluctuations must have been large enough at the time of recombination, when the Universe started to become transparent and radiation and baryonic matter began to evolve separately. The size of these primordial fluctuations remained imprinted in the temperature fluctuations of the Cosmic Microwave Background (CMB; Penzias & Wilson, 1965; Peebles, 1965). The first measurements of the CMB inhomogeneities by COBE (COsmic Background Explorer satellite) gave a puzzling result: the fluctuations were much lower than expected from the density evolution of luminous matter (Smoot et al., 1992). The launch of BOOMERANG (Baloon Observations Of Millimetric Extragalactic Radiation and Geophysics) in 1998 allowed to measure the first Doppler peak of the CMB spectrum and to estimate the baryon density (Lange et al., 2001). WMAP (Wilkinson Microwave Anisotropy Probe), launched in 2001, measured the anisotropies in the CMB far more precisely than ever before. Due to its increased precision (and through the use of computer codes which can calculate the CMB anisotropies given fundamental parameters such as the baryon density) we now know the total and baryonic matter densities[1]: $\Omega_{\rm m}h^2 = 0.1334^{+0.0056}_{-0.0055}$ and $\Omega_{\rm b}h^2 = 0.0260 \pm 0.0053$ (Jarosik et al.,

---

[1] $\Omega_i h^2$ is the physical density; it is given by $\Omega_i h^2 = \rho_i/\rho_{\rm crit} h^2$, where $\rho_{\rm crit}$ is the critical density and h is the Hubble constant H_0 divided by 100.

2011). These two numbers are different, meaning that baryons are not the only gravitating matter in the Universe: non baryonic dark matter comprises about the 83% of the total matter content.

The power spectrum The most likely sources of the primordial density perturbations, at the origin of the observed structures in the Universe, are quantum fluctuations that were magnified by inflation – a period of early rapid exponential expansion of the Universe approximately 10^{-35} s after the Big Bang. If these random fluctuations are Gaussian, one can describe all the density perturbations using a single function: the power spectrum $P(k)$. The power spectrum can be experimentally calculated in several ways, for example using gravitational lensing (e.g. Hoekstra et al., 2002), Lyman α forest (e.g. Gnedin & Hamilton, 2002), the CMB (e.g. Shafieloo & Souradeep, 2004) or galaxy counts (e.g. Tegmark et al., 2004; Abazajian et al., 2009). Each of these probes gives information about the power spectrum on different scales and at different epochs. Using cosmological models, one can then obtain the primordial power spectrum. In combination these independent probes become very powerful (Tegmark & Zaldarriaga, 2002). By obtaining the matter power spectrum, the amount of total matter and baryonic matter can be determined separately: the overall strength of $P(k)$ depends on the total matter density, while the amount of baryons affects the shape of $P(k)$. These results are in very good agreement with the CMB measurements (Cole et al., 2005; Percival et al., 2010).

1.1.2 Dark matter as a particle

Although the existence of dark matter is well motivated by several independent means (see Section 1.1.1), its composition remains an unresolved problem. As seen in Section 1.1.1.5, the cosmological model of structure formation and the observed fluctuations of the cosmic microwave background suggest that dark matter must be electrically neutral and non baryonic. The most popular candidates for dark matter particles, beyond the Standard Model, are the *WIMPs* (Weakly Interacting Massive Particles, Jungman et al., 1996), sterile neutrinos (Boyarsky et al., 2009) and axions (Duffy & van Bibber, 2009).

The Standard Model of particle physics is the quantum field theory that describes three of the four fundamental forces in nature: electricity and magnetism, the weak nuclear force, and the strong nuclear force (gravity is not part of the

Standard Model). The Standard Model comprises seventeen particles: six quarks (up, down, top, bottom, charm, and strange), six leptons (electron, μ, τ, and their respective neutrinos), and five force carriers (photons, gluons, $W^{\pm}$, Z, and the Higgs boson). Quarks and leptons are called fermions, they have half integer spins and are split into three generations, while the force carriers are classified as gauge bosons with integer spins. For each of these particles a corresponding antiparticle with opposite charge exists (e.g. Bailin & Love, 1994).

Despite its success, the Standard Model does not contain any particle that could be dark matter. In fact the only stable, electrically neutral and weakly interacting particles in the Standard Model are neutrinos (and antineutrinos). However neutrinos can not be dark matter for two main reasons. Firstly, they are light particles, so a neutrino dominated Universe would have suppressed the hierarchical structure formation. Secondly, neutrino mass is constrained to be $< 0.23\,\mathrm{eV}$ by WMAP data combined with large-scale structure data, leading to a total mass-energy density which is far too small to account for all the missing matter (Jarosik et al., 2011). Even if the Standard Model does not include any possible candidate for dark matter, this does not invalidate it, but it rather requires an extension to the model.

The most promising extension is supersymmetry (SUSY). SUSY has an additional symmetry between fermions and bosons, adding several "super-partner" particles to the Standard Model's ones. Supersymmetry solves some problems of the Standard models, but it is particularly interesting to us because it offers a viable dark matter candidate: a WIMP called *neutralino*. Although none of the supersymmetric particles has been detected in lab, SUSY still represents the best hope of modeling and understanding dark matter. In the minimal supersymmetry model dark matter densities and detection rates can be calculated (e.g. Baer & Brhlik, 1998).

1.1.2.1 WIMPs detection

There are three main approaches to detect WIMPs (e.g. Jungman et al., 1996): producing them in particle accelerators, as the Large Hadronic Collider (LHC) at CERN, hunting for indirect hints of their presence (Carr et al., 2006) or trying to detect them via interactions with a large underground detector (Baudis & Klapdor-Kleingrothaus, 2000). The LHC is just beginning to collect and analyse data; there is a chance that it creates WIMP-like matter in the next future.

Indirect detection techniques are based on the detections of secondary products of WIMPs annihilations. In supersymmetry neutralinos are classified as Majorana particles (i.e. they are their own antiparticle) and therefore annihilate with each other, giving rise to various products which can be detected, like gamma-rays, neutrinos and antimatter. Because the annihilation rate of WIMPs is proportional to the square of the dark matter density, natural places to look for dark matter annihilations are high density regions, such as the nearby dwarf galaxies and the Galactic center. WIMP annihilations produce gamma-rays with a distinct spectrum. An alternative possibility for indirect detection is that WIMPs are gravitationally captured by the Sun and collect at the centre. There the WIMP density becomes high enough for annihilation to occur. In this case we expect to detect a signal in high energy neutrinos that – unlike gamma-rays – can escape from the centre of the Sun and so can be detected in neutrino telescopes on Earth (Carr et al., 2006). Finally antimatter can be a very good marker for WIMPs annihilation, since antimatter is rare cosmically and many of the astrophysical processes that create antimatter background are understood. So far none of the above strategies has yielded a clear signal of WIMPs, but the experiments continue to improve.

WIMP direct detection experiments like, XENON and CDMS, continue to improve too (Aprile et al., 2005; CDMS Collaboration, 2009). The basic idea behind direct detection experiments is simple: a very sensitive device containing a large amount of some element is set up to detect very small motions and interactions of atoms within it. If dark matter is everywhere in the Universe, then it should be traveling through the Earth (and therefore through the detector) all the time. Although dark matter is weakly interacting, it may occasionally bump into the nucleus of a detector atom and deposit some energy which can be revealed by the detector. The differential rate of such events as a function of recoil energy is given by:

$$\frac{dR}{dE} = \frac{\rho_{\rm dm}\sigma_{wn}|F(E)|^2}{2m\mu^2}\int_{v>\sqrt{ME/2\mu^2}}^{v_{max}} \frac{f_{\rm dm}(\mathbf{v},t)}{v} d^3v \tag{1.5}$$

where $\rho_{\rm dm}$ is the local dark matter density; σ_{wn} is the WIMP interaction cross section; $|F(E)|$ is the WIMP-nucleus form factor; m and M are the masses of the dark matter particle and the target nucleus, respectively; μ is the reduced mass of the WIMP-nucleus system; $v = |\mathbf{v}|$; and v_{max} is the maximum velocity of WIMPs in the Earth frame. To measure σ_{wn} and m (the WIMP particle properties), it is necessary to measure the local dark matter density $\rho_{\rm dm}$. It can be estimated using astrophysical observations. The determination of $\rho_{\rm dm}$ is the main purpose of this thesis.

1.1.3 Alternatives to dark matter

The large amount of dark matter needed has prompted alternative theories, involving a modification of the Newtonian gravity instead.

An early scheme by Milgrom (1983) modified Newtonian dynamics (MOND), but the recent focus has been on changing the law of gravity in the weak regime (e.g. Moffat, 2006). Despite the successes in accounting for flat rotation curves, modified gravity models face several major critical problems: evidences for dark matter exists on many distance scales, but modified gravity theories only work on galactic ones. For example, when considering galaxy clusters, they cannot account for density and temperature profiles and unseen matter is required (e.g. Aguirre et al., 2001). The most popular example for modified gravity failure is the "bullet" cluster, or cluster 1E 0657-558 (Clowe et al., 2006, 2007), shown in figure 1.4. It is a pair of galaxy clusters, where the smaller one (the "bullet", on the right of the figure) has passed the main cluster almost tangentially to the line of sight. The hot X-ray emitting gas has been separated by ram pressure stripping during the passage (see lower panel of figure 1.4). The reconstruction of the gravitating mass distribution from weak lensing (red lines in figure 1.4) shows that it coincides with the distribution of observed galaxies (see upper panel of figure 1.4). However the dominant component in baryonic mass is in X-ray gas which is well separated from the mass distribution. This separation is only possible if the mass is in the collisionless component, i. e. in non baryonic dark halo and not in baryonic gas. Modified gravity theories in their current formulation can not account for such a discrepancy easily. For these reasons, dark matter is still the more promising solution to the puzzle of missing mass in the Universe.

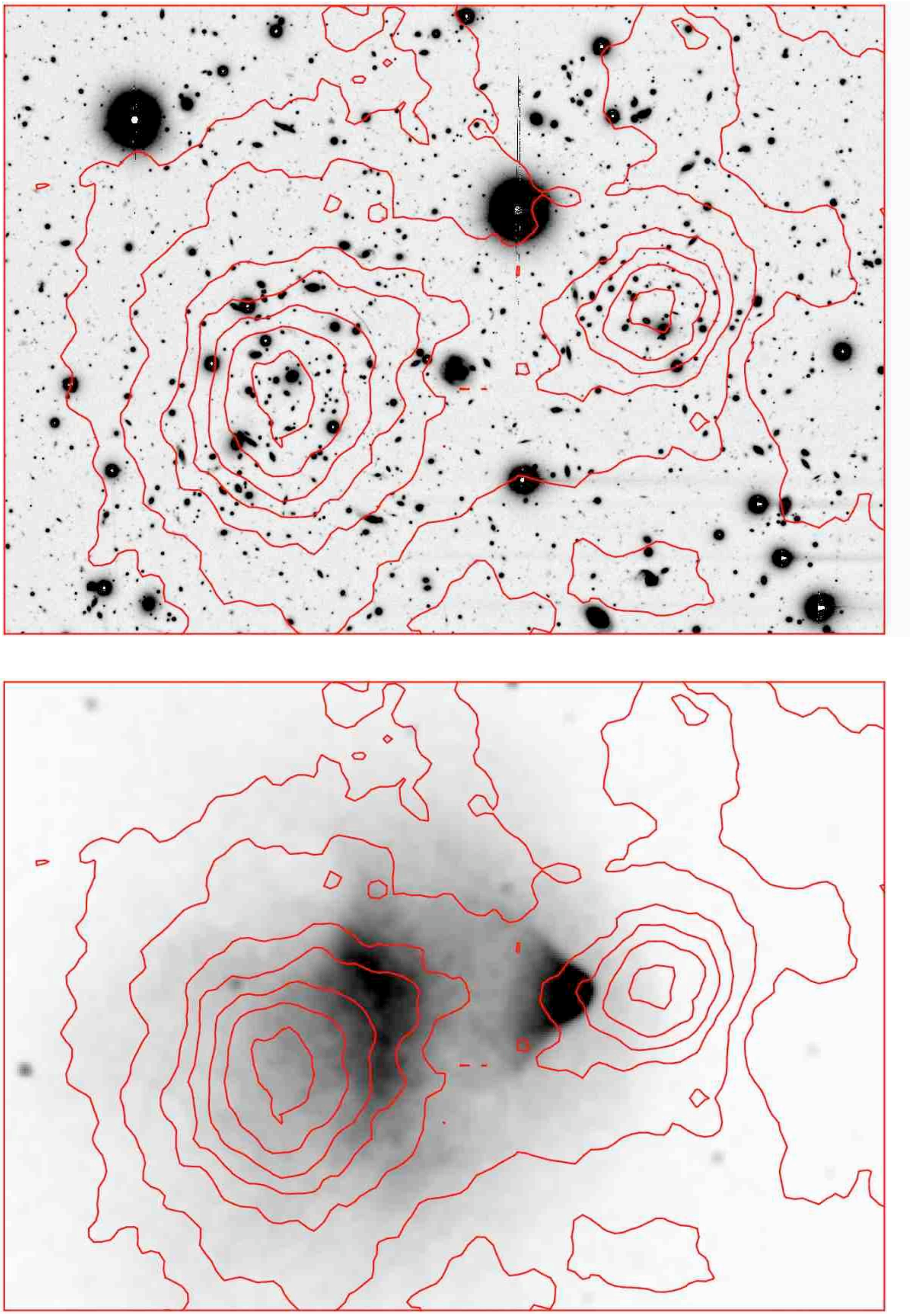

Figure 1.4: *Upper panel:* R band image from Magellan of the merging cluster 1E 0657-558 (the "bullet" cluster). *Lower panel:* 522 ks Chandra image of the "bullet" cluster. Shown in contours on both panels is the weak lensing mass distribution reconstruction. The images are taken from Clowe et al. (2006).

1.2 Dark matter in the Milky Way

In our Galaxy we can measure accurately the kinematics of individual stars and gas, in order to understand the dynamical influence of dark matter. A variety of dynamical measurements predict that the Milky Way is embedded in a halo of dark matter which contains most of its mass and extends far beyond the visible disc of the Galaxy. However the shape and the mass distribution of the dark matter halo of the Galaxy is still under debate.

The formation of flat astrophysical systems, such as galactic discs, requires dissipation to remove energy, but conserve angular momentum, creating thin rotating discs. Non-baryonic collisionless dark matter can not dissipate energy: for this reason the dark matter halo is expected to have only modest flattening. Dark matter only numerical simulations of galaxy formation suggest that the shape of halos are *triaxial* (e.g. Dubinski & Carlberg, 1991; Jing & Suto, 2002; Bailin et al., 2005), and preferentially prolate (e.g. Macciò et al., 2007), rather than spherical, but there is little direct observational evidence on the halo shape. When including the dissipative baryons into simulations, halo shapes become rounder and more aligned with the disc (e.g. Dubinski, 1994; Kazantzidis et al., 2004; Debattista et al., 2008). It is likely that the shape of the halo reflects the last major merger occurred: more prolate shapes arise when the halo undergoes a merger with a comparable massive halo from a nearly radial orbit, while if the the orbit is more circular, oblate halos are expected to form (Moore et al., 2004).

The size and the mass of the Milky Way halo can be constrained using the kinematics of distant globular clusters and nearby galaxies; the resultant mass is $\sim 2 \times 10^{12}$ $\mathrm{M}_\odot$, with a half mass radius of about 100 kpc (Wilkinson & Evans, 1999); however both the size and the mass of the halo are uncertain, as we can see in Table 1.1, reporting the main features of the different dark and luminous components of our Galaxy.

The contribution of the dark matter halo to circular speed at the Sun's position $R_\odot$ is also uncertain and could lie anywhere from less than 20% to about 50% of the total force without violating the observational contraints (e.g. Sofue et al., 2009). As we will see in Section 1.2.1, using the rotation curve to find the value of the dark matter density at the Sun position depends on the uncertain shape of the dark matter halo. These uncertainties on the dark matter distribution inside $R_\odot$ are a significant concern for laboratory detections of dark matter (e.g.

Table 1.1: The distinct components of the Milky Way. From left to right the columns show: the total mass (M); the half mass scale-length ($R_{1/2}$); and the half mass scale height ($z_{1/2}$). These values are compiled using the following relations: $z_{1/2} = 0.55 z_s = 0.7 z_0$ and $R_{1/2} = 1.68 R_0$ (Read et al. 2008), where z_s is the sech^2 disc scale height, z_0 is the exponential disc scale height and R_0 is the exponential disc scale length.

	M [10^{10}M$_\odot$]	$R_{1/2}$ [kpc]	$z_{1/2}$ [kpc]	Ref.
Thin disc	$3.5 - 5.5^*$	$3.35 - 9.24$	$\sim 0.14 - 0.18$	fl,o,fe,k
Thick disc	-	$5.04 - 7.56$	$0.49 - 0.84$	o,n,s
Bulge	~ 1	-	-	d,fl
Halo	$\sim 40 - 200$	-	-	x,g

References: fl=Flynn et al. (2006); o=Ojha (2001); fe=Feast (2000); k=Kuijken & Gilmore (1989a); n=Ng et al. (1997); s=Spagna et al. (1996); d=Dehnen & Binney (1998); x=Xue et al. (2008); g=Guo et al. (2010).
* total disc mass

Gaitskell, 2004, see Section 1.1.2.1). However an accurate local measurement of the dark matter density through kinematics of stars would provide a more robust determination, independent on the halo shape (see in Section 1.2.1).

Recent cosmological simulations (Read et al., 2008; Read et al., 2009) predict that – once baryonic matter is included – a *disc of dark matter* forms in our Galaxy from accreted satellites. The formation of this dark matter disc owes to the dynamical action of the accreting satellites against the baryonic disc. The stellar disc is the dominant component inside the solar radius and its dynamical friction causes satellites to be preferentially dragged into the disc plane (Quinn & Goodman, 1986; Quinn et al., 1993). Satellites having a low inclination orbit with respect to the disc plane, are torn apart by tidal forces and not only accrete their stars into a Galactic disc, but also deposit their dark matter into a thick *dark disc* (Lake, 1989). This accreted dark matter disc is predicted to contribute $\sim 0.25 - 1.5$ times the density of the halo density at the Sun position and to rotate slower than the stellar disc (Read et al., 2009). Unlike tidal streams, the dark disc is an equilibrium structure and it is predicted to exist in all the disc galaxies forming in a hierarchical cosmology. Although the dark disc has a local density comparable to the dark halo, its presence has potentially important consequences for dark matter detection experiments. Its low velocity with respect to the Earth has the effect of boosting the capture of WIMPs (Bruch et al., 2009), increasing the annual modulation signal and enhancing the flux at low recoil energy. It can also enhance WIMP capture in the Sun and Earth which can make neutrino telescopes a competitive dark matter probe (Bruch et al., 2009).

1.2.1 The local dark matter density

This thesis focuses on the determination of the local dark matter density – $\rho_{\rm dm}(R_\odot)$ – defined as an average in a small volume around the Sun, typically a few hundred parsecs. There are two main approaches to determine $\rho_{\rm dm}(R_\odot)$: extrapolating its value from the Milky Way's rotation curve ($\rho_{\rm dm,ext}$; e.g. Sofue et al., 2009; Weber & de Boer, 2010); and using the kinematics of stars in the Solar Neighbourhood ($\rho_{\rm dm}$; e.g. Oort, 1932, 1960). The first approach requires an assumption about the global and local shape of the dark matter halo. Simple extrapolations that assume spherical symmetry, suggest $\rho_{\rm dm,ext} \simeq 0.01\,{\rm M_\odot pc^{-3}}$ (Sofue et al., 2009). However, uncertainties about the halo shape lead to errors of at least a factor of two (Weber & de Boer, 2010). Even larger uncertainties arise if the Milky Way has a dark matter disc (Lake, 1989; Read et al., 2008). As it relies on fewer assumptions, we focus on the second approach in this thesis. However, both approaches remain complementary and – together – provide a powerful probe of Galactic structure. If $\rho_{\rm dm} < \rho_{\rm dm,ext}$, this suggests a prolate dark matter halo for the Milky Way; while $\rho_{\rm dm} > \rho_{\rm dm,ext}$ could imply either an oblate halo or a dark matter disc (Lake, 1989; Read et al., 2008; Read et al., 2009).

The local dark matter density is also needed for direct dark matter search experiments. If dark matter is a new Weakly Interacting Massive Particle, or WIMP (Jungman et al., 1996; Baudis, 2006), these experiments produce results that are degenerate between the WIMP interaction cross section and the local matter density (Gaitskell, 2004; Aprile et al., 2005; CDMS Collaboration, 2009), least for a small number of 10-100 events (Peter, 2011). Thus, extracting WIMP properties requires knowledge of $\rho_{\rm dm}$ (e.g. Gaitskell, 2004).

To date, most limits on WIMP properties have assumed the 'Standard Halo Model' (hereafter SHM) density: $\rho_{\rm dm}(R_\odot) = 0.3\,{\rm GeV\,cm^{-3}}$ ($\simeq 0.008\,{\rm M_\odot\,pc^{-3}}$; Jungman et al. (1996))[2]. This is similar to the latest rotation curve extrapolated

---

[2] $1\,{\rm GeV\,cm^{-3}} \simeq 0.0263158\,{\rm M_\odot\,pc^{-3}}$. The Standard Halo Model is an isothermal sphere

values that assume a spherical Milky Way halo. However, if the Milky Way halo is oblate, or there is a dark matter disc, then this could be a significant underestimate (e.g. Weber & de Boer, 2010).

Measuring the local matter density from the kinematics of stars in the Solar Neighbourhood has a long history dating back to Oort (1932, 1960) in the 1930s. Oort used the classical method of solving the combined Poisson-Boltzmann equations for a sample of stars, assumed to be in equilibrium in the total matter distribution of the disc. At that time, Oort found 50% more mass than the sum of known components. A later study by Bahcall (1984c) introduced a new method that described the visible matter as a sum of isothermal components. He also found dynamically significant dark matter in the disc[3] (Bahcall, 1984b). Using faint K dwarfs at the South Galactic Pole, Bahcall et al. (1992) confirmed his earlier result that more than 50% of the mass was dark, although with a lower statistical significance. However, the early studies by Oort (1932, 1960) and Bahcall (1984c,b) assumed that different tracers could be simply averaged to form a single tracer population. Kuijken & Gilmore (1989a) demonstrated that the two samples of F stars analysed by Bahcall (1984c) were not compatible (i.e. they had different spatial density distribution, but no evidence for a difference in their kinematics) and therefore should not be averaged. They re-analysed the K giant sample used by Bahcall (1984b), assigning more realistic errors to the density profile and using a more detailed fit to the velocity data, finding a value of total matter density compatible with the observed one. They concluded that the determination of the local volume density remained limited by systematic and random errors with the available data.

With the launch of the ESA satellite Hipparcos (1997), the kinematics and position of tracer stars were measured with much higher accuracy. The improved distance measures give a much more accurate measurement of the local luminosity function, so that the total amount of visible matter can be better estimated as

---

model for the Milky Way's dark matter halo with a value of the dark matter velocity dispersion assumed to be $\sigma_{\rm iso} \simeq 270\,{\rm km\,s^{-1}}$.

[3] We should be careful about what we mean by 'dark matter in the disc'. Early studies like Oort (1932) were typically interested in missing disc-like matter (a 'thin dark disc'); more modern studies try to constrain a significantly more extended dark matter halo that has a near-constant dark matter density up to $\sim 1\,{\rm kpc}$. Even the 'dark disc' predicted by recent cosmological simulations (Read et al., 2008; Read et al., 2009) is sufficiently hot that its dark matter distribution is approximately constant up to $\sim 1\,{\rm kpc}$. Throughout this thesis when we talk about 'dark matter in the disc' we refer to a constant density dark matter component within the disc volume.

well. The latest dynamical measurements of the local density of matter – ρ_{tot} – from Hipparcos data show no compelling evidence for a significant amount of dark matter in the disc (Crézé et al., 1998; Holmberg & Flynn, 2000). Holmberg & Flynn (2000) found $\rho_{\mathrm{tot}} = 0.102 \pm 0.01 \mathrm{M}_{\odot}\mathrm{pc}^{-3}$, with a contribution of about $0.095 \mathrm{M}_{\odot}\mathrm{pc}^{-3}$ in visible matter, consistent with the Kuijken & Gilmore (1989)'s value.

In addition to the local volume density, several authors have calculated the local *surface density* of gravitating matter, probing to larger heights above the disc plane (typically $\sim 1\,\mathrm{kpc}$; e.g. Kuijken & Gilmore, 1989b; Kuijken & Gilmore, 1989, 1991; Holmberg & Flynn, 2004). Using faint K dwarfs at the South Galactic Pole, and using a prior from the rotation curve, Kuijken & Gilmore (1989, 1991) find $\rho_{\mathrm{dm}}^{\mathrm{KG}} = 0.010 \pm 0.005\ \mathrm{M}_{\odot}\,\mathrm{pc}^{-3}$, consistent with that expected from the rotation curve assuming a spherical Galactic dark matter halo[4] (e. g. Sofue et al., 2009; Weber & de Boer, 2010; Catena & Ullio, 2010). A similar result was found in the post-Hipparcos era by Holmberg & Flynn (2004). Recently, Moni Bidin et al. (2012) estimated the surface density using tracers at heights $1.5 < z < 4\,\mathrm{kpc}$ above the disc, making a rather stronger claim (incompatible with the earlier results of Kuijken & Gilmore, 1991; Holmberg & Flynn, 2004) that there is no dark matter near the Sun. However, Bovy & Tremaine (2012) demonstrate that this result is erroneous and owes to one of ten assumptions used by Moni Bidin et al. (2012) being false. Furthermore, Sanders (2012) estimate that the velocity dispersion gradients derived by Moni Bidin et al. (2012) could be biased by up to a factor of two, which would also significantly alter their determination of ρ_{dm}. Reanalysing Moni Bidin et al. (2012)'s data, (Bovy & Tremaine, 2012) found $\rho_{\mathrm{dm}} = 0.008 \pm 0.002\,\mathrm{M}_{\odot}\mathrm{pc}^{-3}$; the authors quote only statistical errors: an estimate of the effect of systematic errors leads them to conclude that their measurement likely represents a lower bound on ρ_{dm}.

Zhang et al. (2012) recently used a sample of 9000 K dwarfs up to 1.5 kpc with SDSS/SEGUE (Sloan Extension for Galactic Understanding and Exploration) spectra to calculate the local surface density and ρ_{dm}, finding $\rho_{\mathrm{dm}} = 0.0065 \pm 0.0023\,\mathrm{M}_{\odot}\ \mathrm{pc}^{-3}$. Studying some $\sim$ 7000 stars in four metallicity bins up to $z \sim 2\,\mathrm{kpc}$ from SDSS, Smith et al. (2012), estimated $\rho_{\mathrm{dm}} = 0.015\,\mathrm{M}_{\odot}\ \mathrm{pc}^{-3}$. Both of these results are consistent with global fits of approximately round dark

---

[4] Note that this consistency with the rotation curve is somewhat circular since this is input as a prior in their analysis.

matter halos to rotation curve data in the outskirts of the Milky Way. Notice that (Bovy & Tremaine, 2012), Zhang et al. (2012) and Smith et al. (2012) could not directly reconstruct the density profile of the tracers, given their complex survey selection functions. For this reason – and other unmodelled systematics – Smith et al. (2012) choose not to quote uncertainties on their derived local dark matter density and surface mass density. Zhang et al. (2012) are more confident of the assumed selection function and their modelling of systematics, and quote $\sim 35\%$ errors on the local dark matter volume density.

With next generation surveys (e.g. Gaia; Jordan, 2008), a significant improvement in the number of precision astrometric, photometric and spectroscopic measurements is expected. With these high precision data, the observational uncertainties would become a secondary source of errors, so it is timely to determine the dominant systematic errors when using the kinematics of local stellar tracers. This is the main aim of this thesis. The thesis work spawned two publications on refereed scientific journals. In the first published article (Garbari et al., 2011, see Chapter 2), I use – for the first time – a high resolution N-body simulation of a Milky Way like galaxy as a mock data set to test the hypothesis and the methods used in the literature. I then develop a new unbiased technique, relying on a minimal set of assumptions (the "Minimal Assumptions" method, or MA), to calculate the local dark matter density and test it on the mock data set before applying it to the real data. The second article (Garbari et al., 2012, see Chapter 3) presents the results of the MA method applied to real data from the literature. Also in this case I use high resolution simulations to test the performance of the method, adding to the mock data set the same issues present in the data (e.g. position and velocity errors). This is the first work to test methods from the literature on an N-body simulation, to measure the local dark matter density without using the rotation curve as a prior, and to use an MCMC to carefully marginalise over the uncertainties. The value of the local dark matter density I obtain is $\rho_{\rm dm} = 0.022^{+0.015}_{-0.013}\,{\rm M_\odot pc^{-3}}$ $(0.85^{+0.57}_{-0.50}\,{\rm GeV\,cm^{-3}})$. The lower bound on $\rho_{\rm dm}$ I find is larger than the SHM value typically assumed in the literature, and is at mild tension with extrapolations from the rotation curve that assume a spherical halo. This result can be explained by a larger normalisation for the local Milky Way rotation curve, an oblate dark matter halo, a local disc of dark matter, or some combination of these. The large error bars I obtained are due to the large observational uncertainties on the star positions and velocities. If this result will be confirmed by future high precision data, it will have important implication both for direct detection experiments and for our understanding of the Milky Way dark matter distribution and dynamical evolution.

In the next section I derive the fundamental equations at the base of the measurement of $\rho_{\rm dm}$ from kinematics of stars in the Solar neighbourhood and review the main hypothesis used in the literature.

1.2.2 Calculating the local dark matter density

The stars in the Milky Way disc move under the influence of the gravitational potential. The gravitational potential, in Newtonian mechanics, is related to the total density $\rho_{\rm tot}$ through the Poisson equation:

$$\nabla^2\Phi = 4\pi G\rho_{\rm tot} \tag{1.6}$$

where $\rho_{\rm tot} = \rho_{\rm s} + \rho_{\rm dm}$ is the total matter density, given by the contribution of the visible ($\rho_{\rm s}$) and the dark matter density ($\rho_{\rm dm}$). In order to calculate the local dark matter density, we must constrain the local gravitational potential Φ, using the kinematics of some local stellar tracers. There are two main approaches in the literature to do this: one based on the Jeans equations and the other that uses the distribution function of the tracers. The first approach – which is at the base of the MA method developed by Garbari et al. (2011) – does not require any assumption about the separability of the distribution function in the vertical and radial direction which is a critical issue, as we will see in Chapter 2; however it does not exploit the full available information on the kinematics of the tracers, as distribution function methods do. I will now review the equation at the base of both the approaches; for simplicity I will refer to the first approach as *Jeans-Poisson methods* and to the second one as *distribution function methods.*

1.2.2.1 The collisionless Boltzmann equation

The stars moving in the disc of the Milky Way are a collisionless system. When modelling such a system, we study its statistical properties, calculating the probability of finding a single star in the six-dimentional phase space volume $d^3\mathbf{r}\, d^3\mathbf{v}$ around a position $\mathbf{r}$ and the velocity $\mathbf{v}$. This probability at a given time t is given by $f(\mathbf{r}, \mathbf{v}, t)d^3\mathbf{r}\, d^3\mathbf{v}$, where f is the *distribution function.* Assuming that all the stars are identical, their probability is the same for all of them. The distribution function for a single star is normalised such that

$$\int f(\mathbf{r}, \mathbf{v}, t) d^3\mathbf{r}\, d^3\mathbf{v} = 1, \tag{1.7}$$

where the integral is over the whole phase space: this means that the probability of finding a star anywhere in the phase space is 1 (i.e. 100%). Since any given star moves through the phase space, the probability of finding it in any phase space location evolves with time. As f evolves, the probability must be conserved similarly to the mass in a fluid flow. So the distribution function obeys a kind of continuity equation:

$$\frac{\partial f}{\partial t} + \frac{\partial}{\partial \mathbf{w}} \cdot (f\dot{\mathbf{w}}) = 0 \tag{1.8}$$

where $\mathbf{w} = (\mathbf{q}, \mathbf{p})$, and $\mathbf{q}$ and $\mathbf{p}$ are the generalised phase space coordinates. Using the Hamilton's equations

$$\dot{\mathbf{q}} = \frac{\partial H}{\partial \mathbf{p}}; \quad \dot{\mathbf{p}} = -\frac{\partial H}{\partial \mathbf{q}}, \tag{1.9}$$

where H is the Hamiltonian, one can write

$$\begin{aligned} \frac{\partial}{\partial \mathbf{w}} \cdot (f\dot{\mathbf{w}}) =& \frac{\partial}{\partial \mathbf{q}} \cdot (f\dot{\mathbf{q}}) + \frac{\partial}{\partial \mathbf{p}} \cdot (f\dot{\mathbf{p}}) = \frac{\partial}{\partial \mathbf{q}} \cdot \left(f\frac{\partial H}{\partial \mathbf{p}}\right) - \frac{\partial}{\partial \mathbf{p}} \cdot \left(f\frac{\partial H}{\partial \mathbf{q}}\right) = \\ =& \frac{\partial f}{\partial \mathbf{q}} \cdot \frac{\partial H}{\partial \mathbf{p}} - \frac{\partial f}{\partial \mathbf{p}} \cdot \frac{\partial H}{\partial \mathbf{q}} = \dot{\mathbf{r}} \cdot \frac{\partial f}{\partial \mathbf{q}} + \dot{\mathbf{p}} \cdot \frac{\partial f}{\partial \mathbf{p}}, \end{aligned} \tag{1.10}$$

so equation 1.8 becomes the *collisionless Boltzmann equation* (or *Vlasov equation*):

$$\frac{\partial f}{\partial t} + \dot{\mathbf{q}}\frac{\partial f}{\partial \mathbf{q}} + \dot{\mathbf{p}}\frac{\partial f}{\partial \mathbf{p}} = 0 \quad \leftrightarrow \quad \frac{\partial f}{\partial t} + \frac{\partial f}{\partial \mathbf{q}} \cdot \frac{\partial H}{\partial \mathbf{p}} - \frac{\partial f}{\partial \mathbf{p}} \cdot \frac{\partial H}{\partial \mathbf{q}} = 0 \tag{1.11}$$

For the disc of the Milky Way it is convenient to use cylindrical coordinate $(R, z, \theta, p_R, p_z, p_\theta)$; in this system the Hamiltonian becomes $H = \frac{1}{2}(p_R^2 + p_\theta^2/R^2 + p_z^2 + \Phi)$ – where Φ is the gravitational potential – and so the Boltzmann equation is:

$$\frac{\partial f}{\partial t} + p_R\frac{\partial f}{\partial R} + \frac{p_\theta}{R}\frac{\partial f}{\partial \theta} + p_z\frac{\partial f}{\partial z} - \left(\frac{\partial \Phi}{\partial R} - \frac{p_\theta^2}{R^3}\right)\frac{\partial f}{\partial p_R} - \frac{\partial \Phi}{\partial \theta}\frac{\partial f}{\partial p_\theta} - \frac{\partial \Phi}{\partial z}\frac{\partial f}{\partial p_z} = 0 \tag{1.12}$$

In case of an axisymmetric system (as the disc of our Galaxy) all the derivatives with respect to θ vanish. If we assume that the local disc of the Milky Way is also in *equilibrium* (*steady state assumption*), we neglect the time derivatives too, to obtain:

$$p_R \frac{\partial f}{\partial R} + p_z \frac{\partial f}{\partial z} - \left(\frac{\partial \Phi}{\partial R} - \frac{p_\theta^2}{R^3} \right) \frac{\partial f}{\partial p_R} - \frac{\partial \Phi}{\partial z} \frac{\partial f}{\partial p_z} = 0 \tag{1.13}$$

1.2.2.2 Jeans-Poisson methods

Ideally one would solve the full Poisson-Boltzmann system (equations 1.6 and 1.13) to calculate the gravitational potential Φ and determine the local density; however in practice this is very complicated and requires full six-dimentional phase space information for the stars in the sample. So we can consider the moment of the Boltzmann equation instead. They can be obtained multiplying equation 1.13 by p_R (p_z or p_θ) and integrating over the momenta expressed, in terms of the velocities $p_R = v_R$, $p_\theta = R v_\theta$ and $p_z = v_z$:

$$\frac{\partial(\nu \overline{v_R^2})}{\partial R} + \frac{\partial(\nu \overline{v_z v_R})}{\partial z} + \nu \left(\frac{\overline{v_R^2} - \overline{v_\theta^2}}{R} + \frac{\partial \Phi}{\partial R} \right) = 0 \tag{1.14}$$

$$\frac{1}{R} \frac{\partial \left(R \nu \overline{v_z v_R} \right)}{\partial R} + \frac{\partial}{\partial z} \left(\nu \overline{v_z^2} \right) + \nu \frac{\partial \Phi}{\partial z} = 0 \tag{1.15}$$

$$\frac{1}{R^2} \frac{\partial \left(R^2 \nu \overline{v_\theta v_R} \right)}{\partial R} + \frac{\partial}{\partial z} \left(\nu \overline{v_\theta v_z} \right) = 0 \tag{1.16}$$

where $\nu(R, z)$ is the spatial density of the sample, $\Phi(R, z)$ is the axisymmetric gravitational potential and $\overline{v_i^2}$ and $\overline{v_i v_j}$ (with $i, j = z, R, \theta$) are the velocity dispersion components. These are the *Jeans equations.*

We focus on the vertical Jeans equation (1.15), assuming that the first term – *the "tilt" term* – is negligible with respect to the other two. Binney & Tremaine (2008) give a convincing argument to neglect the tilt term in the Solar neighbourhood: it is likely smaller than $(\overline{v_R^2} - \overline{v_z^2})(z/R)$ (see their discussion of the asymmetric drift in §4.8.2a and §4.9.3); so, assuming that $\overline{v_R^2}$ and $\overline{v_z^2}$ both decline with R as $\exp(-R/R_d)$, the tilt term in equation 1.15 is constrained by:

$$\left| \frac{1}{R} \frac{\partial(R \nu \overline{v_z v_R})}{dR} \right| \simeq \frac{2\nu}{R_d} \overline{v_R v_z} \lesssim \frac{2\nu z}{R_d} \frac{\overline{v_R^2} - \overline{v_z^2}}{R_\odot} \tag{1.17}$$

The second term in equation 1.15 is of the order of $\nu \overline{v_z^2}/z_d$ where $z_d \ll R_\odot$ and $z_d \ll R_d$ is the disc scale height. Hence the neglected term is smaller then the second term by at least a factor of $2zz_d/(R_d R_\odot)$.

With the above assumption, equation 1.15 becomes a function only of z:

$$\overline{v_z^2}\frac{\partial \nu}{\partial z} + \nu \left(\frac{\partial \Phi}{\partial z} + \frac{\partial \overline{v_z^2}}{\partial z} \right) = 0; \tag{1.18}$$

and we can neglect the other two Jeans equations in R and θ. This is the Jeans equation for a one-dimensional slab. In principle, one should solve it for $R =$ constant. However, in practice we must average over some (small) range ΔR. Equation 1.18 is valid for every stellar population in equilibrium with the Galactic gravitational potential. Notice that the tilt term is negligible for stars close to the Galactic midplane; when approaching z larger than $\sim 1\,\mathrm{kpc}$, the radial derivative of the velocity dispersion cannot be neglected anymore and we need to use all the three terms in the Jeans equation.

The Poisson equation, in cylindrical coordinates, for an axisymmetric system becomes:

$$\begin{aligned} 4\pi G \rho_{\mathrm{tot}} &= \frac{\partial^2 \Phi}{\partial z^2} + \frac{1}{R}\frac{\partial}{\partial R}\left(R \frac{\partial \Phi}{\partial R} \right) \\ &= \frac{\partial^2 \Phi}{\partial z^2} + \frac{1}{R}\frac{\partial V_c^2(R)}{\partial R} \end{aligned} \tag{1.19}$$

where $V_c(R)$ is the (total) circular velocity at a distance R (in the plane) from the centre of the Galaxy. For a flat rotation curve, the second term vanishes and $\rho_{\mathrm{dm}}^{\mathrm{eff}} = \rho_{\mathrm{dm}}(R,z)$. Splitting the matter density ρ_{tot} into disc contributions (gas+stars) that vary with z $(\rho_{\mathrm{s}}(z))$[5], and an effective dark matter contribution that includes the circular velocity term $(\rho_{\mathrm{dm}}^{\mathrm{eff}})$, the Poisson equation becomes:

$$\frac{\partial^2 \Phi}{\partial z^2} = 4\pi G(\rho_{\mathrm{s}}(z) + \rho_{\mathrm{dm}}^{\mathrm{eff}}) \tag{1.20}$$

with:

$$\rho_{\mathrm{dm}}^{\mathrm{eff}} = \rho_{\mathrm{dm}}(R,z) - (4\pi G R)^{-1}\frac{\partial}{\partial R}V_c^2(R) \tag{1.21}$$

Jeans-Poisson methods adopt a mass model for the visible matter density $\rho_{\mathrm{s}}(z)$ and solve the Jeans-Poisson system (equations 1.18 and 1.20) – using the observed

---

[5] Note that we use throughout the notation $\rho_s = \rho_s(0)$ – the in-plane baryonic mass density.

vertical velocity dispersion $\overline{v_z^2}$ and density fall-off $\nu(z)$ for a tracer population – to calculate the gravitational potential and, consequently $\rho_{\rm dm}$. We now review the mass modelling adopted by (Garbari et al., 2011) and the details of the MA method.

Minimal assumption method For a given tracer population i, we can write the Jeans equation 1.18 as:

$$\frac{d\nu_i}{\nu_i} = -\frac{1}{\overline{v_{z,i}^2}} d(\overline{v_{z,i}^2} + \Phi) \tag{1.22}$$

which can be solved straightforwardly:

$$\log\left(\frac{\nu_i}{\nu_i(0)}\right) = -\log\left(\frac{\overline{v_{z,i}^2}}{\overline{v_{z,i}^2}(0)}\right) - \int_0^z \frac{1}{\overline{v_{z,i}^2}} \frac{d\Phi}{dz} dz. \tag{1.23}$$

Thus, at each height above the disc z_*, the density of the tracer population $\nu_i(z_*)$ can be calculated:

$$\frac{\nu_i(z_*)}{\nu_i(0)} = \frac{\overline{v_{z,i}^2}(0)}{\overline{v_{z,i}^2}(z_*)} \exp\left(-\int_0^{z_*} \frac{1}{\overline{v_{z,i}^2}(z)} \frac{d\Phi}{dz} dz\right) \tag{1.24}$$

This general equation for $\nu_i(z)$ can be used to describe all the visible components of the disc. Given the density at the midplane $\nu_i(0)$ and the vertical velocity dispersion $\overline{v_{z,i}^2}(z)$ as a function of z for each of the gas and stellar populations in the local disc, we can model the full disc density distribution as:

$$\rho_{\rm s}(z) = \sum_i m_i^* \nu_i(0) \frac{\overline{v_{z,i}^2}(0)}{\overline{v_{z,i}^2}(z)} \exp\left(-\int_0^z \frac{1}{\overline{v_{z,i}^2}} \frac{d\Phi}{dz} dz\right). \tag{1.25}$$

where m_i^* is the mass-to-light ratio for a given population i. Note that there is an important difference between the vertical velocity dispersion of a tracer population, $\overline{v_{z,i}^2}(z)$ in equation 1.24, and the same quantity as it appears in the mass model (equation 1.25). The former is something that we must measure for our chosen tracers, while the latter is simply a parameter that appears in our disc mass model. To put it another way, the tracers *must* satisfy equation 1.24, but we could replace equation 1.25 with some other mass model for the disc. In particular in Garbari et al. (2011), we showed that assuming that the visible matter density is given by a *superposition of isothermal components* (i.e. having $\overline{v_{z,i}^2}(z) = \overline{v_{z,i}^2}(0) =$constant) does not affect the result; so while it is fundamental to measure $\overline{v_z^2}(z)$ for the tracers population, we can simply use the midplane values of the density and the velocity dispersion of the visible matter component to model $\rho_{\rm s}$ as:

$$\rho_{\rm s}(z) = \sum_i m_i^* \nu_{i,0} \exp\left(-\frac{\Phi(z)}{\overline{v_{z,i}^2}}\right) \tag{1.26}$$

In particular, (Garbari et al., 2011, 2012) use the visible mass model by Flynn et al. (2006), reported in Table 1.2.

In addition to the steady state assumption and neglecting the tilt term in the Jeans equation, the MA relies on a further assumption: that *the dark matter density is constant* in the volume considered (typically up to $z \sim 1\,\mathrm{kpc}$). With this assumption $\rho_{\rm dm}(R,z) = \rho_{\rm dm}(R)$. This hypothesis requires that the disc scale height is much smaller than the dark matter halo scale length $z_d \ll r_h$, or for disc-like dark matter, that the scale height of dark disc is significantly larger than z_d.

The MA method adopts the following procedure to numerically solve the Jeans-Poisson system: first, we make initial trial guesses for $\rho_{\rm s}(0)$ (and any other unknowns in the star/gas disc), $\rho_{\rm dm}$, and the run of vertical velocity dispersion for the tracers $\overline{v_{z,i}^2}(z)$. Next, we solve equation 2.9 to obtain $\Phi(z)$ and its first derivative $\frac{\partial\Phi}{\partial z}$, with $\Phi(0) = \frac{\partial\Phi}{\partial z}\big|_0 = 0$. Then, we plug this result into equation 2.8 to obtain the vertical density fall-off the tracers $\nu_i(z)$. Finally, this is compared with the observed distribution to obtain a goodness of fit. In principle, each tracer population gives us an independent constraint on $\Phi(z)$. A useful consistency check then follows since all tracers should yield the same potential, while combining different tracers gives smaller errors on the derived parameters. Note that the above procedure requires many input parameters that are typically poorly constrained, for example the normalisations and dispersions of each of the disc components and the vertical dispersion profile of the tracers. To efficiently explore this parameter space and marginalise over the uncertainties, we use a Monte Carlo Markov Chain (MCMC) method (for more details see Chapter 2).

Table 1.2: The disc mass model taken from Flynn et al. (2006). Each component in the table gives the local mass density in the midplane $\rho(0)$ in $\mathrm{M_{\odot}pc^{-3}}$, the total column density Σ in $\mathrm{M_{\odot}pc^{-2}}$, and the vertical velocity dispersion $\overline{v_{z,i}^2}(0)^{1/2}$ in $\mathrm{km\,s^{-1}}$. Uncertainties on the densities are of order 50 per cent for all the gas components (indicated with *) and $10-20$ per cent for all the stellar components. For the thick disc, the column density is rather well known, while the velocity dispersion and the volume density are poorly known such that they should have larger error bars. However, these two quantities are essentially nuisance parameters for our analysis here. Since they anti-correlate and – as pointed out by Kuijken & Gilmore (1989b) – the local gravitational potential is mainly constrained by the column density, we simply assume small errors for both here such that the integrated column agrees with the observed value.

Component	$\nu_{i,0}(0)$ $[\mathrm{M_{\odot}\,pc^{-3}}]$	Σ_i $[\mathrm{M_{\odot}pc^{-2}}]$	$\overline{v_{z,i}^2}(0)^{1/2}$ $[\mathrm{km\,s^{-1}}]$
H_2^*	0.021	3.0	4.0 ± 1.0
$\mathrm{HI(1)}^*$	0.016	4.1	7.0 ± 1.0
$\mathrm{HI(2)}^*$	0.012	4.1	9.0 ± 1.0
Warm gas*	0.0009	2.0	40.0 ± 1.0
Giants	0.0006	0.4	20.0 ± 2.0
$M_V < 2.5$	0.0031	0.9	7.5 ± 2.0
$2.5 < M_V < 3.0$	0.0015	0.6	10.5 ± 2.0
$3.0 < M_V < 4.0$	0.0020	1.1	14.0 ± 2.0
$4.0 < M_V < 5.0$	0.0022	1.7	18.0 ± 2.0
$5.0 < M_V < 8.0$	0.007	5.7	18.5 ± 2.0
$M_V > 8.0$	0.0135	10.9	18.5 ± 2.0
White dwarfs	0.006	5.4	20.0 ± 5.0
Brown dwarfs	0.002	1.8	20.0 ± 5.0
Thick disc	0.0035	7.0	37.0 ± 5.0
Stellar halo	0.0001	0.6	100.0 ± 10.0

1.2.2.3 Distribution function methods

Distribution function methods avoid the moments of the Boltzmann equation by introducing an additional assumption: that *the gravitational potential is completely separable* in the z and R direction $\Phi(R,z) = \Phi(R) + \Phi(z)$. This assumption allows to use the full vertical velocity distribution function of the tracers to compute their density fall off, exploiting all the available information about the tracers' kinematic; notice that using the Jeans equation is instead equivalent to consider only the width of the distribution function. However – as we will see in detail in Chapters 2 and 3 – this assumption is critical and can lead to biased results.

Note that if the gravitational potential is completely separable, then the *tilt term* in the Jeans equation is exactly zero and the motions in the z and R directions are completely decoupled. However, we want to stress that the MA method makes the weaker assumption that the tilt term is *small* as compared to the other terms in the Jeans equations, not necessarily zero.

Furthermore this assumption implies that the angular momentum (L_z) in independent on z. In fact if we take the Lagrangian of the system (for an axisymmetric potential):

$$\mathcal{L} = \frac{1}{2}[\dot{R}^2 + (R\dot{\theta})^2 + \dot{z}^2] - \Phi(R,z) \tag{1.27}$$

and apply the Euler-Lagrange equations, we have:

$$\ddot{R} = -\frac{d\Phi(R)}{dR} + R\dot{\theta}^2 \tag{1.28}$$

$$\ddot{z} = -\frac{d\Phi(z)}{dz} \tag{1.29}$$

$$\frac{d}{dt}(R^2\dot{\theta}) = 0. \tag{1.30}$$

Now $L_z = p_\theta = R^2\dot{\theta}$, so:

$$\ddot{R} = -\frac{d\Phi(R)}{dR} + \frac{L_z^2}{R^3} \tag{1.31}$$

$$\ddot{z} = -\frac{d\Phi(z)}{dz} \tag{1.32}$$

$$\frac{dL_z}{dt} = 0. \tag{1.33}$$

The last equation determines the conservation of the angular momentum; from the first two equations, if the potential is separable, $\Phi(R,z) = \Phi(R) + \Phi(z)$, we deduce that the motions in the z and R direction are decoupled and that the angular momentum L_z is independent of z.

If the gravitational potential is separable, we can write a separable distribution function of the tracers: $f = f_{R,\theta}(v_R, v_\theta, R) \times f_z(v_z, z)$. So one can calculate the vertical density fall off of the tracers integrating the distribution function in the vertical velocity space:

$$\nu(z) = \int_{-\infty}^{\infty} dv_z f(E_z) = 2\int_0^{\infty} dv_z \left[f\left(\frac{1}{2}v_z^2 + \Phi\right)\right]; \qquad (1.34)$$

This integral is at the base of the the methods used by Holmberg & Flynn (2000, 2004) (the HF method) and by Kuijken & Gilmore (1989b); Kuijken & Gilmore (1989) (the KG method). These two methods are described in the following sections (for more details see Chapter 2 and 3).

1.2.2.4 The HF method

Instead of using the Jeans equation, Holmberg & Flynn (2000) solve equation 1.34 to compute the predicted density fall off for a tracer population moving in the Galactic gravitational potential. Equation 1.34 can be rewritten as an Abel integral (see Appendix 1.3.1):

$$\nu_i(z) = 2\int_{\Phi(z)}^{\infty} d(\sqrt{2E_z})\sqrt{2E_z}\frac{f(\sqrt{2E_z})}{\sqrt{2\,(E_z - \Phi)}}. \qquad (1.35)$$

Substituting $|v_z(0)| = |w_0| = \sqrt{2E_z}$ and using $f(\sqrt{2E_z}) = f(w_0)$, one obtains:

$$\nu_i(z) = 2\int_{\sqrt{2\Phi}}^{\infty} \frac{f(w_0)w_0 dw_0}{\sqrt{w_0^2 - 2\Phi}} \qquad (1.36)$$

where $w_0 = v_z(0)$ is the vertical velocity at the midplane.

Similarly to the MA method, Holmberg & Flynn (2000) model the visible matter density as a superposition of *isothermal components* (equation 1.25). In addition, they constrain the local dark matter density to be consistent with the extrapolation from the *rotation curve*, assuming a spherical halo. This assumptions on the visible and dark matter densities allow them to compute the gravitational potential $\Phi(z)$ through the Poisson equation 1.20. They then use the tracers' observed velocity distribution in the Galactic plane – $f(w_0)$ – and $\Phi(z)$ to predict their density fall-off $\nu(z)$ through equation 1.36. The comparison between the observed and the predicted density fall-off allow them to evaluate the goodness of their fitting parameters.

1.2.2.5 The KG method

Kuijken & Gilmore (1989)'s approach relies on the same key assumption about the distribution function as the HF method. In most studies, the density $\nu(z)$ of the tracers is known to better precision than the velocity distribution $f_z(v_z, z)$. For this reason, Kuijken & Gilmore (1989) work in the opposite direction with respect to Holmberg & Flynn (2000, 2004) and predict $f_z(v_z, z)$ from the observed $\nu(z)$. Applying an inverse Abel transform to equation 1.34, they obtain:

$$f_z(E_z) = \frac{1}{\pi}\int_{E_z}^{\infty} \frac{-d\nu/d\Phi}{\sqrt{2(\Phi - E_z)}} d\Phi. \tag{1.37}$$

so there is a unique relation between $\nu(\Phi)$ and $f_z(E_z)$. Notice that $f_z(E_z)$ depends on $\nu(\Phi(z))$ only at large z, where the potential exceeds E_z, i.e. beyond $z = \Phi^{-1}(E_z)$. Thus an additional key advantage of the KG method is that one can model the potential at large distances from the Galactic plane, ignoring the detailed distribution of matter at small z. Instead of solving the Poisson equation for a given visible mass model, Kuijken & Gilmore (1989) parameterise the gravitational potential $\Phi(z)$ above the bulk of the disc matter (where it is sensitive only to the total surface density of gravitating matter) as:

$$\Phi(z) = K(\sqrt{z^2 + D^2} - D) + Fz^2 \tag{1.38}$$

where D is the disc scale height, K is proportional to the total disc surface density $\Sigma(R_\odot)$, and $F \propto \rho_{\mathrm{dm}}^{\mathrm{eff}}$ (the effective halo density). Kuijken & Gilmore (1989) use a range of Galactic mass models (calculated using different values of the disc mass M, the radial disc scale-length R_d, the circular velocity $V_\mathrm{c}(R_\odot)$ and Sun position $R_\odot$) to *ensure* consistency with the Galactic *rotation curve* (assuming a spherical Milky Way halo) and therefore to obtain a relation between F and K. Note that already this is different from the MA approach where we use no information about the rotation curve to constrain our mass models.

Given the observed space density of a tracer population $\nu(z)$ and a set of gravitational potential models $\Phi(z)$, one can solve equation 1.37. To reduce the noise in the differential of $\nu(z)$, Kuijken & Gilmore (1989) fitted it with a double exponential. They then used the $f_z(E_z)$ derived for each potential model $\Phi(z)$ to compute the likelihood of the spectroscopic sample:

$$\mathcal{L} = \prod\nolimits_{*} \frac{f_z(E_{z,*})}{\int_0^\infty f_z(E_z) dE_z} \tag{1.39}$$

where the product is over all stars in the spectroscopic sample, and select the potential parameters that maximise this likelihood function $\mathcal{L}$.

Outline

This thesis is organised as follows:

- In Chapter 2, I present a new method (the Minimal assumption method – MA method) developed for measuring the local dark matter density from the vertical kinematics of tracers. I use a high resolution simulation of a Milky Way like galaxy as a mock data set to test this new method and compare it with previous methods in the literature. This chapter has been published in MNRAS in 2011 (Garbari et al., 2011), in collaboration with Justin Read and George Lake.

- In Chapter 3, I apply the MA method to real data to obtain a new unbiased determination of the local dark matter density. I choose the K dwarf stars sample from Kuijken & Gilmore (1989) and present our new re-calibration of the photometric distances of these tracers. I use the high resolution simulation presented in Garbari et al. (2011) to test the performance of the MA method with distance and velocity uncertainties, as in the real data. Finally I present our new result. This chapter has been published in MNRAS in 2012 (Garbari et al., 2012), in collaboration with Chao Liu, Justin Read and George Lake.

- In Chapter 4 I present a new ongoing project to map – for the first time – the dark matter density over a large region of the Milky Way disc plane. Having a measure of $\rho_{\rm dm}$ at different radial positions could allow us to detect/constrain the possible presence of a dark disc in our Galaxy. I run two N-body simulation of mergers between a Milky Way like galaxy and a satellite, with two different orbit inclinations. I use the N-body simulations to test how the MA method work at different radial position in the disc and in particular to understand how non-equilibrium features at large R, such as flares and warps, can affect the recovery of the dark matter density. Then I present the data set we choose for mapping $\rho_{\rm dm}$; the analysis of those data is still ongoing. This chapter presents the results of the semester project "Mapping the dark matter density in the Milky Way disc" accomplished by David von Rickenbach (ETH Zurich), supervised by me and Justin Read. The simulations used for the tests have been set up and run by me; the numerical implementation of the MA method has been done by me. David von Rickenbach accomplished the analysis of the simulation and applied the method to them. The data analysis is made in collaboration with Chao Liu.

- Finally, in Chapter 5, I present my conclusions.

1.3 Appendix

1.3.1 Abel Integral

Calculation of the Abel integral of the distribution function:

$$\nu(z) = \int_{-\infty}^{+\infty} dv_z f(E_z) = 2\int_{0}^{+\infty} dv_z f\left(\frac{1}{2}v_z^2 + \Phi(z)\right); \tag{1.40}$$

so

$$v_z = \sqrt{2E_z - 2\Phi(z)} \quad \rightarrow \quad dv_z = \frac{dE_z}{\sqrt{2E_z - 2\Phi(z)}} \tag{1.41}$$

and finally:

$$\begin{aligned} \nu_z &= 2\int_{0}^{+\infty} \frac{dE_z f(E_z)}{\sqrt{2E_z - 2\Phi(z)}} = \qquad \leftarrow dE_z = \sqrt{2E_z}d(\sqrt{2E_z}) && (1.42)\\ &= 2\int_{0}^{+\infty} \frac{f(\sqrt{2E_z})\sqrt{2E_z}d\sqrt{2E_z}}{\sqrt{2E_z - 2\Phi(z)}} = \qquad \leftarrow w_0 = \sqrt{2E_z} && (1.43)\\ &= 2\int_{0}^{+\infty} \frac{f(w_0)w_0 dw_0}{\sqrt{w_0^2 - 2\Phi(z)}} && (1.44) \end{aligned}$$

where $|w_0| = |v_z(0)| = \sqrt{2E_z}$ is the velocity of the tracers in the midplane of the Galaxy.

Chapter 2

Limits on the local dark matter density

This chapter has been published
in MNRAS 416, 2318-2340, 2011 (Garbari et al., 2011)
its authors are Silvia Garbari, Justin I. Read and George Lake.

Abstract

We revisit systematics in determining the local dark matter density $\rho_{\rm dm}$ from the vertical motion of stars in the Solar Neighbourhood. Using a simulation of a Milky Way like galaxy, we determine the data quality required to detect $\rho_{\rm dm}$ at its expected local value. We introduce a new method for recovering $\rho_{\rm dm}$ that uses moments of the Jeans equations, combined with a Monte Carlo Markov Chain technique to marginalise over the unknown parameters. Given sufficiently good data, we show that our method can recover the correct local dark matter density even in the face of disc inhomogeneities, non-isothermal tracers and a non-separable distribution function. We illustrate the power of our technique by applying it to *Hipparcos* data. We first make the assumption that the A and F star tracer populations are isothermal. This recovers $\rho_{\rm dm} = 0.003^{+0.009}_{-0.007}\,{\rm M}_\odot\,{\rm pc}^{-3}$ ($\rho_{\rm dm} = 0.11^{+0.34}_{-0.27}{\rm GeV}\,{\rm cm}^{-3}$, with 90 per cent confidence), consistent with previous determinations. However, the vertical dispersion profile of these tracers is poorly known. If we assume instead a non-isothermal profile similar to the recently measured blue disc stars from SDSS DR-7, we obtain a fit with a very similar χ^2 value, but with $\rho_{\rm dm} = 0.033^{+0.008}_{-0.009}\,{\rm M}_\odot\,{\rm pc}^{-3}$ ($\rho_{\rm dm} = 1.25^{+0.30}_{-0.34}{\rm GeV}\,{\rm cm}^{-3}$ with 90 per cent confidence). This highlights that it is vital to measure the vertical dispersion profile of the tracers to recover an unbiased estimate of $\rho_{\rm dm}$.

2.1 Introduction

There are two approaches to determine the local dark matter density: extrapolating its value from the Milky Way's rotation curve ($\rho_{\rm dm,ext}$; e.g. Sofue et al., 2009; Weber & de Boer, 2010); and using the kinematics of stars in the Solar Neighbourhood ($\rho_{\rm dm}$; e.g. Oort, 1932, 1960). The first requires an assumption about the global and local shape of the dark matter halo. Simple extrapolations that assume spherical symmetry, find $\rho_{\rm dm,ext} \simeq 0.01\,{\rm M_\odot pc^{-3}}$ (Sofue et al., 2009). However, uncertainties about the halo shape lead to errors of at least a factor of two (Weber & de Boer, 2010). Even larger uncertainties arise if the Milky Way has a dark matter disc (Lake, 1989; Read et al., 2008) as predicted by recent cosmological simulations. The second approach relies on fewer assumptions, and this is our focus in this paper. However, both approaches are complementary and, together, provide a powerful probe of Galactic structure. If $\rho_{\rm dm} < \rho_{\rm dm,ext}$, this suggests a prolate dark matter halo for the Milky Way; while $\rho_{\rm dm} > \rho_{\rm dm,ext}$ could imply either an oblate halo or a dark matter disc (Lake, 1989; Read et al., 2008; Read et al., 2009).

The local dark matter density is needed for direct dark matter search experiments. In the simplest case where the dark matter is a Weakly Interacting Massive Particle, or WIMP (Jungman et al., 1996; Baudis, 2006), these experiments produce results that are degenerate between the WIMP interaction cross section and the local matter density (Gaitskell, 2004; Aprile et al., 2005; CDMS Collaboration, 2009). Thus, extracting WIMP properties requires knowledge of $\rho_{\rm dm}$ (e.g. Gaitskell, 2004).

To date, most limits on WIMP properties have assumed the 'Standard Halo Model' (hereafter SHM) density: $\rho_{\rm dm}(R_\odot) = 0.3\,{\rm GeV\,cm^{-3}}$ ($\simeq 0.008\,{\rm M_\odot\,pc^{-3}}$; Jungman et al., 1996)[1]. This is similar to the latest rotation curve extrapolated values that assume a spherical Milky Way halo. However, if the Milky Way halo is oblate, or there is a dark matter disc, then this could be a significant underestimate (e.g. Weber & de Boer, 2010).

Measuring the local matter and dark matter density from the kinematics of Solar Neighbourhood stars has a long history dating back to Oort (Oort, 1932, 1960) who determined the total matter density $\rho_{\rm tot}(R_\odot)$. Many studies since

---

[1] $1\,{\rm GeV\,cm^{-3}} \simeq 0.0263158\,{\rm M_\odot\,pc^{-3}}$. The SHM is an isothermal sphere model for the Milky Way's dark matter halo with a value of the dark matter velocity dispersion assumed to be $\sigma_{\rm iso} \simeq 270\,{\rm km\,s^{-1}}$.

then have revisited the determination of both $\rho_{\rm tot}$ and $\rho_{\rm dm}$; we summarise recent results from the literature in Figure 2.1.

We can see from Figure 2.1 that results have converged on no or very little disc dark matter[2]. In addition to the local volume density, several studies have measured the dynamical *surface density* of all gravitating matter – $\Sigma_{\rm tot,L}$ – rather than the volume density, typically probing up to heights of about $L \sim 1\,{\rm kpc}$ above the Galactic disc (e.g. Kuijken & Gilmore, 1991; Holmberg & Flynn, 2004). If we assume a constant dark matter density over this range, we can estimate the local volume density as $\rho_{\rm dm} = (\Sigma_{\rm tot,L} - \Sigma_{\rm s,L})/L$. This gives[3] $\rho_{\rm dm} = 0.013 \pm 0.006\,{\rm M}_\odot\,{\rm pc}^{-3}$ for an exponential and $\rho_{\rm dm} = 0.008 \pm 0.006\,{\rm M}_\odot\,{\rm pc}^{-3}$ for a sech^2 disc profile, respectively.

The uncertainties on $\rho_{\rm tot}$ and $\rho_{\rm dm}$ quoted in Figure 2.1 owe only to the sample size and observational errors. With current/future surveys like GAIA (Jordan, 2008; Bailer-Jones, 2009), RAVE (Steinmetz, 2003; Steinmetz et al., 2006; Zwitter et al., 2008) and SEGUE (Yanny et al., 2009) we expect a dramatic improvement in the number of precision astrometric, photometric and spectroscopic measurements. With this explosion in data, it is timely to revisit the systematic errors in determining $\rho_{\rm dm}$ from Solar Neighbourhood stars since these will become the dominant source of error, if they are not already. This is the goal of this paper.

Previous work in the literature has examined some of the possible systematics. Statler (1989) approximated the Galactic potential with a Stäckel potential

---

[2] We should be careful about what we mean by the terms 'local dark matter' and 'dark matter disc'. In simulations, the dark matter disk has a scaleheight of $\sim 1-2\,{\rm kpc}$ (Read et al., 2008), but most importantly, it is just intermediate between the disc ($z_0 \sim 250\,{\rm pc}$) and the halo which has an effective scaleheight of $\sim R_\odot$. Here, we use 'local dark matter' to mean dark matter within a local volume probed by the motions of stars in the solar neighborhood. Since this will only probe $\rho_{\rm dm}$ to $|z| \sim 1\,{\rm kpc}$, we can only separate a dark disk from a dark halo using another estimate of the dark matter halo's density. In the past, studies have talked about 'disk dark matter' and meant dark matter with a scaleheight similar to the stellar disk. Here, we would consider that to be just normalizing our stellar mass distribution rather than being a dark matter component.

[3] We derive the surface density of the visible matter at L as $\Sigma_{{\rm s},L} = \Sigma_{{\rm thin},L} + \Sigma_{{\rm thick},L}$, where

$$\Sigma_{i,L} = 2\int_0^L \rho_i(0)F(z)dz$$

with i = thin, thick – for the thin and the thick disc and $F(z) = \exp(-z/z_{0,i})$ or $F(z) = {\rm sech}^2(z/z_s)$ if we consider exponential or sech^2 disc, respectively. The densities at the midplane $\rho_i(0)$ are taken from Table 2.4 and the exponential (sech^2) disc scale heights $z_{0,i}$ ($z_{s,i}$) are calculated from the values in Table 2.2. The cited values of $\rho_{\rm dm}$ is obtained from a simple average of $\rho_{\rm dm}$ obtained using the dynamical $\Sigma_{\rm tot}$ from Kuijken & Gilmore (1991) and Holmberg & Flynn (2004).

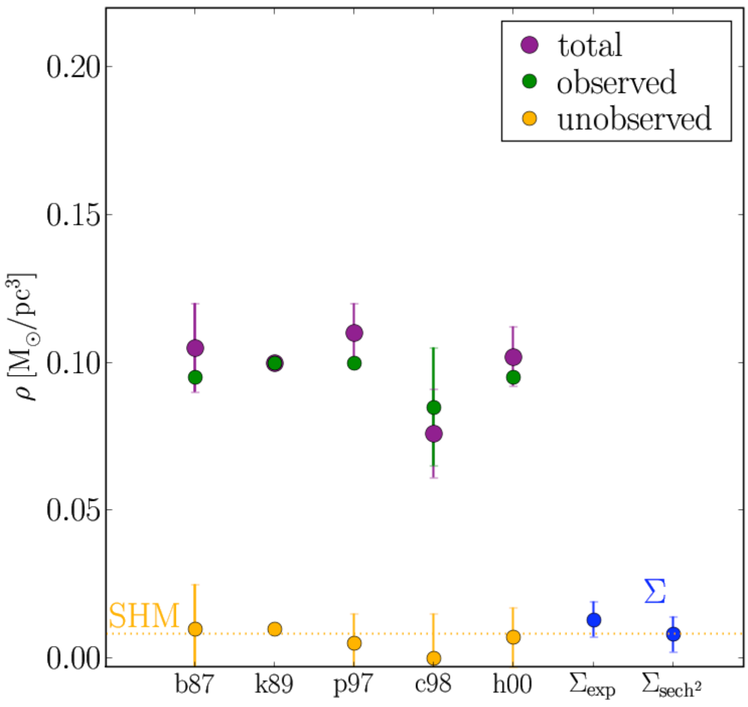

Figure 2.1: A summary of recent determinations of total density $\rho_{\rm tot}$ (purple), dark matter density $\rho_{\rm dm}$ (yellow) and observed matter density (green) from the kinematics of Solar Neighbourhood stars in the literature. The yellow dotted line represents the dark matter density in the SHM. The blue points are the values of $\rho_{\rm dm}$ calculated from the local surface density (using an exponential and a sech^2 profile for the disc; see footnote 2). Data are taken from: b87: Bienayme et al. (1987); k89: Kuijken & Gilmore (1989); p97: Pham (1997); c98: Crézé et al. (1998); h00: Holmberg & Flynn (2000).

(Stäckel, 1895) and used the analytic third integral to treat cross terms in the Jeans equations. He applied this method to artificial data superficially resembling data available at the time, finding that systematic uncertainties were at least 30 per cent, due mainly to sample size and uncertainties in the rotation curve. Kuijken & Gilmore (1989a) reconsidered the determination of the volume density near the Sun with particular emphasis on possible systematic effects in the analyses of local F and K stars. They focused on the importance of modeling the velocity distribution of the stars near the plane (important for their method that assumes that the distribution function is separable; see Section 2.2), and determining the density distribution as a function of height z above the plane.

In this paper, we study systematic errors using high resolution N-body simulations. We first build an equilibrium N-body model approximating the Milky Way that satisfies all of the usual assumptions made in determining ρ_{dm} – vertical isotropy in the velocity distribution, separability of the Galactic potential, constant local dark matter density and negligible radial gradient in the tilt of the velocity ellipsoid. We then evolve the disc over several dynamical times to form an inhomogeneous and complex disc structure that includes a strong bar and spiral waves similar to the Milky Way (Drimmel & Spergel, 2001; Dehnen, 2002; Binney & Tremaine, 2008). This breaks many of the usual assumptions, providing a stringent test of different techniques. We first use our simulation to test a standard method in the literature for recovering ρ_{dm}. We then present and test a new method that: (i) relies only on a 'minimal' set of assumptions; and (ii) that uses a Monte Carlo Markov Chain (MCMC) technique to marginalise over unknown parameters. The former makes the method – given good enough data – robust to model systematics. The latter allows us to cope with incomplete or noisy data and model degeneracies. Finally, we apply our new method to data from the literature to obtain a new measure of both ρ_{tot} and ρ_{dm}.

This paper is organised as follows. In Section 2.2, we review the basic equations of the method and the assumptions used in past work. We present two methods that we test in detail: the 'HF' method proposed by Fuchs & Wielen (1993) and developed by Holmberg & Flynn (2000); and a new more general method that assumes only equilibrium. In Sections 2.3, we describe the simulation that we use to test these two methods and we confront the different methods with our simulated Milky Way to assess the systematic uncertainties. In Section 2.4, we apply our new method to data from the literature to determine more realistic errors on the local dark matter density. Finally in Section 2.5, we present our conclusions.

2.2 Determining the Local Matter Density

Ideally, we should solve the Vlasov-Poisson equations to obtain the gravitational potential Φ from the distribution function of stars $f(\mathbf{x}, \mathbf{v})$:

$$\frac{\partial f}{\partial t} + \nabla_x f \mathbf{v} - \nabla_v f \nabla_x \Phi = 0 \tag{2.1}$$

$$\nabla^2 \Phi = 4\pi G \rho_{\rm tot} \tag{2.2}$$

where G is the gravitational constant; $\rho_{\rm tot}$ is the *total* matter density; and the density of tracers ν follows from the distribution function: $\nu = \int d^3\mathbf{v} f(\mathbf{x}, \mathbf{v})$. If the system is in equilibrium, we may also assume that it is in a steady state such that $\frac{\partial f}{\partial t} = 0$.

However, equations (2.1) and (2.11) are difficult to solve in practice. The distribution function is six dimensional, requiring full phase space information. Worse still, we require its derivatives which amplifies any noise in the data (even a million stars will sample only ten points per phase space dimension). As a result, there have been two types of methods proposed in the literature: take velocity moments of the Vlasov equation and solve the resulting Jeans equations (e.g. Bahcall, 1984a,b,c); or guess the form of the distribution function and ask if the data are consistent with this (Kuijken & Gilmore, 1989b; Kuijken & Gilmore, 1989; Kuijken & Gilmore, 1989a). The first method has the advantage that we need not specify f, since we constrain it only through its moments. However, it throws away information about the shape of f. The latter method maximises the available information but comes at the price of potentially fatal systematic errors if an incorrect form for f is assumed. Some mixed methods have also been proposed where the Jeans-Poisson system is solved, but the tracer density is closed by an integral over the measured (planar) distribution function (Fuchs & Wielen, 1993; Flynn & Fuchs, 1994).

In this paper, we focus on the moment based methods that solve the Jeans-Poisson system of equations. This is because we want to make as few assumptions as possible to combat systematic errors. We do, however, also test the mixed method proposed by Fuchs & Wielen (1993) and applied to *Hipparcos* data by Crézé et al. (1998) and Holmberg & Flynn (2000). This allows us to evaluate systematic errors introduced by assumptions about the form of f.

In the following sections, we review methods for recovering $\rho_{\rm s}$ (the in-plane disc matter density) and $\rho_{\rm dm}$ from the simultaneous solution of the Jeans and Poisson equations. We present first a new method based on minimal assumptions – our 'MA' method. We then derive the method used in Holmberg & Flynn (2000) as a special case – the 'HF' method. We test both the MA and the HF methods on our Milky Way like simulation in Section 2.3.

2.2.1 The Minimal Assumption method (MA)

The Jeans equations in cylindrical coordinates follow from velocity moments of the steady state Vlasov equation (equation 2.1; Binney & Tremaine, 2008). Consider first just the z Jeans equation:

$$\frac{1}{R}\frac{\partial}{\partial R}\left(R\nu_i\overline{v_{R,i}v_{z,i}}\right) + \frac{\partial}{\partial z}\left(\nu_i\overline{v_{z,i}^2}\right) + \nu_i\frac{\partial\Phi}{\partial z} = 0 \tag{2.3}$$

where ν_i, $\overline{v_{z,i}^2}$ and $\overline{v_{R,i}v_{z,i}}$ are the density and the velocity dispersion components of a *tracer* population i moving in potential Φ.

We now introduce our only assumptions:

1. The system is in equilibrium (steady state assumption).
2. The dark matter density is constant over the range of $|z|$ considered.
3. The 'tilt' term: $\frac{1}{R}\frac{\partial}{\partial R}\left(R\nu_i\overline{v_{R,i}v_{z,i}}\right)$ is negligible compared to all other terms.

The first assumption is necessary for any mass modelling method (e.g. Sánchez-Salcedo et al., 2011). The second assumption requires that the disc scale height is much smaller than the dark matter halo scale length $z_d \ll r_h$, or for disc-like dark matter, that the scale height of dark disc is significantly larger than z_d.

Binney & Tremaine (2008) show that the 'tilt' term is likely smaller than $(\overline{v_R^2} - \overline{v_z^2})(z/R)$ (see their discussion of the asymmetric drift in §4.8.2a and §4.9.3); so, assuming that $\overline{v_R^2}$ and $\overline{v_z^2}$ both decline with R as $\exp(-R/R_d)$ (applying also for our simulation, at least in the early stage, by construction), then the *tilt term* in equation 2.3 is constrained by:

$$\left|\frac{1}{R}\frac{\partial(R\nu\overline{v_R v_z})}{dR}\right| \simeq \frac{2\nu}{R_d}\overline{v_R v_z} \lesssim \frac{2\nu z}{R_d}\frac{\overline{v_R^2}-\overline{v_z^2}}{R_\odot} \tag{2.4}$$

The second term in equation 2.3 is of the order of $\nu\overline{v_z^2}/z_d$ where $z_d \ll R_\odot$ and $z_d \ll R_d$ is the disc scale height. Hence the neglected term is smaller then the second term by at least a factor of $2zz_d/(R_d R_\odot)$. For these reasons we define these assumptions as a 'minimal' set.

With the above assumptions, equation 2.3 becomes a function only of z and we can neglect the other two Jeans equations in R and θ. Our remaining Jeans equation becomes:

$$\overline{v_{z,i}^2}\frac{\partial\nu_i}{\partial z} + \nu_i\left(\frac{\partial\Phi}{\partial z} + \frac{\partial\overline{v_{z,i}^2}}{\partial z}\right) = 0; \tag{2.5}$$

This is the Jeans equation for a one-dimensional slab. In principle, we should solve it for $R =$ constant. However, in practice we must average over some range ΔR. We examine what is the maximum tolerable value of ΔR in Section 2.3.3.1.

For a given tracer population i, we can now write:

$$\frac{d\nu_i}{\nu_i} = -\frac{1}{\overline{v_{z,i}^2}}d(\overline{v_{z,i}^2} + \Phi) \tag{2.6}$$

which can be solved straightforwardly:

$$\log\left(\frac{\nu_i}{\nu_i(0)}\right) = -\log\left(\frac{\overline{v_{z,i}^2}}{\overline{v_{z,i}^2}(0)}\right) - \int_0^z \frac{1}{\overline{v_{z,i}^2}}\frac{d\Phi}{dz}dz \tag{2.7}$$

Thus, at each height above the disc z_*, the density of the tracer population $\nu_i(z_*)$ can be calculated:

$$\frac{\nu_i(z_*)}{\nu_i(0)} = \frac{\overline{v_{z,i}^2}(0)}{\overline{v_{z,i}^2}(z_*)}\exp\left(-\int_0^{z_*}\frac{1}{\overline{v_{z,i}^2}(z)}\frac{d\Phi}{dz}dz\right) \tag{2.8}$$

This general equation for $\nu_i(z)$ can be used to describe all the visible components of the disc. Given the density at the midplane $\nu_i(0)$ and the vertical velocity dispersion $\overline{v_{z,i}^2}(z)$ as a function of z for each of the gas and stellar populations in the local disc, we can model the full disc density distribution as:

$$\rho_{\rm s}(z) = \sum_i m_i^* \nu_i(0) \frac{\overline{v_{z,i}^2}(0)}{\overline{v_{z,i}^2}(z)} \exp\left(-\int_0^z \frac{1}{\overline{v_{z,i}^2}} \frac{d\Phi}{dz} dz\right). \tag{2.9}$$

where m_i^* is the mass-to-light ratio for a given population i. The Poisson equation then determines the potential Φ from the density. In cylindrical polar coordinates this is given by:

$$\begin{aligned} 4\pi G\rho &= \frac{\partial^2\Phi}{\partial z^2} + \frac{1}{R}\frac{\partial}{\partial R}\left(R\frac{\partial\Phi}{\partial R}\right) \\ &= \frac{\partial^2\Phi}{\partial z^2} + \frac{1}{R}\frac{\partial V_c^2(R)}{\partial R} \end{aligned} \tag{2.10}$$

where ρ is now the *total mass density* and $V_c(R)$ is the circular velocity at radius R.

Splitting the matter density ρ into disc contributions (gas+stars) that vary with z ($\rho_{\rm s}(z)^4$), and an effective dark matter contribution that includes the circular velocity term ($\rho_{\rm dm}^{\rm eff}$), the Poisson equation becomes:

$$\frac{\partial^2\Phi}{\partial z^2} = 4\pi G(\rho_{\rm s}(z) + \rho_{\rm dm}^{\rm eff}) \tag{2.11}$$

with:

$$\rho_{\rm dm}^{\rm eff} = \rho_{\rm dm}(R) - (4\pi GR)^{-1}\frac{\partial}{\partial R}V_c^2(R) \tag{2.12}$$

where $\rho_{\rm dm}(R)$ is the halo mass density (following assumption 2, this is assumed to be independent of z in the volume considered); and $V_c(R)$ is the (total) circular velocity at a distance R (in the plane) from the centre of the Galaxy. For a flat rotation curve, the second term vanishes and $\rho_{\rm dm}^{\rm eff}(R) = \rho_{\rm dm}(R)$. Note that there is an important difference between the vertical velocity dispersion of a tracer population, $\overline{v_{z,i}^2}(z)$ in equation 2.8, and the same quantity as it appears in the mass model (equation 2.9). The former is something that we must measure for our chosen tracers, while the latter is simply a parameter that appears in our disc mass model. To put it another way, the tracers *must* satisfy equation 2.8, but we could replace equation 2.9 with some other mass model for the disc.

We may now solve equations 2.9 and 2.11 numerically for a given tracer pop-

---

[4] Note that we use throughout the notation $\rho_s = \rho_s(0)$ – the in-plane baryonic mass density.

ulation. We adopt the following procedure: first, we make initial trial guesses for $\rho_\mathrm{s}(0)$ (and any other unknowns in the star/gas disc), ρ_dm, and the run of vertical velocity dispersion for the tracers $\overline{v_{z,i}^2}(z)$. Next, we solve equation 2.9 to obtain $\Phi(z)$ and its first derivative $\frac{\partial\Phi}{\partial z}$, with $\Phi(0) = \frac{\partial\Phi}{\partial z}\big|_0 = 0$. Then, we plug this result into equation 2.8 to obtain the vertical density fall-off the tracers $\nu_i(z)$. Finally, this is compared with the observed distribution to obtain a goodness of fit. In principle, each tracer population gives us an independent constraint on $\Phi(z)$. A useful consistency check then follows since all tracers should yield the same potential, while combining different tracers gives smaller errors on the derived parameters. Note that the above procedure requires many input parameters that are typically poorly constrained, for example the normalisations and dispersions of each of the disc components and the vertical dispersion profile of the tracers. To efficiently explore this parameter space and marginalise over the uncertainties, we use a Monte Carlo Markov Chain (MCMC) method. This is described in Section 2.2.3.

Our Minimal Assumption (MA) method requires a measurement of $\overline{v_{z,i}^2}(z)$ for each tracer population considered. The HF method we derive next does not require $\overline{v_{z,i}^2}(z)$ – using an additional assumption of separability instead. This has several advantages, but comes with a risk that this additional assumption will lead to systematic bias. We examine this in detail in Section 2.3.

2.2.2 The Holmberg and Flynn method (HF)

The HF method Fuchs & Wielen (1993); Holmberg & Flynn (2000) adds four additional assumptions:

1. The potential is separable: $\Phi(R, z) = \Phi(R) + \Phi(z)$
2. The distribution function of tracers also separates. At a fixed cylindrical radius in the disc, it is a function only of the vertical energy: $f = f(E_z)$.
3. All disc components are isothermal.
4. The rotation curve contribution to the Poisson equation – $(4\pi GR)^{-1}\frac{\partial}{\partial R}V_c^2(R)$ – is negligible. Thus $\rho_\mathrm{dm} = \rho_\mathrm{dm}^\mathrm{eff}$ by construction.

The first two assumptions are critical for the method and also lie at the heart of the method proposed by Kuijken & Gilmore (1989b). Thus testing their validity applies to a wider range of past methods. Note that if these two assumptions are satisfied, then the 'tilt' term in the Jeans equation is exactly zero, thus perfectly satisfying assumption 3 of the MA method. However, the MA method makes the weaker assumption that the tilt term is *small* as compared to the other terms in the Jeans equations. Unlike the HF method, it requires no assumptions about the form of the potential or the distribution function. It is the latter that is the key difference between the two. If the motion is not separable, then the distribution function cannot be approximated by $f = f(E_z)$. As we will demonstrate in Section 2.3, this assumption leads to significant systematic errors even at ~ 1.5 disc scale heights above the plane. By contrast, assuming that the tilt term is simply small appears to be robust even up to several disc scale heights[5].

The HF method is a mixed method that uses the Jeans equations (as in the MA method), but assumes that each disc component is isothermal. This gives a Jeans equation as a function of z similar to that in the MA method:

$$\overline{v_{z,i}^2}\frac{\partial \nu_i}{\partial z} + \nu_i \frac{\partial \Phi(z)}{\partial z} = 0 \tag{2.13}$$

which is independent of R and can then be straightforwardly solved to give:

$$\nu_i = \nu_{0,i} \exp\left(-\frac{\Phi(z)}{\overline{v_{z,i}^2}}\right) \tag{2.14}$$

where $\nu_{0,i} = \nu_i(0)$.

Thus, the density of the disc ρ_s can be written as a sum over isothermal components:

$$\rho_\mathrm{s}(z) = \sum_i m_i^* \nu_{i,0} \exp\left(-\frac{\Phi(z)}{\overline{v_{z,i}^2}}\right) \tag{2.15}$$

where m_i^* is the mass-to-light ratio for a given population i. With the above decomposition, non-isothermality can still be modeled as a linear combinations of a larger number of isothermal distributions (Bahcall, 1984a). However, this expansion is degenerate, and introduces many additional parameters that become expensive to explore (Kuijken & Gilmore, 1989b).

---

[5] Note that should the tilt term become large then in principle we could correct for it in the Jeans equation. This is perfectly possible in the MA method, but problematic for the HF method. In the HF method we would also have to correct for it in the distribution function. Such tilt corrections are, however, beyond the scope of this paper.

Plugging equation 2.15 into the Poisson equation 2.11, we can then calculate the gravitational potential, assuming a constant contribution for the dark matter density.

As in our MA method, the HF equations are closed by comparing the observed fall-off of the tracer population with the predicted one (given an initial guess of the disc model and dark matter density parameters). However, instead of using the solution to the moment equation 2.8 (or 2.14), they calculate the density fall-off of the tracers from the integral of the distribution function (Fuchs & Wielen, 1993; Flynn & Fuchs, 1994). Here they use the additional assumptions (reasonable close to the midplane) that the potential is separable: $\Phi(R,z) = \Phi(R) + \Phi(z)$ and that the distribution function of tracers is a function only of the vertical energy: $f = f(E_z)$. This has two key advantages. Firstly, it maximises the use of information in the data since it uses the *shape* of the distribution function, rather than just its lowest moments as in the MA method above. Secondly, one needs only measure f at one height z above the disc: $\overline{v_{z,i}^2}(z)$ is not required. We may understand this as follows. The density of the tracers is given by:

$$\nu_i(z) = \int_{-\infty}^{\infty} dv_z f(E_z) = 2\int_0^{\infty} dv_z \left[f\left(\frac{1}{2}v_z^2 + \Phi\right)\right] \tag{2.16}$$

And, since $f = f(E_z)$, we can rewrite equation 2.16 as an Abel integral:

$$\nu_i(z) = 2\int_{\Phi(z)}^{\infty} d(\sqrt{2E_z})\sqrt{2E_z}\frac{f(\sqrt{2E_z})}{\sqrt{2\,(E_z - \Phi)}}. \tag{2.17}$$

Then, substituting $|w_0| = \sqrt{2E_z}$ and using $f(\sqrt{2E_z}) = f(w_0)$, we obtain:

$$\nu_i(z) = 2\int_{\sqrt{2\Phi}}^{\infty} \frac{f(w_0)w_0 dw_0}{\sqrt{w_0^2 - 2\Phi}} \tag{2.18}$$

where w_0 is the vertical velocity of stars in the midplane ($z = 0$). Thus, we can measure $f(E_z)$ – valid for all height about the disc z – from $f(|w_0|)$ measured only in the disc plane.

Note that the above does not assume that the tracers are isothermal, though the mass model (equation 2.15) does. This will become inconsistent if the tracers comprise most of the mass of the disc. In practice, this is unlikely to be the case. However, the inconsistency can always be avoided by using the more general mass model derived in the MA method, while still closing the equations using equation

2.18. We test the effect of this inconsistency in Section 2.3.

We stress that the assumption of $f = f(E_z)$ is likely to be valid close to the disc plane. Thus, the HF method as employed in Holmberg & Flynn (2000) – where they probe only up to ~ 1 half mass scale height above the disc – is unlikely to be biased. However, as we probe to heights greater than the disc scale height, systematics will creep in. Furthermore, probing to such heights – as we shall show – is necessary for breaking a degeneracy between ρ_{dm} and ρ_{s}. We explore the effect of the $f = f(E_z)$ assumption in Section 2.3.

2.2.3 Determining ρ_{dm} and ρ_s with an MCMC

In summary, while the MA and HF methods differ in their underlying assumptions, the basic strategy for recovering the local matter density is the same:

1. Build a mass model for the local mass distribution consisting of components ν_i, defined by equation 2.8 or 2.14, for gas and stellar populations, and a constant contribution for dark matter ρ_{dm}.

2. Use this mass model to integrate the Poisson (2.11) and the Jeans equation (2.5 or 2.13) simultaneously to compute the local potential Φ (and its z-derivative).

3. Use the calculated potential Φ and the measured kinematics of the tracers to compute their density fall-off $\nu(z)$ (using equation 2.8 or 2.18). To predict the density fall-off of the tracers the HF method needs the measure of their vertical velocity distribution function in the mid-plane $f(w_0)$, while in the case of the MA method the vertical velocity dispersion as a function of z - $\overline{v_{z,i}^2}(z)$ - is required.

4. Compare the predicted density profile(s) $\nu(z)$ with the observed one(s) $\nu_{\mathrm{obs}}(z)$ to reject or accept the model input parameters: ρ_{dm} and parameters governing each of the components ν_i.

In practical applications, the above implies many (degenerate) free parameters if the disc model has many non-isothermal components with parameters that are poorly known, while $\overline{v_{z,i}^2}(z)$ for the tracers may also be poorly constrained. A Monte Carlo Markov Chain (MCMC) provides an efficient way to rapidly explore this parameter space. It naturally deals with parameter degeneracies: all of the unknown parameters are 'marginalised out' to leave the key parameters of interest in (the total matter density $\rho_{\rm tot}$ and the dark matter density $\rho_{\rm dm}$). In this way, the MCMC addresses some of the issues raised by Kuijken & Gilmore (1989b); Kuijken & Gilmore (1989); Kuijken & Gilmore (1989a) about degeneracies between parameters in very complex models making such models unworkable.

We use a MCMC method based on a Metropolis algorithm (e.g. Saha, 2003) to recover the local density. For the simulation data, we use the dark matter density (namely $\rho_{\rm dm}$ in equation 2.12, adding the rotation curve term calculated for each volume) and the visible matter density $\rho_{\rm s}$ (which correspond to $\nu_{i,0} = m_i^* \nu_i(0)$ in equation 2.9 or 2.15), as our input parameters. When we apply the HF method, we fit the distribution function at the midplane with a Gaussian (double Gaussian) for the unevolved (evolved) simulation. These fits are good for most of the volumes considered (an example is shown in the left panel of Figure 2.2). When we adopt the MA method, we linearly interpolate the velocity dispersion of the tracers above the plane $\overline{v_{z,i}^2}(z)$, since this method is extremely sensitive to the velocity dispersion function adopted.

When we apply the two methods to the real data (see Section 2.4) the situation is more complex. Firstly, we must fit a larger number of parameters: namely the local dark matter density $\rho_{\rm dm}$, the total visible density $\rho_{\rm s}$, the fraction of the different disc components ($\nu_{i,0}$), and their velocity dispersions in (and even potentially above) the plane ($\overline{v_{z,i}^2}$). Secondly, the data are magnitude rather than volume limited. We take this into account by drawing the observed stellar distribution from the model density fall-off using the observed luminosity function. The MCMC allows us to easily implement both these additional parameters and the sampling of the luminosity function. In addition, it is straightforward to model different tracer populations simultaneously, and apply constraints on the local *surface density* of the disc. Our full procedure is described in more detail in Section 2.4. Finally, with real data we cannot simply interpolate the velocity dispersion as a function of z, but we must consider the uncertainties on the velocities. Such uncertainties can be straightforwardly added to the MCMC and marginalised out (see Appendix 2.6.3).

We apply the MA and HF methods to our simulated Milky Ways in Section 2.3. We then apply the MA method to real data in Section 2.4. For the simulation, we calculate the potential by modeling the visible matter in the disc as a single population. To simplify the calculation we introduce some dimensionless

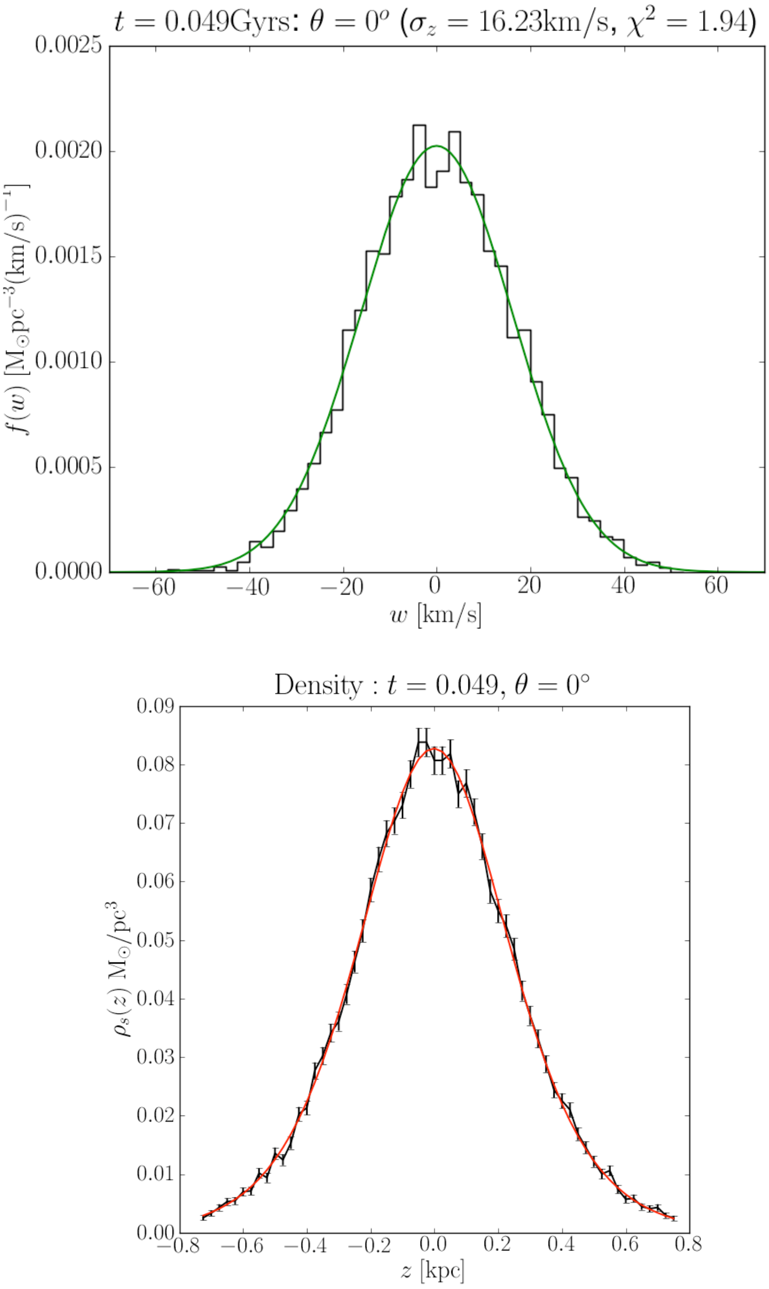

Figure 2.2: *Upper panel:* The vertical velocity distribution of star particles (in black) for one of the "wedge" patches at $R_\odot = 8.5\,\mathrm{kpc}$ from the center of the galaxy. The green curve corresponds to the Gaussian fit. *Lower panel:* The vertical density distribution of star particles (in black) for one of the "wedge" patches at $R_\odot = 8.5\,\mathrm{kpc}$ from the center of the galaxy. The red curve corresponds to the prediction of the best-fitting mass model. The error bars represent Poisson noise.

parameters described in Appendix 2.6.1 (Bahcall, 1984a,b,c). This transforms equations 2.8, 2.14 and 2.11 to 2.34, 2.37 and 2.35.

2.3 Testing the methods

To test the MA and HF methods in Section 2.2 and evaluate the systematic errors, we apply both to a high resolution collisionless simulation of a Milky Way like galaxy.

We consider two different stages of the simulation: an unevolved one with an axisymmetric disc (shown in the left panel of Figure 2.3) and fulfilling all the hypotheses of the more restrictive HF method; and a more evolved stage (represented in Figure 2.3, right panel) presenting a bar, similar to the real Milky Way, that breaks many of the assumptions. The results for these two different stages of the simulation are described in Sections 2.3.3.1 and 2.3.3.2, respectively.

2.3.1 The simulation

We ran a simulation of a Milky Way like galaxy with the parallel tree code PkdGRAV (Stadel, 2001), using the galaxy models of Widrow & Dubinski (2005) for the initial conditions. These models are derived from a composite three-integral distribution function $f = f_{\mathrm{disc}}(E, E_z, L_z) + f_{\mathrm{halo}}(E) + f_{\mathrm{bulge}}(E)$ and provide near-equilibrium initial conditions.

The disc model has an exponential radial profile and a $\mathrm{sech}^2(z/z_{\mathrm{s}})$ vertical profile. Its distribution function applies in the epicyclic approximation with $\sigma_{R,\phi,z} \ll V_c$, so the vertical energy is an approximate integral of motion: this leads to triaxial velocity ellipsoids in the disc models as seen in real spiral galaxies (Widrow et al., 2008). The halo is modeled as a NFW profile. However, when its distribution function is combined with the disc one, the net halo density profile is slightly flattened along the z-axis near the centre, but preserving the r^{-1} central cusp.

To have statistics comparable with the present data in the Solar Neighbourhood (e.g. Holmberg & Flynn (2000) considered ~ 2000 A-stars in a cylindrical volume of radius $R = 200$pc and height $|z| < 200$pc centered on the Sun), we constructed a disc with $n_{\mathrm{d}} = 30 \times 10^6$ star particles. We chose the masses of the dark matter halo particles and the (star) bulge particles so that the heating

Table 2.1: Parameters for the disc, dark matter halo and stellar bulge for the initial conditions of the simulation. From left to right columns show: the number of particles (N); the total mass (M); the softening length (ε); the half mass scale-length ($R_{1/2}$); and the half-mass scale height ($z_{1/2}$).

	N [10^6]	M [10^{10}M$_\odot$]	ε [kpc]	$R_{1/2}$ [kpc]	$z_{1/2}$ [kpc]
Disc	30	5.30	0.015	4.99	0.17
Bulge	0.5	0.83	0.012	-	-
Halo	15	45.40	0.045	-	-

time-scale for the disc is much larger than both the internal relaxation time-scale, and the time of the simulation ($\sim 4\,$Gyr): $t_{\rm heat} \gg t_{\rm rel} \gg t_{\rm sim}$, where $t_{\rm rel}$ is given by (Binney & Tremaine, 2008):

$$t_{\rm rel} = n_{\rm rel} t_{\rm cross} = \frac{n}{8\log\Lambda}\frac{b_{\rm max}}{v_{\rm typ}} \tag{2.19}$$

where $v_{\rm typ} = \sqrt{GM/R_\odot}$ is the typical velocity at the Solar position $R_\odot = 8.5\,$kpc; $b_{\rm min} = 2Gm_{\rm part}/v_{\rm typ}^2$, $b_{\rm max} = R_\odot$; and the Coulomb logarithm is $\log\Lambda = \log(b_{\rm max}/b_{\rm min})$. Given $n_{\rm d} = 30 \times 10^6$ total stars, the number enclosed within $R_\odot$ is $n = n_{\rm d}(R_\odot) \sim 25 \times 10^6$. Using this latter number, we find $t_{\rm rel} \simeq 1.17 \times 10^4\,$Gyr.

The heating time $t_{\rm heat}$ is given by (Lacey & Ostriker, 1985):

$$t_{\rm heat} = \frac{\sigma_z^2 V_{\rm h}}{8\pi G^2 M_{\rm h} \rho_{\rm h} \log\Lambda_{\rm h}} \tag{2.20}$$

where σ_z is the vertical velocity dispersion of the disc particles; $M_{\rm h}$ the mass of the dark matter particles; $V_{\rm h}$ their typical velocity; $\rho_{\rm h}$ and $\log\Lambda_{\rm h}$ are the density and the Coulomb logarithm for the halo (a similar calculation can be done for the bulge particles).

Using $t_{\rm heat} = kt_{\rm rel}$, with $k \sim 10$, we find the following satisfy the above timescale constraints: $n_{\rm h} = 15 \times 10^6$ and $n_{\rm b} = 0.5 \times 10^6$ particles for the halo and the bulge respectively.

The main features of the model we used are listed in Table 2.1. For comparison, some of the corresponding features of the real Milky Way are given in the Table 2.2.

In our analysis, we consider two different outputs of the simulation: an un-

Table 2.2: The distinct components of the Milky Way. From left to right the columns show: the total mass (M); the half mass scale-length ($R_{1/2}$); and the half mass scale height ($z_{1/2}$). These values are compiled using the following relations: $z_{1/2} = 0.55 z_s = 0.7 z_0$ and $R_{1/2} = 1.68 R_0$ (Read et al. 2008), where z_s is the sech^2 disc scale height, z_0 is the exponential disc scale height and R_0 is the exponential disc scale length.

	M $[10^{10}\mathrm{M}_\odot]$	$R_{1/2}$ [kpc]	$z_{1/2}$ [kpc]	Ref.
Thin disc	$3.5 - 5.5^*$	$3.35 - 9.24$	$\sim 0.14 - 0.18$	fl,o,fe,k
Thick disc	-	$5.04 - 7.56$	$0.49 - 0.84$	o,n,s
Bulge	~ 1	-	-	d,fl
Halo	$\sim 40 - 200$	-	-	x,g

References: fl=Flynn et al. (2006); o=Ojha (2001); fe=Feast (2000); k=Kuijken & Gilmore (1989a); n=Ng et al. (1997); s=Spagna et al. (1996); d=Dehnen & Binney (1998); x=Xue et al. (2008); g=Guo et al. (2010).
* total disc mass

evolved stage ($t \sim 50$ Myrs) in which the disc is still axisymmetric, and an evolved one ($t \sim 4$ Gyr) which presents a bar similar to the real Milky Way. These two stages are shown in Figure 2.3 (left and right panels, respectively). The unevolved disc is used to test the method in general, and to study what data are needed to recover the right value of the local density in the ideal case of data fulfilling all the assumptions. The evolved stage represents a more realistic situation and is used to test the effect of realistic disc inhomogeneities on the determination of the local density. The spiral arms – that are the major driver of inhomogeneities at the Solar neighbourhood in the evolved disc – are compatible with the Milky Way: our Galaxy has an inter-arm ratio of the spiral structure at the solar radius $R_\odot$ of $K \sim 1.7$ (Drimmel & Spergel, 2001); the corresponding value for the simulation is $K \sim 1.5$.

In the analysis of the simulation, we set the Solar Neighbourhood position at a Galactocentric distance of $R_\odot = 8.5$ kpc, in agreement with the IAU (International Astronomy Union) recommended value. We consider several small volumes at different angular position around the disc, represented as red circles and wedges in Figure 2.3 (and see Section 2.3.3). For the unevolved (axisymmetric) disc, these different patches test the effect of sampling error on our derived ρ_{dm} and ρ_s; for the evolved disc, they examine the effect of disc inhomogeneities.

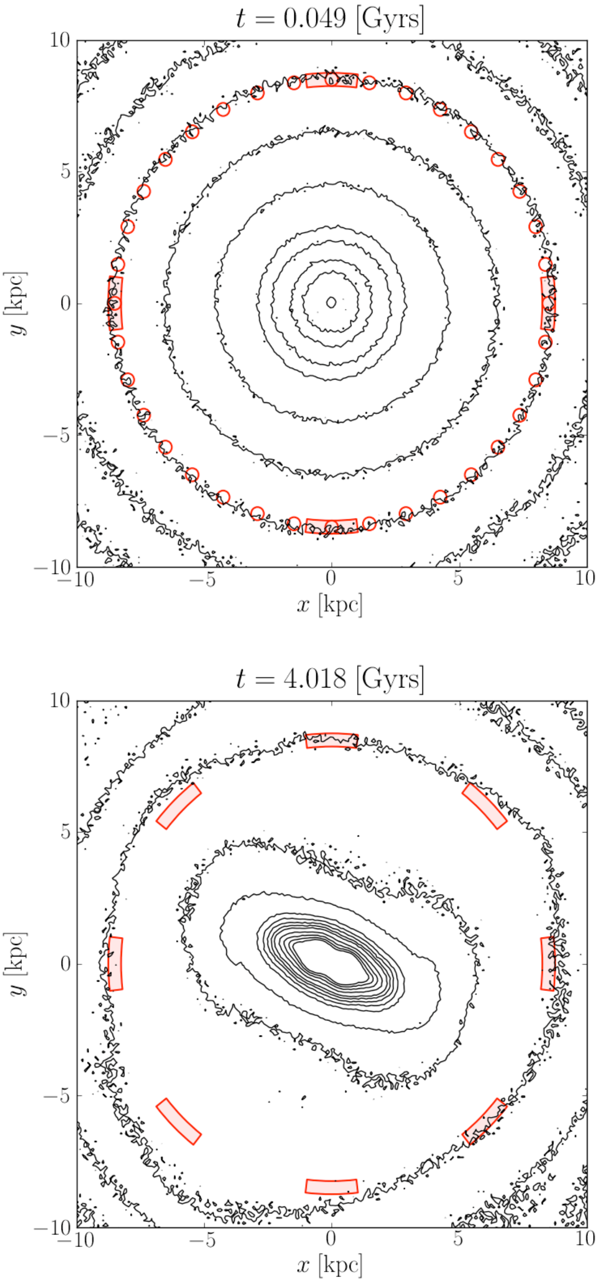

Figure 2.3: Density contours viewed from top for the disc star particles. *Upper panel:* an early time-step ($t \sim 0.05\,\mathrm{Gyr}$) presenting an axisymmetric disc. *Lower panel:* the evolved simulation ($t \sim 4\,\mathrm{Gyr}$), presenting a bar and spiral arms with inter-arm contrast $\rho_{\mathrm{arm}}/\rho_{\mathrm{dip}} \simeq 0.15$. The red circles correspond to the position of the cylindrical "Solar Neighbourhood" patches, at a distance of $R_\odot = 8.5\,\mathrm{kpc}$ from the Galactic Centre. The red shaded wedges represent the other volumes we used to compare the results of the analysis of the two stages of the simulation. We adopt patches of this shape to obtain better sampling. The angular position of the patches is calculated from $x, y = [R_\odot, 0]$ anti-clockwise.

2.3.2 How well does the simulation satisfy our assumptions

Both the MA and HF methods are based on several key assumptions, as outlined in Section 2.2.1 and Section 2.2.2. To understand how well both methods can recover the local dark matter density, we first evaluate how well the two stages of the simulation fulfil these assumptions.

2.3.2.1 Constant ρ_{dm} in the local volume

The hypothesis 2 of the MA method is well fulfilled as shown in Figure 2.4, where we plot the dark matter density as a function of z for the unevolved (left) and the evolved (right) simulation. The purple line represents $|z| = 0.75\,\mathrm{kpc}$, i.e. the maximum height considered in our analysis.

2.3.2.2 Isothermality, tilt and equilibrium

The velocity dispersion $\overline{v_z^2}$ as a function of z should be constant, by definition, for an isothermal population. In the two left panels of Figure 2.5 the velocity dispersion $\overline{v_z^2}(z)$ is represented for the two output times of the simulation considered ($t = 0.049\,\mathrm{Gyr}$ in the upper panel and $t = 4.018\,\mathrm{Gyr}$ in the lower one) at $R = 8.5\,\mathrm{kpc}$ (in red). For comparison, the observational data for the Milky Way (blue data points), and the best fit $\overline{v_z^2}(z)$ function determined by Bond et al. (2010) (green dashed line: the light green shaded region represent the errors in the fit parameter) are shown. Bond et al. (2010)'s fit are obtained from a sample of 53000 blue ($0.2 < g - r < 0.6$) disc stars from SDSS with radial velocity measurements, $b > 20^\circ$ and high metallicity ([Fe/H]> -0.9), up to $|z| < 5\,\mathrm{kpc}$. These stars are taken at high z over the plane and are much hotter than the stars used in literature (A,F and K stars) to trace the local gravitational potential (blue dots). However, the fit does gives us information about the potential non-isothermality of the disc. The dashed yellow line is the isothermal line for 8.5 kpc. These plots refer to a particular angular position in the disc ($\theta = 0^\circ$), but the situation for $\overline{v_z^2}$ is similar for the whole disc.

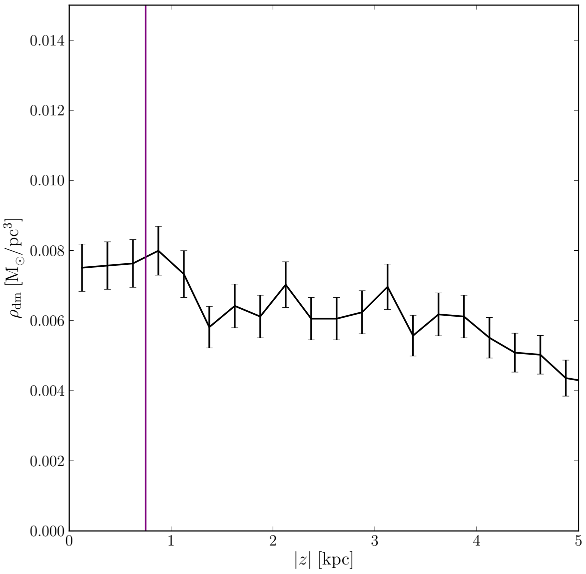

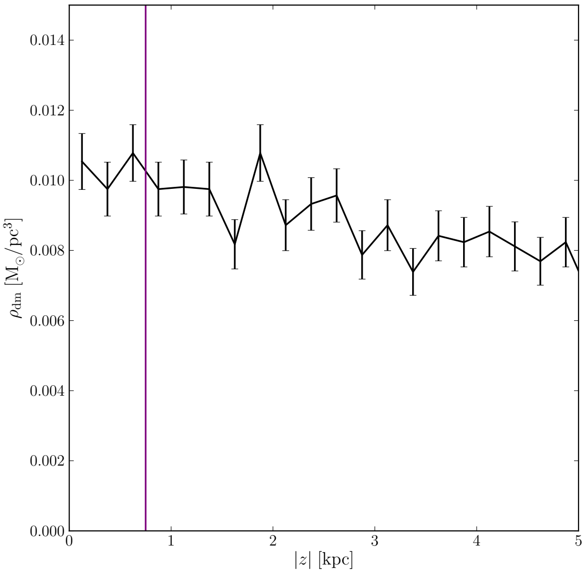

Figure 2.4: The dark matter density as a function of $|z|$ for the the unevolved (*upper panel*) and the evolved simulation (*lower panel*). The purple line represents $z = 0.75\,\mathrm{kpc}$, i.e. the maximum height considered in our analysis. The errorbars correspond to the Poisson errors. The dark matter density is noisy owing to the large mass of the dark matter particles, but it is constant within the uncertainties for $|z| < 0.75\,\mathrm{kpc}$.

The visible population in the disc for the unevolved stage ($t = 0.049\,\mathrm{Gyr}$) of the simulation is almost perfectly isothermal, while a significant deviation from isothermality is seen for the more evolved stage ($t = 4.018\,\mathrm{Gyr}$).

When the disc species are not isothermal, the second term of the Jeans equation 2.3 cannot be approximated as $\overline{v_{z,i}^2}\partial\nu_i/\partial z$, but we must consider also the contribution of z-derivative of $\overline{v_{z,i}^2}(z)$.

To quantify the effect of non-isothermality, we look at the the second and the third terms of the Jeans equation 2.3 calculated for the two stages of our simulation. We compute these terms using a Smoothed Particle Hydrodynamics (SPH)-like method to determine smoothed quantities and gradients at the particle positions (for more details see Appendix 2.6.2).

In Figure 2.6, the SPH calculated quantities are plotted for the two stages of the simulation considered $t = 0.049\,\mathrm{Gyr}$ (left panel) and $t = 4.018\,\mathrm{Gyr}$ (right panel) for $\theta = 0°$. The red line represents the potential term. The solid black and the dashed grey lines represent the sum of the two last terms of the Jeans equation in the non-isothermal (r_{NI}) and in the isothermal (r_{I}) case respectively, namely:

$$r_{\mathrm{NI}} = \nu_i \frac{\partial \Phi}{\partial z} + \frac{\partial(\overline{v_{z,i}^2}\nu_i)}{\partial z} \quad (\mathrm{non-isothermal}) \tag{2.21}$$

and

$$r_{\mathrm{I}} = \nu_i \frac{\partial \Phi}{\partial z} + \overline{v_{z,i}^2}\frac{\partial \nu_i}{\partial z} \quad (\mathrm{isothermal}). \tag{2.22}$$

We see in this figure that, for $t = 0.049\,\mathrm{Gyr}$, the second term calculated as isothermal ($\overline{v_{z,i}^2}\partial\nu_i/\partial z$, dashed cyan line) and including non-isothermality ($\partial(\nu_i\overline{v_{z,i}^2})/\partial z$ solid blue line) overlap almost perfectly, and that r_{NI} (black continuous line) and r_{I} (grey dashed line) are also very similar and close to zero. This is not surprising since the velocity dispersion $\overline{v_{z,i}^2}$ is almost constant with z in the unevolved stage of the simulation.

As expected from Figure 2.5, this is not the case for the simulation at $t = 4.018\,\mathrm{Gyr}$ where the isothermal (cyan) and the non-isothermal (blue) second term lines are clearly different. In this case r_{I} and r_{NI} are distinct and, while the non-isothermal residual averages to zero, the isothermal one presents a positive (negative) feature for $z < 0$ ($z > 0$). This suggests that using the isothermal approximation for the evolved stage of the simulation will introduce a bias that must be corrected. We show this in Section 2.3.3.1.

Finally, notice that the sum of the second and third terms of the Jeans equa-

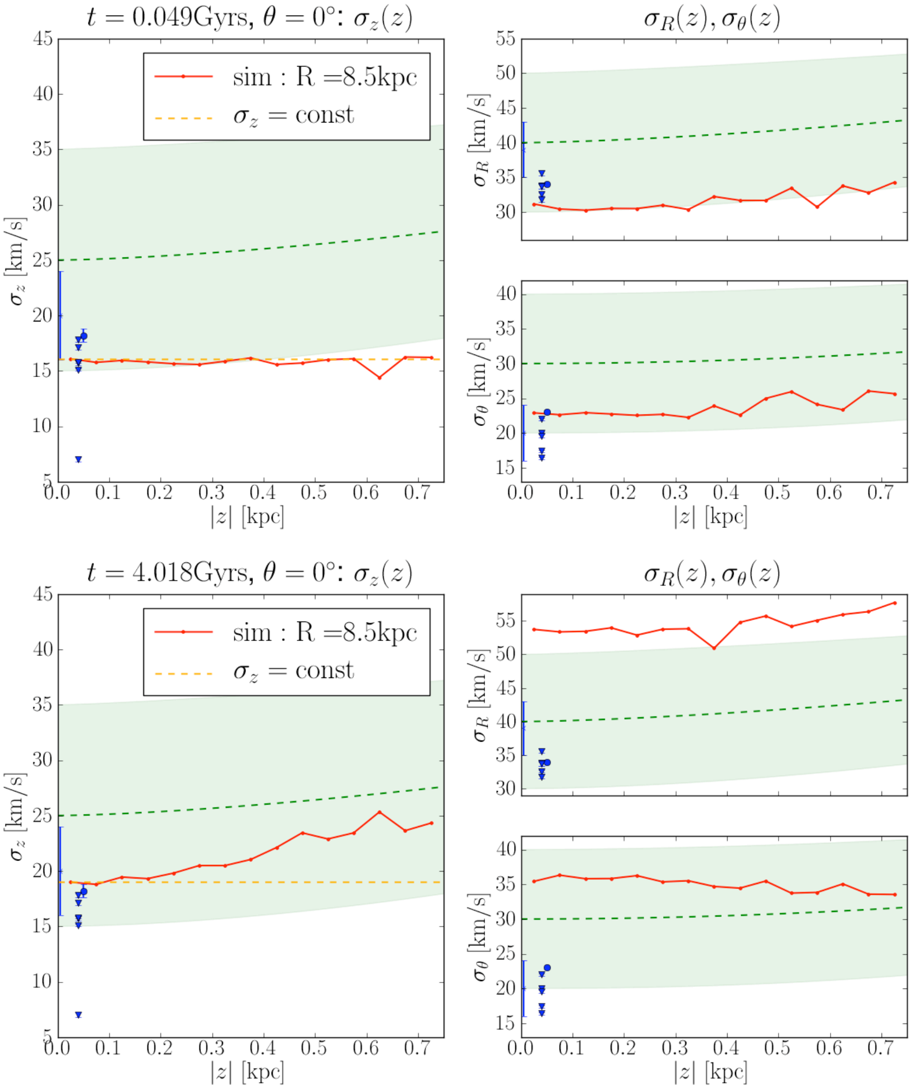

Figure 2.5: Velocity dispersion gradients with z. Upper panel: unevolved simulation $t = 0.049$ Gyr. Lower panel: evolved simulation $t = 4.018$ Gyr. The dashed green line represent the best fit of the velocity dispersion by (Bond et al., 2010), while the green shaded region shows the errors in the fitted parameters. The blue data points give the values of $\overline{v_z^2}(z)$, $\overline{v_\theta^2}(z)$ and $\overline{v_R^2}(z)$ taken from the literature (Holmberg & Flynn, 2004; Seabroke & Gilmore, 2007). The red points represent the values for our simulation at $R = 8.5$ kpc. The yellow and red dot-dashed lines in the $\overline{v_z^2}(z)$ plot are lines of constant $\overline{v_z^2}(z)$.

tion in Figure 2.6 is consistent with zero, excluding the presence of an important *tilt term* (hypothesis 3 of the MA method) or significant non-equilibrium effects (hypothesis 1).

2.3.2.3 A flat rotation curve

The second term of equation 2.12 is zero for flat rotation curves, i.e. for $V_c(R) = (Rd\Phi/dR)^{1/2}$ = constant. For a flat rotation curve the effective dark matter density corresponds to the halo mass density, $\rho_{\rm dm}^{\rm eff} = \rho_{\rm dm}(R)$, while the effect of a rising (falling) rotation curve is to give rise to a term of opposite (similar) sign to $\rho_{\rm dm}$, causing an underestimation (overestimation) of the dark matter density in the disc.

In Figure 2.7 the rotation curves for the unevolved stage of the simulation ($t = 0.049\,$Gyr) and for the evolved one ($t = 4.018\,$Gyr) are plotted in the left and the right panel respectively. For the unevolved simulation the rotation curve is almost flat or slightly falling, while for the more evolved stage, in general, the rotation curve is usually slightly rising for $R = 8.5\,$kpc; this means that we would expect a systematic underestimation of $\rho_{\rm dm}$ at $R = 8.5\,$kpc for the evolved simulation.

To quantify the effect on the determination of $\rho_{\rm dm}$, we compute $V_c(R) = (Rd\Phi/dR)^{1/2}$ in large R-bins (1 kpc) along a 'slice' of the disc for each angular position considered using the SPH-method, then we calculate its $\partial/\partial R$ derivative to estimate the second term of equation 2.12: $|(4\pi GR)^{-1}\partial V_c^2/\partial R|$. In Figure 2.8 the absolute value of these terms are plotted for $\theta = 0°$ at $t = 0.049\,$Gyr (left panel) and $t = 4.018\,$Gyr (right panel). The black crosses show the values of $\rho_{\rm dm}$ at $R = 8.5\,$kpc. For the evolved simulation, the shape of these plots is slightly different for the various angular positions at small R, due to the presence of the bar. However, at $R = 8.5\,$kpc the contribution of the rotation curve term is between 10 and 30 per cent of $\rho_{\rm dm}$ (with positive sign). The shape of the rotation curve term with R is always similar around the disc for the unevolved simulation and its contribution is $\sim 15 - 20$ per cent of $\rho_{\rm dm}$ at $R = 8.5\,$kpc, always with negative sign.

For the real Milky Way, we can estimate the contribution of the rotation curve

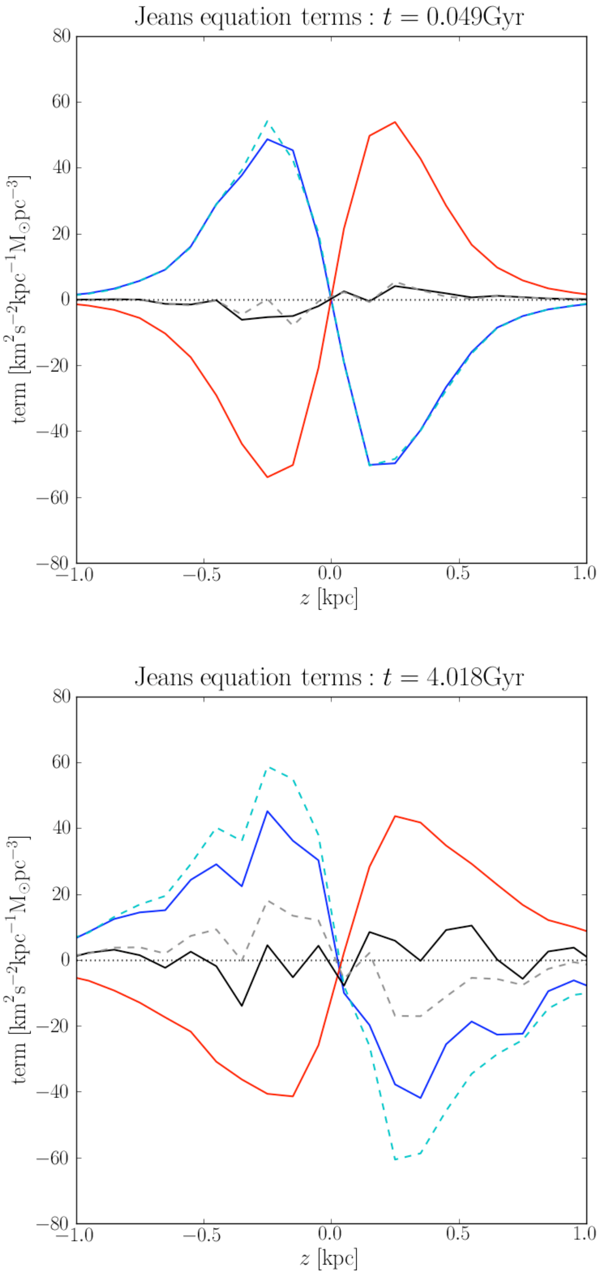

Figure 2.6: The second and the third term of the Jeans equation 2.3, calculated for our simulation at $t = 0.049$ Gyr (*upper panel*) and $t = 4.018$ Gyr (*lower panel*) for $\theta = 0°$, with the SPH-like method. The different lines represent: dashed cyan: $\overline{v_{z,i}^2}\partial\nu_i/\partial z$ (2nd term: isothermal); solid blue: $\partial(\nu_i\overline{v_{z,i}^2})/\partial z$ (2nd term: non-isothermal); solid red: $\nu_i\partial\Phi/\partial z$ (3rd term). The black and grey lines are the 'residuals' given by the sum of the terms: solid black: $\nu_i\partial\Phi/\partial z + \partial(\overline{v_{z,i}^2}\nu_i)/\partial z$ (non-isothermal); dashed grey: $\nu_i\partial\Phi/\partial z + \overline{v_{z,i}^2}\partial\nu_i/\partial z$ (isothermal).

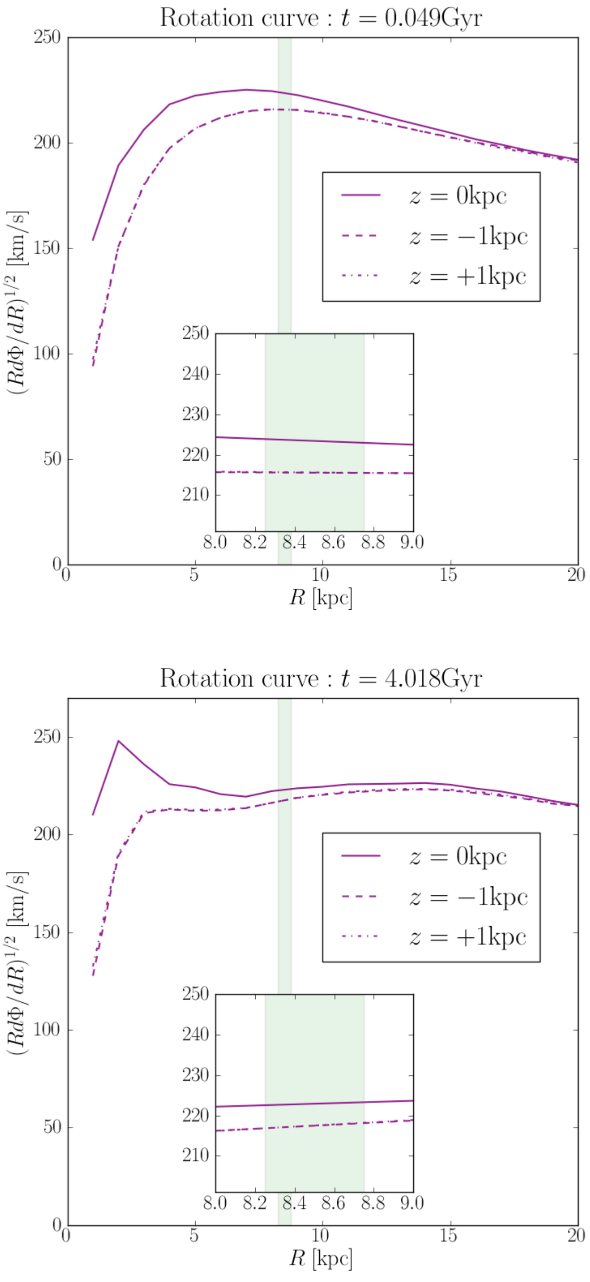

Figure 2.7: Rotation curve for the unevolved stage of the simulation (t = 0.049 Gyr - *upper panel*) and for the evolved one (t = 4.018 Gyr - *lower panel*); it was calculated in large R-bins (1 kpc) along a 'slice' of the disc for each angular position considered using the SPH-method, here the patches at $\theta = 0°$ are shown. The solid line represents V_c at the midplane, while the dashed and the dot-dashed line represent the rotation curve at $z = -1$ kpc and $z = +1$ kpc, respectively. The shaded green area is zoomed in the insert on the bottom of each plot and represents the radial position analysed in our work (R =8.5 kpc).

term from the Oort constants (Binney & Tremaine, 2008):

$$(4\pi GR)^{-1}\frac{\partial V_c^2}{\partial R} = \frac{B^2 - A^2}{2\pi G} \tag{2.23}$$

To determine the Oort constants, we must use stellar tracers that are well-mixed. As for the vertical potential determination, this means avoiding young stars. The most recent estimates using F giants (Branham, 2010) and K-M giants (Mignard, 2000) from *Hipparcos* give $A = 14.85 \pm 7.47\,\mathrm{km\,s^{-1}\,kpc^{-1}}$ and $B = -10.85 \pm 6.83\,\mathrm{km\,s^{-1}\,kpc^{-1}}$ and $A = 14.5 \pm 1.0\,\mathrm{km\,s^{-1}\,kpc^{-1}}$ and $B = -11.5 \pm 1.0\,\mathrm{km\,s^{-1}\,kpc^{-1}}$, respectively. This is ~ -35 per cent of the expected dark matter contribution as extrapolated from the rotation curve assuming spherical symmetry (see Section 2.1), namely[6] $-0.0033 \pm 0.0050\,\mathrm{M_\odot\,pc^{-3}}$, leading to a slight overestimate of the dark matter density.

2.3.2.4 Assuming that the z-motions are completely decoupled

The last assumption of the HF method is that the z motion is decoupled so that the distribution function of the stars is only a function of E_z. If this is true, the distribution function of the stars in the midplane – $f(E_z(0)) = f(w_0)$ – represents the distribution of the stars at all heights above the plane – $f(E_z(z)) = f(\sqrt{v_z^2 + 2\Phi(z)})$. Thus, it can be integrated in $w_0 = v_z(0)$ to predict the density fall-off.

In Figure 2.9, we plot the distribution function at $z = 0.5$ kpc predicted from $f(w_0, 0)$ for the unevolved simulation (first panel) and the evolved simulation (second and third panel representing two extreme cases at two different angular positions in the disc) in red. The actual distribution functions are over-plotted in black. As expected, while for the unevolved simulation the predicted distribution function is in good agreement with the actual one (left panel), the situation is different for the evolved stage. For most of the angular positions around the disc, the shape of the predicted distribution function is very different from the true one: the two volumes shown (at $\theta = 45°$ and $\theta = 180°$) in the second and third panel represent the best and the worst cases, respectively. From this analysis, we might expect the HF method to perform well on the $\theta = 45°$ patch, but poorly on the $\theta = 180°$ patch. We test this expectation in 2.3.3.

---

[6] this is just a simple average of the two cited values.

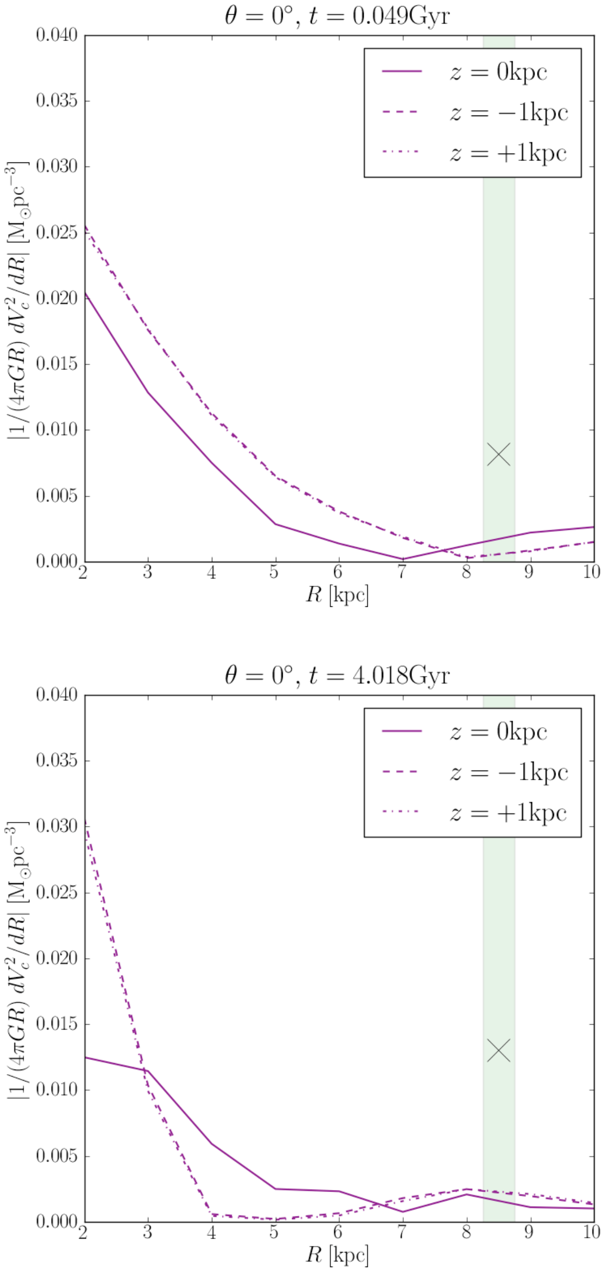

Figure 2.8: Absolute value of the rotation curve term $|1/(4\pi G) dV_c^2/dR|$ for the unevolved stage of the simulation (t = 0.049 Gyr - *upper panel*) and for the evolved one (t = 4.018 Gyr - *lower panel*). The solid line represents the term calculated at the midplane, while the dashed and the dot-dashed line correspond to $z = -1$ kpc and $z = +1$ kpc, respectively. The shaded green area represents the radial position analysed in our work (R =8.5 kpc), while the black cross gives the actual value of $\rho_{\rm dm}$ at $R = 8.5$ kpc.

Note that Statler (1989) also considered this problem. Using Stäckel potentials, he showed that, the E_z is a good approximation to the Galactic third integral close to the midplane, but not above $z \approx 1\,\mathrm{kpc}$. Two recent works by Siebert et al. (2008) and Smith et al. (2009) find that the tilt of the velocity ellipsoid for the Milky Way is indeed significant at $z \gtrsim 1\,\mathrm{kpc}$, meaning that at such height, the motion is no longer separable. In our evolved simulation, we find important non-separability even at $z \sim 500\,\mathrm{pc}$ above the plane.

We also note that assuming the separability of the distribution function as $f = f(E_z)g(L_z)$, implies that $g(L_z) = \mathrm{const.}$ with height above the midplane. We test this in Figure 2.10, where we plot $g(L_z)$ at the midplane (dashed red histogram) and at $z = 0.5\,\mathrm{kpc}$ (black histogram) for the unevolved (left panel) and for the evolved simulation (center and right panel). In the unevolved disc, $g(L_z)$ at the midplane and $z = 0.5\,\mathrm{kpc}$ are similar. For the evolved simulation this is not always the case. In accord with our analysis above, the situation is better for the 'best case' $\theta = 45°$ patch than for the 'worst case' $\theta = 180°$ patch.

2.3.3 Results for the simulation

In this section, we test the MA and HF methods on our evolved and unevolved simulations. We define three different 'Solar Neighbourhood' patches: 36 cylinders around the disc at angular separations of 10° (represented as red circles in Figure 2.3); a 'superpatch' that is the average of the 36 cylindrical patches; and 4 (or 8) wedges around the disc at angles: $\theta = 0°, 90°, 180°, 270°$ (and additionally $45°, 135°, 225°, 315°$ for the evolved simulation which is not axisymmetric, to examine all the relevant positions with respect to the bar). All patches are represented as red shaded areas in Figure 2.3. The cylinders have sampling similar to the currently available *Hipparcos* data that we consider in Section 2.4. The 'superpatch' gives sampling equivalent to that expected from the GAIA mission (GAIA will obtain distances with an accuracy better than 0.1 per cent for ~ 100000 stars within 80 pc (Bailer-Jones, 2009)). However, we can only apply the superpatch to the unevolved simulation that is axisymmetric. For this reason we introduce also the wedges that contain approximately 5 times the number of stars in a cylinder; they are the best compromise to obtain larger sampling for a sufficiently local volume in the non-axisymmetric disc. Note that, for the unevolved disc, the cylinders and wedges tell us only about sampling errors since

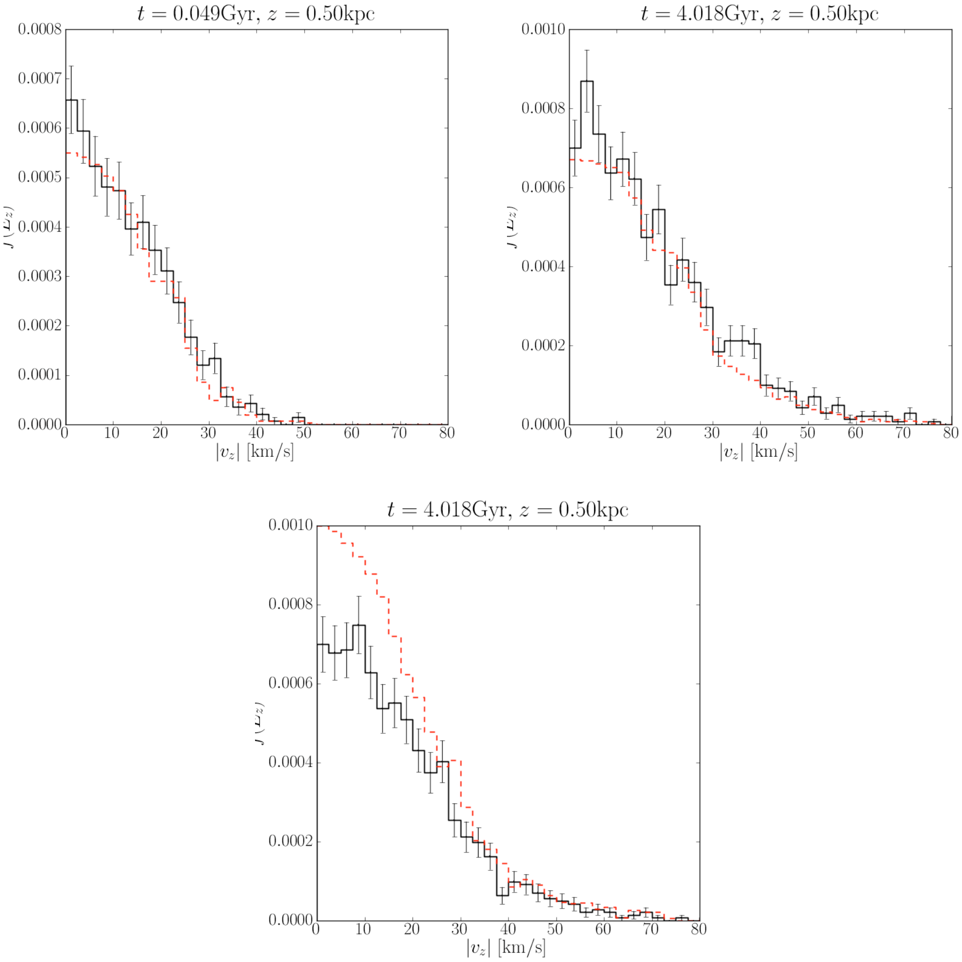

Figure 2.9: Distribution function above the plane at $z = 0.5$ kpc (in black) compared with the one predicted from $f(E_z(0))$ (in red). The first panel represents the patch at $\theta = 0°$ for the unevolved simulation ($t = 0.049$ Gyr), while the second and the third panels correspond to $\theta = 45°$ and $\theta = 180°$ in the evolved disc ($t = 4.018$ Gyr).

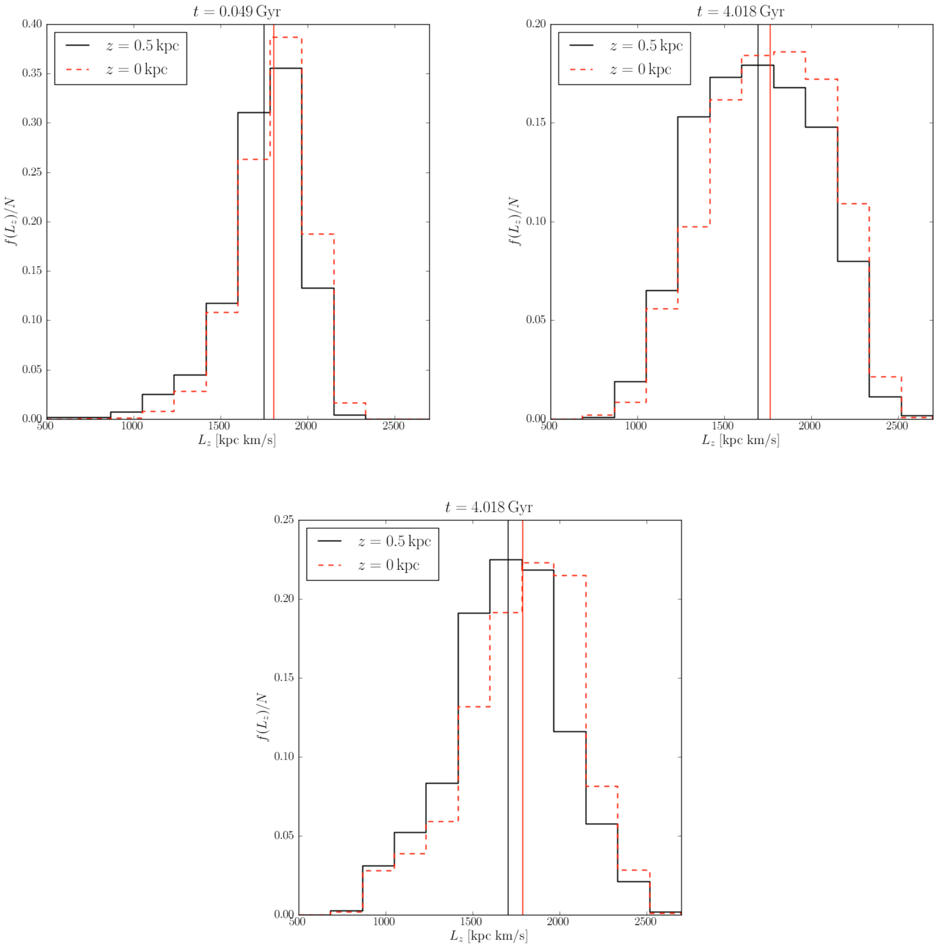

Figure 2.10: Angular momentum distribution $g(L_z)$ – normalized by the total number of stars N – at $z = 0\,\mathrm{kpc}$ (dashed red histogram) and at $z = 0.5\,\mathrm{kpc}$ (black histogram). The red and black vertical lines represent the median of the distributions at $z = 0$ and $0.5\,\mathrm{kpc}$ respectively. The left panel represents the patch at $\theta = 0°$ for the unevolved simulation ($t = 0.049\,\mathrm{Gyr}$), the centre and the right panels correspond to $\theta = 45°$ and $\theta = 180°$ in the evolved disc ($t = 4.018\,\mathrm{Gyr}$). While the distributions have similar shape, the mean shifts by ~ 3, 4 and 5 per cent for the unevolved simulation and the evolved simulation at $\theta = 45°$ and $\theta = 180°$, respectively. This means that the stars in the plane at 8.5 kpc have a mean guiding center of $\sim 8.0\,\mathrm{kpc}$, while those at $z = 0.5\,\mathrm{kpc}$ have a mean guiding center of 7.8, 7.8 and 7.7 kpc for the unevolved simulation and the evolved simulation at $\theta = 45°$ and $\theta = 180°$, respectively.

the disc is axisymmetric (the results for each patch should be statistically equivalent). For the evolved disc, however, the different patches explore the effect of spiral structure and disc inhomogeneities on our analysis.

We consider a single visible component to build the mass model for the disc, described by its density in the plane and its velocity dispersion. We set the Sun's position at $R_\odot = 8.5\,\mathrm{kpc}$. We let the local dark matter density ρ_{dm} vary in the range $[0, 1]\,\mathrm{M}_\odot\,\mathrm{pc}^{-3}$, and the disc mass density $\rho_{\mathrm{s}}(0)$ vary in the range ± 0.014 $\mathrm{M}_\odot\,\mathrm{pc}^{-3}$ around the actual value that we measure for the simulation. This range has a width comparable to the observational uncertainties for the data we consider in Section 2.4 (and see also Table 2.4).

For the HF method, we need the distribution function in the midplane $f(w_0)$ to be used in equation 2.18. To compute this, we fit the velocity distribution of stars with $|z| \leq 50\,\mathrm{pc}$ (see Section 2.3.3.1) with a Gaussian function for the unevolved simulation, and a double Gaussian for the evolved one (an example fit is shown in the left panel of Figure 2.2).

2.3.3.1 The unevovled simulation

We first consider the unevolved simulation ($t = 0.049\,\mathrm{Gyr}$) that fulfils the hypotheses of the methods.

Maximum volume of the patch We first consider the appropriate size of the volume for the MA method: it should be small enough in the radial direction (ideally infinitesimal) to average the potential and its derivatives over R to solve the Jeans equation for a one-dimensional slab. Of course, we need a large patch for the best possible sampling. In this section, we use the unevolved simulation to measure how large our patch can be before systematic errors dominate over our sample error. For this, we use the 'superpatch' described in Section 2.3.3, above. We consider the average of 36 cylinders around the disc at $R_\odot = 8.5\,\mathrm{kpc}$ with radius $R = 150, 250, 300, 400, 500\,\mathrm{pc}$.

In addition, the HF method requires measuring the distribution function in the midplane: $f(w_0)$. For this, we must choose a vertical scale to determine $f(w_0)$, and again there is a trade off between bias and sample error. To find the optimal height, we compute the velocity distribution considering star particles up to $|z| < 50, 75, 100\,\mathrm{pc}$. Note that for any patch size, there will be a bias error due to the finite volume considered. Here we find the largest patch size (for 'GAIA'

Table 2.3: Best χ^2 for different sizes of the 'local volume' box; $|z| < 50, 75, 100\,\mathrm{pc}$ is the height used to construct the midplane velocity distribution; $R = 150, 250, 300, 400, 500\,\mathrm{pc}$ is the radial size of the cylindrical box. The dashes correspond to a failure of the MCMC in recovering the density, i.e. it can not find an acceptable value.

	$R = 150\,\mathrm{pc}$	$250\,\mathrm{pc}$	$300\,\mathrm{pc}$	$400\,\mathrm{pc}$	$500\,\mathrm{pc}$
$\lvert z\rvert < 50\,\mathrm{pc}$	1.16	1.96	2.52	3.60	-
$\lvert z\rvert < 75\,\mathrm{pc}$	1.21	2.18	3.04	5.03	-
$\lvert z\rvert < 100\,\mathrm{pc}$	-	-	-	-	-

sampling; the 'superpatch' described in Section 2.3.3) for which the bias error is small as compared to the sample error. If the sampling for a given volume is improved, then we will become more sensitive to bias. In this case, the optimal patch size will be smaller than that found here.

For each choice of R and $|z|$, we apply our MCMC method to explore the ρ_s-ρ_dm parameter space and calculate the χ^2 for each model.

We first apply our MA method to test the optimal radial extent of a patch. For a cylinder of radius $R > 500\,\mathrm{pc}$ the MCMC fails to find a solution indicating that the bias errors are dominant. For smaller patches, we recover the correct values of ρ_s and ρ_dm within our quoted errors, but find that the best χ^2 shrinks with R. Next, we apply the HF method. In this case, the MCMC fails to find a solution if the midplane velocity distribution is averaged up to $|z| = 100\,\mathrm{pc}$. The best χ^2 values for each case are reported in Table 2.3 (the situation for the MA method is very similar to the first line). The recovered densities in the different volumes are shown in Figure 2.11: for $R = 250, 300, 400\,\mathrm{pc}$ and when we calculate the velocity distribution function in the midplane using stars with $|z| < 50\,\mathrm{pc}$, we always recover the correct answer even if the agreement between the predicted and the measured density fall-off of the tracers give rise to increasing χ^2 value with R. For $R = 150\,\mathrm{pc}$ the result is not as good, likely owing to the poorer sampling. Calculating the velocity distribution in the midplane from stars with $|z| < 75\,\mathrm{pc}$ gives always slightly biased results.

Given the above results, we will consistently use patches with $R = 250\,\mathrm{pc}$ and average our midplane velocity distributions for stars with $|z| < 50\,\mathrm{pc}$. This volume is similar to that used by Holmberg & Flynn (2000) whose data we consider in Section 2.4.

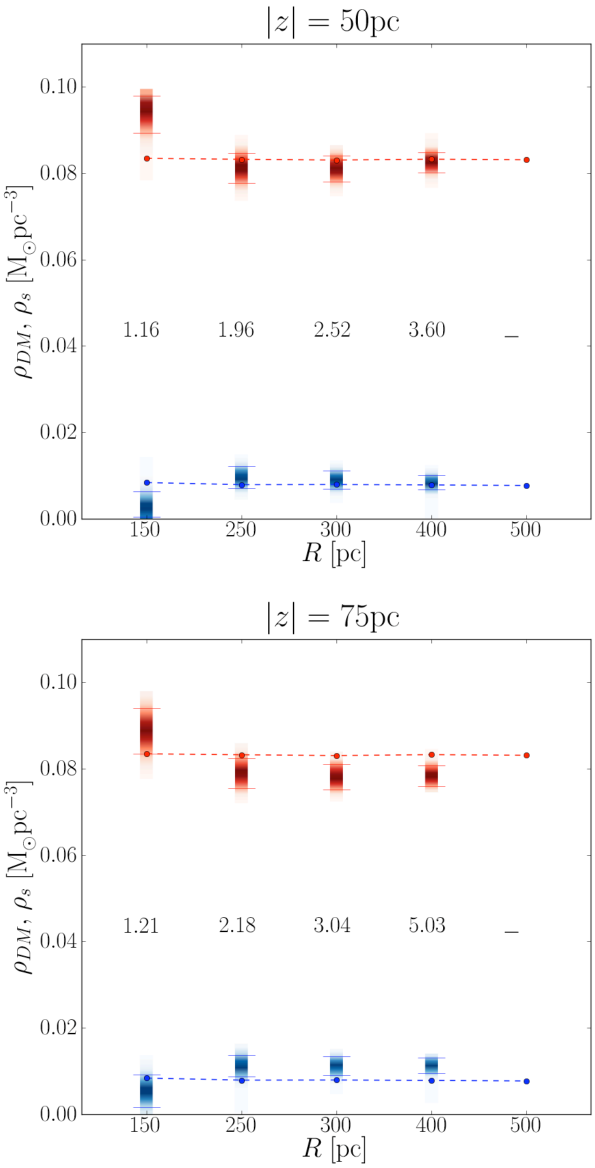

Figure 2.11: Models explored by the MCMC for the HF method, using different size of the ‘local volume’ box. The *upper* (*lower*) panel correspond to velocity distribution in the midplane constructed using stars with $|z| < 50$ pc ($|z| < 75$ pc). On the $x-$axis the different radial sizes are indicated. The blue (red) shaded rectangles represent the recovered dark (visible) matter density. The blue (red) dashed line and filled dots represent the actual value of $\rho_{\rm dm}$ ($\rho_{\rm s}$). The horizontal red (blue) segments represent the 90 per cent errors in the recovered value of $\rho_{\rm s}$ ($\rho_{\rm dm}$).

Degeneracy in $\rho_{\rm s}$ and $\rho_{\rm dm}$ In their work, Holmberg & Flynn (2000) fit the density fall off of the stellar tracers up to $0.1 - 0.2\,$kpc which approximately corresponds to the MW disc half mass scale height $z_{1/2}$. If we adopt the same criteria for our 'superpatch', we see that the area of the $\rho_{\rm s}$-$\rho_{\rm dm}$ plane explored by the MCMC corresponds to a 45^o stripe with almost the same value of χ^2 for all models. This means that we have a nearly flat distribution of models and a strong degeneracy between $\rho_{\rm s}$ and $\rho_{\rm dm}$. This is shown in the left panel of Figure 2.12. The grey contours represent the density of models explored by the MCMC, while the black contour contains all models with $\chi^2 \leq 1.1\chi^2_{\rm best}$.

This strong degeneracy means that we can only determine the total density on the plane $\rho_{\rm tot}(0) = \rho_{\rm s}(0) + \rho_{\rm dm}(0)$, but not $\rho_{\rm s}$ and $\rho_{\rm dm}$ separately. To break this degeneracy – and obtain smaller error bars – we must fit the tracers to higher z. This has been noted in earlier work. Bahcall (1984c) state that data up to $z = 600\,$pc are required to be sensitive to the SHM dark matter density.

In the right panel of Figure 2.12, we show our recovered $\rho_{\rm s}$ and $\rho_{\rm dm}$, but now fitting to $|z| = 0.75\,$kpc ($\sim$ 4 times $z_{1/2}$). This is sufficient to break the degeneracy and we recover the correct answer for both $\rho_{\rm s}$ and $\rho_{\rm dm}$ inside our 1σ error bars. We show results here for brevity only for the MA method, however the HF method produces similar results for this test. For the rest of our analysis we will fit the density fall-off of the tracers up to 0.75 kpc.

Introduction of realistic errors As already stressed, the 'superpatch' has statistics comparable to that expected for the GAIA mission. In this section, we consider the effect of realistic observational errors in the velocities and positions of the stars on the recovered stellar and dark matter densities.

We consider errors typical for current *Hipparcos* data (that we consider in Section 2.4) and GAIA quality data. The *Hipparcos* mission provided $\sim 10^4$ stars out to $\sim 100\,$pc with proper motions and parallaxes accurate to < 10 per cent (Dehnen, 2002). In Holmberg & Flynn (2000), the (incomplete) radial velocity information from *Hipparcos* data were ignored and the velocity distribution was computed using only low latitude stars, whose motion is dominated by the proper motion. The confidence limits were estimated via a series of Monte Carlo simulations of observations drawn from synthetic *Hipparcos* survey catalogues, taking into account the *Hipparcos* magnitude limits and magnitude-dependent parallax and proper-motion errors. For the A and the F sample they found a 95 per cent

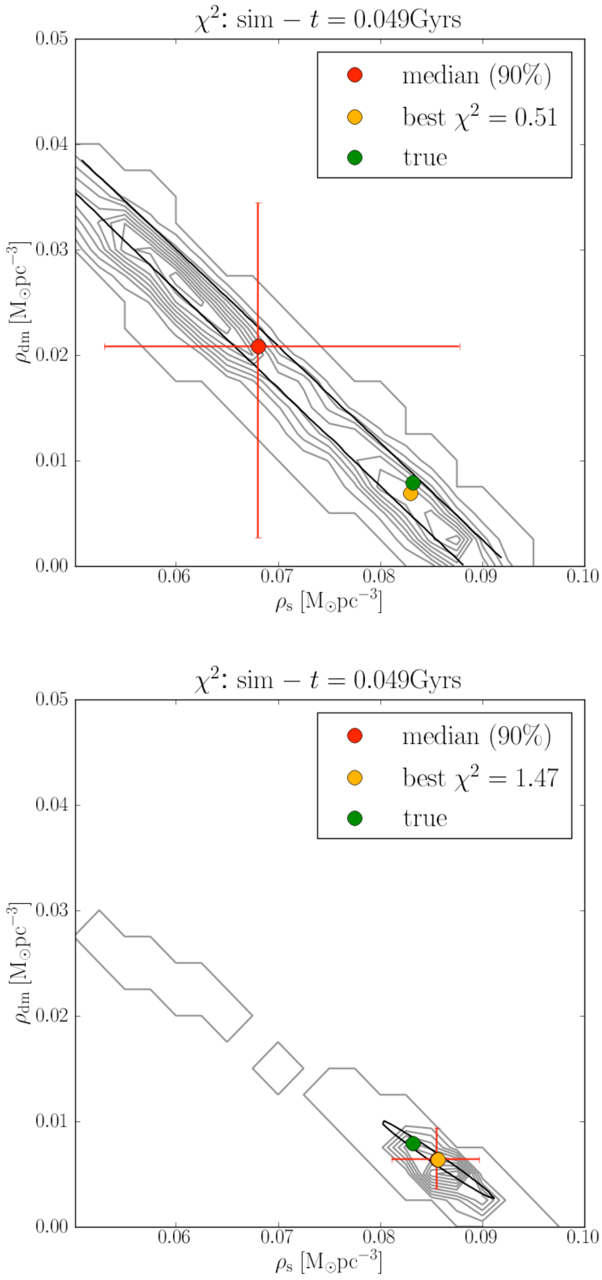

Figure 2.12: MCMC models in $\rho_{\rm s}$-$\rho_{\rm dm}$ space for the 'superpatch' applied to the unevolved simulation. The yellow dot corresponds to the best $\chi^2_{\rm best}$ model; the green dot corresponds to the true value; the red dot is the median of the distribution with 90 per cent error bars; the black contours contain all models with $\chi^2 \leq 1.1\chi^2_{\rm best}$; and the grey contours represent the density of models explored by the MCMC. *Upper panel:* fitting the density fall off up to $|z| = 0.25$ kpc ($\gtrsim z_{1/2}$); *Right panel:* fitting up to $|z| = 0.75$ kpc ($\gtrsim 4z_{1/2}$).

confidence limit of $\pm 0.011\,\mathrm{M_\odot\,pc^{-3}}$ and $\pm 0.023\,\mathrm{M_\odot\,pc^{-3}}$, respectively.

GAIA will determine distances for 150 million stars with a accuracy better than 10 per cent (within 8 kpc) and some 100000 stars to better than 0.1 per cent within 80 pc (Bailer-Jones, 2009). For an unreddened K giant at 6 kpc, GAIA will measure the distance accurate to 2 per cent and the transverse velocity with an accuracy of about $1\,\mathrm{km\,s^{-1}}$ (Bailer-Jones, 2009).

To understand the impact of GAIA's accuracy, we introduce Gaussian errors in the velocity of $1\,\mathrm{km\,s^{-1}}$ and an accuracy in the positions of 2 per cent. We then run our MCMC chain on these input data with errors. We find that our recovered values for the density are unchanged, but the χ^2 increases. We conclude that velocity-position errors are a perturbation on sample errors and model systematics.

Here we included only uncorrelated errors on distances and velocities of the stars; correlated errors could be a concern when one calculates space velocity from proper motions. However, in the methods considered, only the vertical velocity of stars in a small volume (i.e. mostly high latitude stars) for which v_z is mostly due to the radial velocity are considered. In addition, we show that the main uncertainties come from model rather than measurement uncertainties.

The importance of statistics In this section, we investigate the effect of sample size. We considered a GAIA data quality mission with 'superpatch' sampling. Now we consider smaller patches with sampling more similar to *Hipparcos* data. Good statistics are particularly important for the HF method that requires the shape of the in-plane velocity distribution function rather than just its moments.

We consider 4 cylindrical volumes around the disc with statistics comparable to *Hipparcos* data ($\sim 2000 - 3000$ within $|z| < 200\,\mathrm{pc}$), and 4 wedge-shaped larger volumes at the same angular positions, having the same radial and vertical size, but covering a larger azimuthal angle (and containing about 4-5 times more particles).

The results are reported in Figure 2.13, which shows the models explored by the MCMC for the MA method for the four cylinders (left panel) and the four wedges (right panel). In both cases, the method recovers the correct value of ρ_s and ρ_dm within our quoted errors, with the error bars shrinking with improved sampling as expected. The results are almost identical for the HF method for this early stage of the simulation.

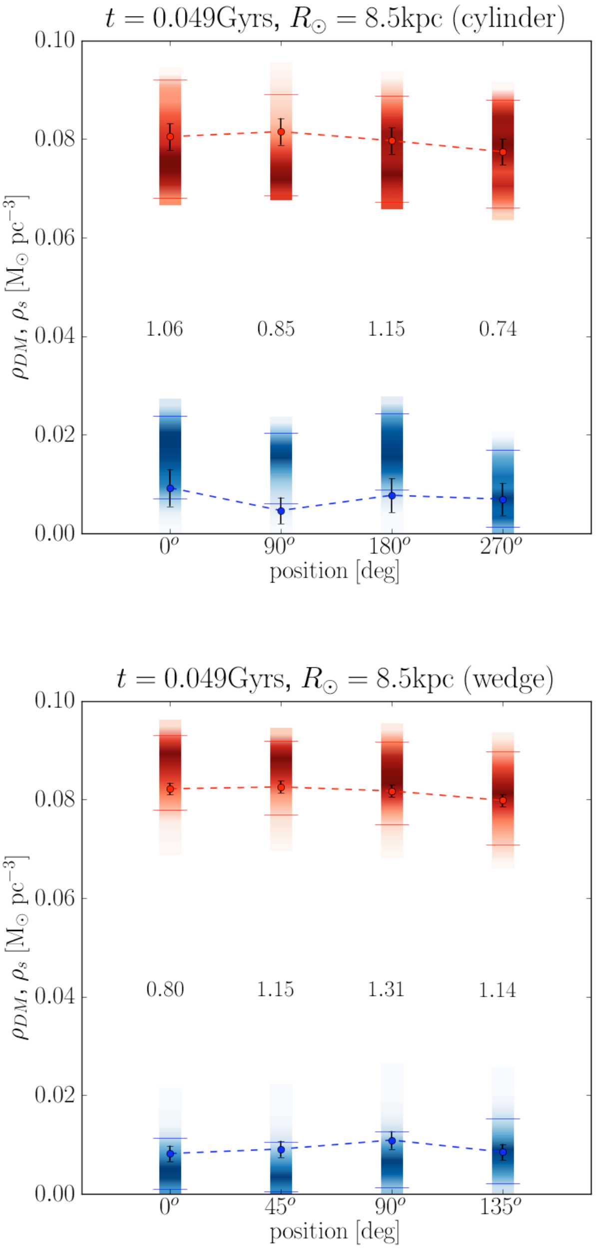

Figure 2.13: Models explored by the MCMC for the MA method for the four cylinders (*upper panel*) and the four wedges (*lower panel*) represented as shaded areas of different colours. Blue corresponds to the recovered dark matter density $\rho_{\rm dm}$ and red to the recovered visible matter density $\rho_{\rm s}$ in the plane. The filled dots represent the corresponding actual values with Poisson errors. The red and blue horizontal segments show the 90 per cent errors on the recovered densities. The numbers correspond to the reduced χ^2 values. Notice that the apparent fluctuations in the density at different angular positions are due to the sample noise.

2.3.3.2 The evolved simulation

The HF method In the previous section, we demonstrated that the MA and HF methods perform equivalently well when applied to the ideal situation of an isothermal axisymmetric disc, fulfilling all the standard assumptions. Both recover the local dark matter and midplane stellar densities within our quoted uncertainties. The situation is different when we consider the evolved stage of the simulation. The onset of spiral arms and a bar causes significant radial mixing that induces vertical non-isotropy and non-separability that violate key assumptions in the HF method. As such, we might expect its performance to degrade accordingly.

We consider 8 different wedges[7] around the evolved disc to sample patches that lie on/away from spiral/bar features. We first apply the HF method, assuming an isothermal disc mass model. The results are shown in Figure 2.14 (upper panel). As expected, we do not recover the correct value of the local stellar and dark matter densities for most of the volumes. The possible reasons are: the neglected non-isothermality of the disc; the unsatisfactory fit of the distribution function with a double Gaussian (at least for some of the volumes considered); and, at this stage of the simulation, that the distribution function of the stars above the plane is not well represented by the distribution in the midplane.

To test the first two possible sources of error, we correct for the non-isothermality of the disc population using equation 2.9 instead of 2.15, and we interpolate linearly the distribution function instead of fitting it. The results are very similar; the reason for such a small change is that it is the non-isothermality of the *tracers* that really matters, not that of the whole disc model. (Recall that the HF method does not assume that the tracers are isothermal, but rather that their distribution function is a function only of the vertical energy E_z). Thus we can conclude that it is the assumption that $f = f(E_z)$ that leads to the systematic bias in the recovery of $\rho_{\rm dm}$ and $\rho_{\rm s}$ for the HF method applied to the evolved simulation. To see this, consider the wedges at $\theta = 45°$ and $\theta = 180°$. Recall from Section 2.3.2 that for the former wedge, the velocity distribution at $z = 0.5\,$kpc was well predicted from $f(w_0)$, while for the latter wedge the velocity distributions differed strongly. As might be expected, the $\theta = 45°$ gives an excellent recovery for $\rho_{\rm dm}$

---

[7] In order not to confuse sampling errors with systematic errors, we show the results for the evolved simulation only for the wedges. The results for the MA method applied to the cylinders are given in Appendix 2.6.3.

and $\rho_{\rm s}$, while the $\theta = 180°$ wedge gives a very poor recovery. In the lower panel of Figure 2.14 the recovered total (visible+dark) matter density is shown: the HF method fails to recover the correct answer in many cases, even dramatically (e.g. see $\theta = 90°$ or $\theta = 315°$).

The above is a problem for the HF method – and indeed any method that assumes that $f = f(E_z)$ – if such methods are applied at heights larger than ~ 1 disc scale height. However, going to this height is necessary to break the degeneracy between $\rho_{\rm dm}$ and $\rho_{\rm s}$ (Section 2.3.3.1). It may be possible to build an unbiased distribution function (or mixed) method that works at large height above the disc plane, by using more complex forms for f. This is beyond the scope of this present work.

The MA method We first apply the MA method assuming isothermality of the tracers to the 8 wedges. The results are shown in Figure 2.15. Notice that, similar to the HF method, the density recovery in all of the wedges is systematically biased and poor. The MCMC explores a very small area in the $\rho_{\rm s}$-$\rho_{\rm dm}$ parameter space, always pushing on the lower limit imposed for $\rho_{\rm dm}$. The error in this case has a particular direction: this probably owes to the deviation from zero of the sum of the second and third terms of the Jeans equation (represented as a grey line in Figure 2.6). When we assume isothermality, this has a particular sign.

Next, we include the non-isothermality of our tracers. The results are shown in Figure 2.16. Our results are now excellent for all patches, recovering the correct unbiased value for both $\rho_{\rm dm}$ and $\rho_{\rm s}$ (and the total matter density) within our quoted 90 per cent uncertainties. This emphasises the importance of knowing $\overline{v_{z,i}^2}(z)$ precisely for each tracer population. In fact, a small deviation from the actual velocity dispersion of the tracers is enough to lead to a wrong result; for this reason we linearly interpolate $\overline{v_{z,i}^2}(z)$. Note that this is possible for the simulation if we consider large enough wedges, so that the velocity dispersion is a quite smooth. For real data the situation is more complicated since we have to deal with velocity uncertainties and noisier velocity dispersions. In this case, we can use the MCMC to marginalise over such uncertainties. We demonstrate this for the evolved simulation in Appendix 2.6.3.

Note, however, that the errors are still large even though the relative amount of dark matter in the simulation is larger than we expect in the Milky Way. We can further improve on this if the errors on $\rho_{\rm s}(0)$ can be reduced. We ex-

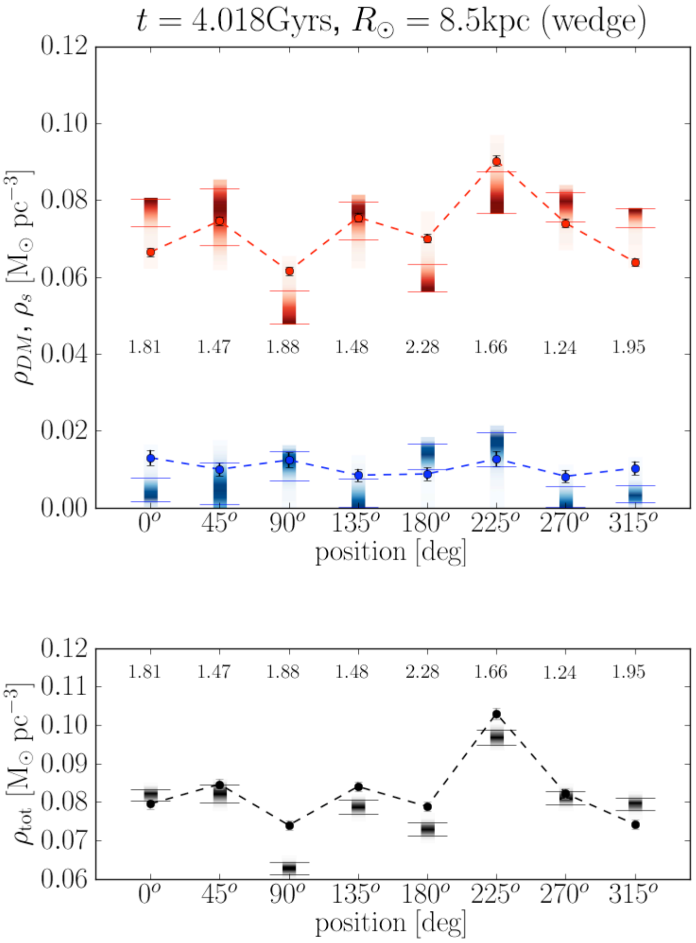

Figure 2.14: Models explored by the MCMC for the HF method assuming isothermality of the disc population and using a double Gaussian fit of the velocity distribution for the 8 wedge-shaped “Solar neighbourhood” volumes at $R = 8.5$ kpc. Upper panel: recovered dark and visible matter density (the symbols and colours are as in Figure 2.13). Lower panel: recovered total (dark+visible) matter density. The numbers under each stellar density are the reduced χ^2 for the best-fitting model.

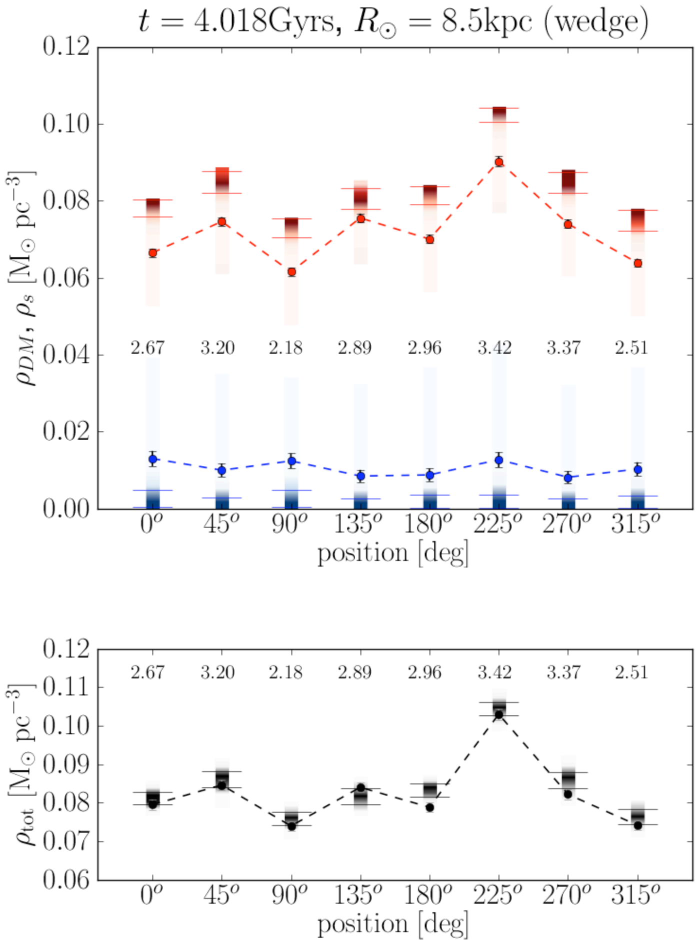

Figure 2.15: Models explored by the MCMC for the MA method assuming isothermality for 8 wedge-shaped "Solar neighbourhood" volumes at $R = 8.5$ kpc. The symbols and colours are as in Figure 2.14. The numbers under each stellar density are the reduced χ^2 for the best-fitting model.

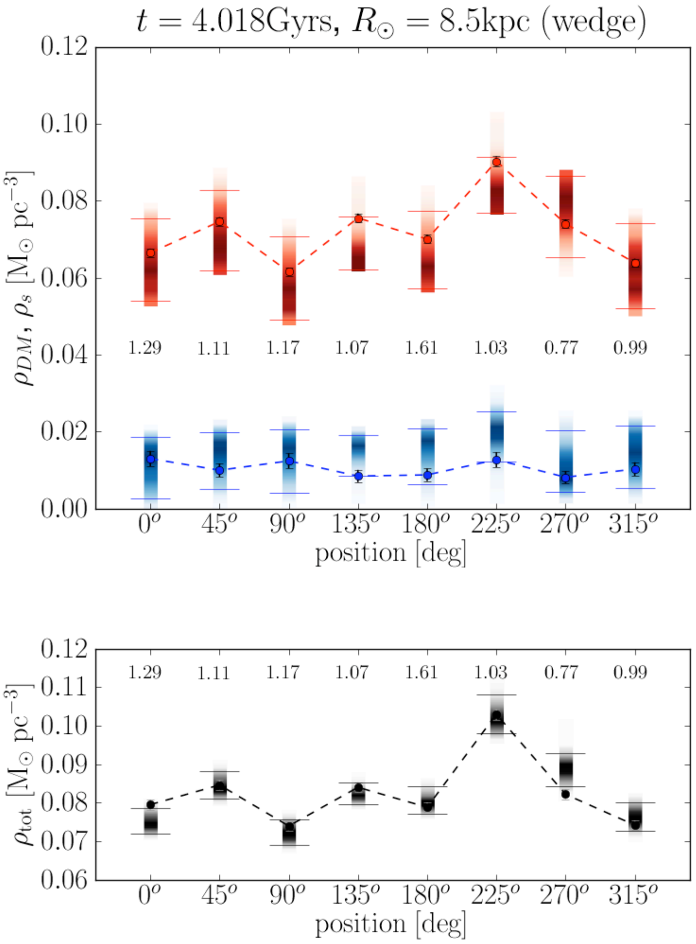

Figure 2.16: Models explored by the MCMC for the MA method for 8 wedge-shaped "Solar neighbourhood" volumes of the evolved simulation at $R = 8.5\,$kpc. Upper panel: recovered values of dark and visible matter density. Lower panel: recovered values of the total (dark+visible) matter density. The symbols and colours are as in Figure 2.15.

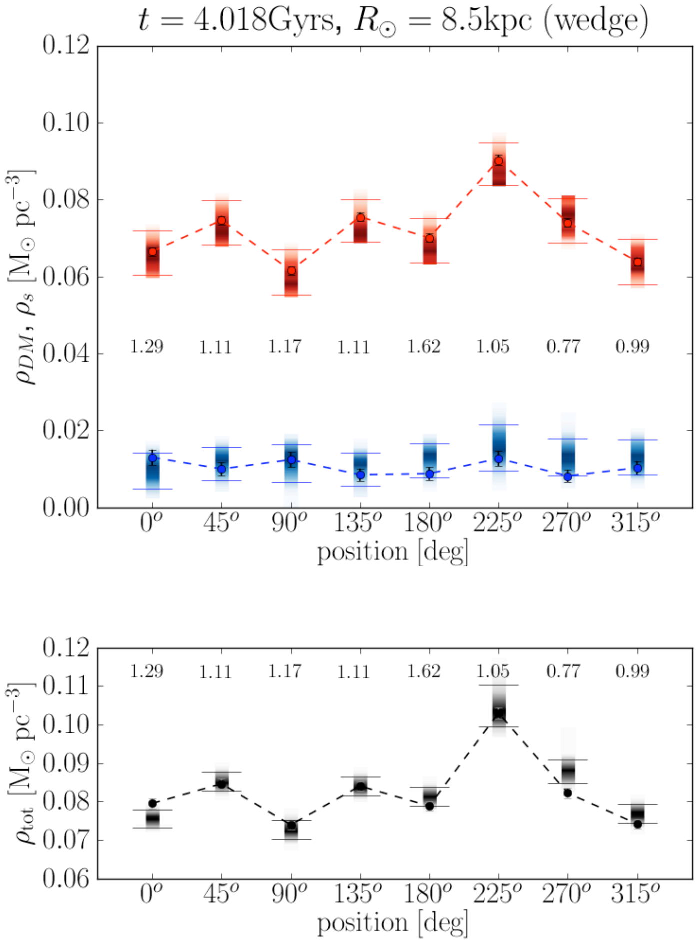

Figure 2.17: Models explored by the MCMC for the MA method for 8 wedge-shaped “Solar neighbourhood” volumes of the evolved simulation at $R = 8.5\,$kpc. In this case tighter constraints on $\rho_{\rm s}$ are assumed (an error of $\pm 0.007\,{\rm M}_\odot\,{\rm pc}^{-3}$ instead of $\pm 0.014\,{\rm M}_\odot\,{\rm pc}^{-3}$). The symbols and colours are as in Figure 2.15.

plore this in Figure 2.17 where we assume that $\rho_{\rm s}(0)$ is known to an accuracy of $\pm 0.007\,{\rm M}_\odot\,{\rm pc}^{-3}$ instead of $\pm 0.014\,{\rm M}_\odot\,{\rm pc}^{-3}$ as previously assumed. The results are correspondingly improved, as expected. This suggests that the key limiting factors to determining $\rho_{\rm dm}$ are a good measure of the non-isothermality of the tracer population, and an accurate determination of the local visible matter density.

2.4 Application to real data

In this section, we illustrate the power of our new minimal assumption (MA) method by applying it to the *Hipparcos* data used by Holmberg & Flynn (2004) to calculate the local surface density up to $z = 0.7\,\mathrm{kpc}$. As we demonstrated in Section 2.3.3.1, fitting the density fall-off up to large z is required to break the degeneracy between ρ_s and ρ_dm.

2.4.1 The data

We use the raw data of the 'HD sample' Holmberg & Flynn (2004) from Chris Flynn (private communication) consisting of 139 K-giants from Flynn & Freeman (1993)'s catalogue in a cone pointing towards the South Galactic Pole with an aperture of $430\mathrm{deg}^2$, having a limiting visual magnitude of $V = 9.2$, a magnitude range of $0.0 < M_V < 2.0$ and a colour range of $1.0 < B - V < 1.5$ (see figure 11, upper panel in Holmberg & Flynn (2004)). Holmberg & Flynn (2004) compute the velocity distribution of the tracers using a volume complete (to 100 pc) sample of 395 K-stars from the *Hipparcos* catalogue with radial velocity information (in the same colour and absolute magnitude ranges). Because of the nature of those data, the analysis is more complicated and uses the *Hipparcos* luminosity function for K-giants (figure 2 in Holmberg & Flynn (2004)). A further complication as compared to our simulation data is the mass model for the real Milky Way which has several gas and stellar components, each with its local density and velocity dispersion. The density in the midplane $\nu_{i,0}$ and the velocity dispersion $\overline{v_{z,i}^2}(0)$ of the various visible components Flynn et al. (2006) are listed in Table 2.4.

The HD sample contains very few stars, so we also include additional constraints from the literature. This illustrates the power of our MA technique coupled to the MCMC since additional constraints are straightforward to add. As additional data, we include the two volume complete samples of stars from *Hipparcos* data employed by Holmberg & Flynn (2000) in their calculation of the local density: the *A* star sample (including B5 to A5 stars) which contains 2026 stars in a cylinder with radius and height of 200 pc, and the *F* sample (A0 to F5) which comprises 3080 stars within 100 pc. We also ensure that the surface density calculated for each model explored by the MCMC agrees with the observational constraints. In the second column of Table 2.4, the current observational constraints for the surface densities of the different visible components are listed.

From the values in this table, we adopt a total visible surface density for the disc of $\Sigma_{vis}(\mathrm{R}_\odot)$=49.4$\pm$4.6 $\mathrm{M}_\odot$ pc^{-2}. For each model explored by the MCMC we then calculate the expected surface density as:

$$\Sigma_{\mathrm{s}}^{\mathrm{exp}} = 2\int_0^\infty \rho_{\mathrm{s}}(z)dz = 2\int_0^\infty \sum_i \nu_{i,0}\exp\left(-\frac{\Phi(z)}{\overline{v_{z,i}^2}}\right)dz, \tag{2.24}$$

where $\Phi(z)$ is the potential computed according to the parameters of the model. We then compare this with $\Sigma_{vis}(\mathrm{R}_\odot)$, including the result in our determination of the χ^2 for each model.

As parameters to fit in the MCMC, we use the local dark matter density ρ_{dm}; the total visible density in the midplane $\rho_{\mathrm{s}}(0)$; the relative fractions of the visible components $\nu_{i,0}/\rho_{\mathrm{s}}(0)$; their velocity dispersions in the midplane $\overline{v_{z,i}^2}(0)^{1/2}$; the velocity dispersion as a function of z of the tracers; and the normalisation of the density fall-off of the tracers. We allow the densities and the velocity dispersions of the different components to vary within their measured uncertainties (the errors for each component are given in Table 2.4). We let the total visible density in the plane $\rho_{\mathrm{s}}(0)$ vary within its observed range: $\rho_{\mathrm{s}}(0) = 0.0914 \pm 0.0140\,\mathrm{M}_\odot\,\mathrm{pc}^{-3}$; and we let the dark matter density vary between 0 and $0.5\,\mathrm{M}_\odot\,\mathrm{pc}^{-3}$. The velocity dispersion of the tracers in the midplane is given by the Gaussian fit of the velocity distribution calculated by Holmberg & Flynn (2004), namely $\overline{v_{z,i}^2}(0)^{1/2} = 18.3 \pm 0.6\,\mathrm{km\,s^{-1}}$ for the HD sample, and by Holmberg & Flynn (2000), i.e. $\overline{v_{z,i}^2}(0)^{1/2} = 5.7 \pm 0.2\,\mathrm{km\,s^{-1}}$ for the A sample and $\overline{v_{z,i}^2}(0)^{1/2} = 8.3 \pm 0.3\,\mathrm{km\,s^{-1}}$ for the F sample.

After computing the expected density fall-off for the tracers of the (magnitude limited) HD sample through (2.8), we apply the *Hipparcos* luminosity function and the magnitude cut $V < 9.2$, to compare it to the observed number of stars in the cone. The A and the F samples from (Holmberg & Flynn, 2000) are easier to fit, since they are volume complete.

Unfortunately, we do not have much information about the velocity dispersion above the plane of the different disc components included in the mass model. As such, we consider two extreme assumptions: one in which all of the visible components of the disc and the tracers are isothermal; and another in which the tracers and all of the visible components of the disc are non-isothermal. We model the non-isothermality of the stars in this second case assuming a behaviour similar to the fit by Bond et al. (2010) to blue disc stars. We proceed in the following

Table 2.4: The disc mass model taken from Flynn et al. 2006. Each component in the table gives the local mass density in the midplane $\rho(0)$ in $\mathrm{M_\odot pc^{-3}}$, the total column density Σ in $\mathrm{M_\odot pc^{-2}}$, and the vertical velocity dispersion $\overline{v_{z,i}^2}(0)^{1/2}$ in $\mathrm{km\,s^{-1}}$. Uncertainties on the densities are of order 50 per cent for all the gas components (indicated with *) and $10-20$ per cent for all the stellar components. For the thick disc, the column density is rather well known, while the velocity dispersion and the volume density are poorly known such that they should have larger error bars. However, these two quantities are essentially nuisance parameters for our analysis here. Since they anti-correlate and – as pointed out by Kuijken & Gilmore (1989b) – the local gravitational potential is mainly constrained by the column density, we simply assume small errors for both here such that the integrated column agrees with the observed value.

Component	$\nu_{i,0}(0)$ [$\mathrm{M_\odot\,pc^{-3}}$]	Σ_i [$\mathrm{M_\odot pc^{-2}}$]	$\overline{v_{z,i}^2}(0)^{1/2}$ [$\mathrm{km\,s^{-1}}$]
H_2^*	0.021	3.0	4.0 ± 1.0
HI(1)*	0.016	4.1	7.0 ± 1.0
HI(2)*	0.012	4.1	9.0 ± 1.0
Warm gas*	0.0009	2.0	40.0 ± 1.0
Giants	0.0006	0.4	20.0 ± 2.0
$M_V < 2.5$	0.0031	0.9	7.5 ± 2.0
$2.5 < M_V < 3.0$	0.0015	0.6	10.5 ± 2.0
$3.0 < M_V < 4.0$	0.0020	1.1	14.0 ± 2.0
$4.0 < M_V < 5.0$	0.0022	1.7	18.0 ± 2.0
$5.0 < M_V < 8.0$	0.007	5.7	18.5 ± 2.0
$M_V > 8.0$	0.0135	10.9	18.5 ± 2.0
White dwarfs	0.006	5.4	20.0 ± 5.0
Brown dwarfs	0.002	1.8	20.0 ± 5.0
Thick disc	0.0035	7.0	37.0 ± 5.0
Stellar halo	0.0001	0.6	100.0 ± 10.0

way:

1. We use the velocity dispersion in the plane of each component $\overline{v_{z,i}^2}(0)^{1/2}$ with its error bar (see Table 2.4) and the constants $A = 4 \pm 0.8$ and $b = 1.5 \pm 0.2$ calculated by Bond to compute the velocity dispersion for that particular species at the maximum fitted height $z_{\rm max}$ with the help of Bond's fitting function:
$$\overline{v_{z,i}^2}(z_{\rm max})^{1/2} = \overline{v_{z,i}^2}(0)^{1/2} + A|z_{\rm max}/{\rm kpc}|^b. \tag{2.25}$$

2. Since the function fitted by Bond is discontinuous in $z = 0$, we use a quadratic function:
$$\overline{v_{z,i}^2}(z) = \overline{v_{z,i}^2}(0)(1 + C|z|^2), \tag{2.26}$$
We choose the parameter C of equation (2.26) so that the quadratic pass through $\overline{v_{z,i}^2}(0)$ and the value of $\overline{v_z^2}(z_{\rm max})$.

In Figure 2.18, the quadratic curve (red solid line) and the Bond-like fit (red dotted line) for the HD tracers are shown. The shaded red area represent the uncertainties on the Bond's fit due to the errors in A and b calculated by Bond et al. (2010) and the uncertainties in $\overline{v_{z,i}^2}(0)^{1/2}$ (blue point). Notice that the quadratic function obtained is very close to the Bond's fit and lies inside its quoted uncertainties.

We stress that the velocity dispersion law from Bond et al. (2010) refers to different types of stars that are hotter than the A, F and K stars we consider here. However, recall that our goal is simply to explore the effect of varying the functional form of $\overline{v_{z,i}^2}$.

To summarise, our approach is as follows: (i) we use the mass model of table 2.4 (with a constant dark matter contribution) to calculate the potential; (ii) we use this potential and an isothermal/Bond-like velocity dispersion law (separately normalised for each tracer population) to predict the density fall-off of the three tracer populations; (iii) we simultaneously predict the total visible surface density; (iv) from the comparison of the three predicted and observed density laws (and the predicted and observed visible surface density) we accept or discard the initial guess for the potential at each iteration of the MCMC.

The application of the MA method assuming isothermal or Bond-like velocity dispersion profiles leads to very different results for the recovered visible and dark

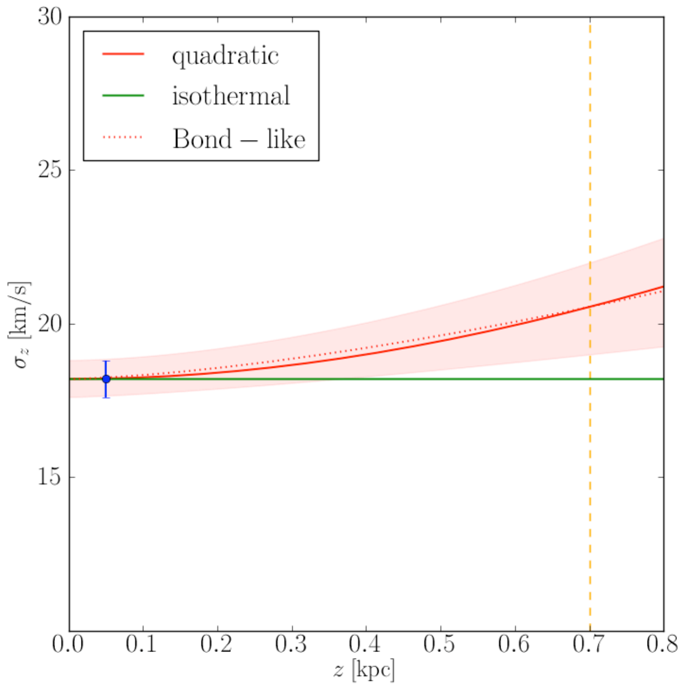

Figure 2.18: Bond-like (dotted red line), quadratic (red solid line) and isothermal (solid green line) velocity dispersion functions for the 'HD sample'. The shaded red area represents the errors in the Bond-like function. The blue dot represents the measured velocity dispersion in the local sample ($|z| < 100\,\mathrm{pc}$) and the dashed orange line is at $z = 0.7\,\mathrm{kpc}$ (the upper z-limit for the HD sample).

matter density, but with a very similar value of χ^2. The results are given in Figure 2.19. The recovered visible and dark matter density calculated with the MA method assuming isothermality (upper panel) and a Bond-like non-isothermality (lower panel) are shown. The red dot represents the median of the distribution of the models explored by the MCMC in the $\rho_{\rm s}$-$\rho_{\rm dm}$ plane within a 90 per cent confidence interval. The blue dashed lines correspond to the priors imposed on $\rho_{\rm s}$; the purple stripe shows the result by Holmberg & Flynn (2000); and the green and yellow horizontal dashed lines represent the lower limit of the local dark matter density ($\simeq 0.005\,{\rm M}_\odot\,{\rm pc}^{-3}$) as extrapolated from the Milky Way's rotation curve (a summary of these values is given in Table 2.5) and the 'Standard Halo Model' (SHM) canonical value ($\simeq 0.008\,{\rm M}_\odot\,{\rm pc}^{-3}$), respectively.

If all of the stellar tracers are assumed to be isothermal, we obtain a fit similar to Holmberg & Flynn (2000) with a dark matter density of $0.006^{+0.008}_{-0.005}\,{\rm M}_\odot\,{\rm pc}^{-3}$. By contrast, if we assume instead a 'Bond-like' non-isothermality for the stellar populations in the disc, the recovered dark matter density is much larger ($0.036^{+0.007}_{-0.008}\,{\rm M}_\odot\,{\rm pc}^{-3}$); the measured local dark matter densities, corrected for the rotation curve using the Oort constants (see section 2.3.2.3), are: $0.003^{+0.009}_{-0.007}\,{\rm M}_\odot\,{\rm pc}^{-3}$ (for the isothermal tracers) and $0.033^{+0.008}_{-0.009}\,{\rm M}_\odot\,{\rm pc}^{-3}$ (for non-isothermal tracers). They are represented as black dots in Figure 2.19.

Yet the (non-reduced) χ^2 for both models is comparable: $\chi^2 = 41.5$ for the fully isothermal model and $\chi^2 = 42.3$ for the non-isothermal model. This means that, for the data we consider here, we cannot discriminate between these two scenarios. Note that our χ^2 values seem rather high (similar to those for the model fits in Holmberg & Flynn (2000)). The number of fitted parameters is 38, using 39 data points and two additional constraints (the total visible density and the surface density). This latter constraint is non-linear and so we cannot simply compute a reduced χ^2. However, assuming that this constraint enters linearly, this gives a remaining 3 degrees of freedom and a reduced χ^2 of 13.8 for the isothermal model and 14.1 for the non-isothermal model. This is still high, suggesting that our models are a poor representation of the data, despite the apparent goodness of the fits (shown in Figure 2.20). The reason for this is that our method leads by construction to a smooth density fall-off which cannot account for the (statistically significant) wiggles present in the analysed samples.

Finally, we repeated our analysis using the isothermal mass model of Table 2.4, but still assuming a Bond-like non-isothermal velocity dispersion for the tracers.

Table 2.5: Extrapolated values of the local dark matter density using other methods from the literature. From these, we can place a reasonable lower limit on $\rho_{\rm dm}$ of $0.005\,{\rm M}_\odot\,{\rm pc}^{-3}$ ($\sim 0.20\,{\rm GeV\,cm}^{-3}$).

$\rho_{\rm dm}(R_\odot)$ $[\,{\rm GeV\,cm}^{-3}]$	Method	Reference
$0.519^{+0.021}_{-0.017}$	microlensing+ mass modeling	Gates et al. (1995)
0.385 ± 0.027	Bayesan approach + Einasto profile	Catena & Ullio (2010)
0.364	rotation curve + spherical halo	Sofue et al. (2009)
$0.20 \div 0.52^{a}$	rotation curve + mass modeling^{b}	Weber & de Boer (2010)

^{a} range for the different mass models considered.

^{b} this is a lower limit calculated considering smooth DM halo; substructures can only enhance the local density.

We found that the result was almost unchanged. This means that the method is very sensitive to the velocity dispersion of the tracer population that must be known accurately. However, the visible components of the mass model are less important. This is not surprising: the velocity dispersion of the tracers enters in equation 2.8 and thus directly affects the tracer density fall-off. By contrast, the mass-model velocity dispersion profiles appear only in equation 2.11 (through equation 2.9), and uncertainties in these profiles are marginalised out when we calculate $\rho_{\rm dm}$ and $\rho_{\rm s}$. Thus, it is vital to obtain an accurate determination of $\overline{v_{z,i}^2}(z)$ for our tracers, but not crucial to know the precise form of the mass model.

2.5 Conclusions

We have revisited systematic problems in determining the local matter densities from stellar motions. We used a high resolution N-body simulation of a Milky Way like Galaxy to test different methods in the literature and the systematic errors potentially introduced by their assumptions. We introduced a new method – the minimal assumption (MA) method – based on moments of the Jeans equations, combined with a Monte Carlo Markov Chain technique to marginalise over the

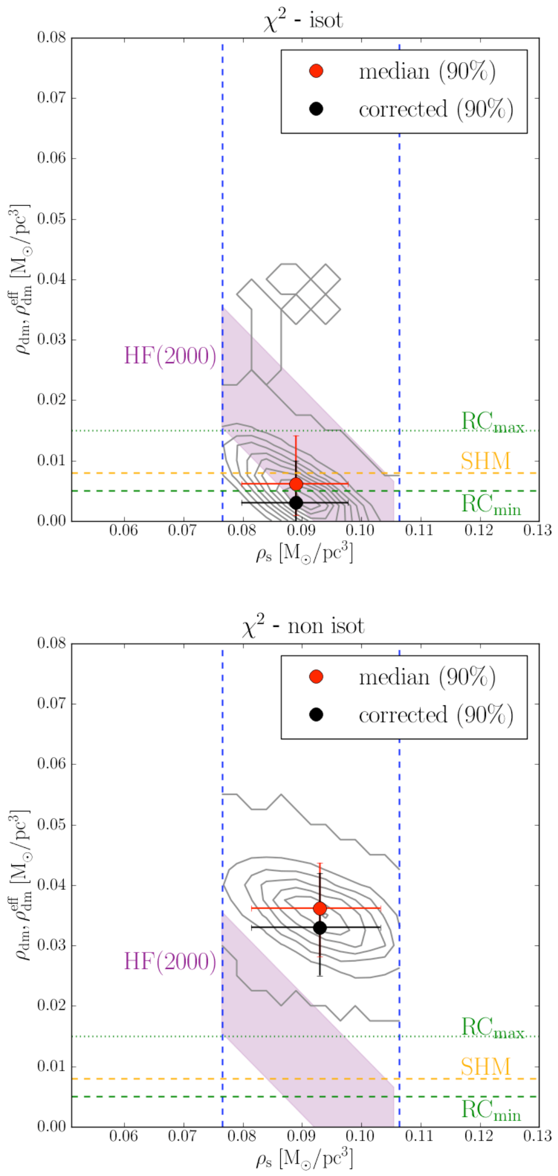

Figure 2.19: The recovered visible and dark matter density calculated with the MA method, assuming isothermality (*upper panel*) and non-isothermality of all the stellar populations (*lower panel*) for the real data. The grey contours represent the density of models explored by the MCMC, the red dot represents the median values of ρ_{s} and $\rho_{\mathrm{dm}}^{\mathrm{eff}}$ (see equation 2.12); the red error bars correspond to the 90 per cent confidence interval of the distribution. The black dot is the result corrected for the rotation curve term calculated from the Oort contants (see Section 2.3.2.3). The purple area represents the values estimated by Holmberg and Flynn (2000). The blue dashed lines show the imposed priors on ρ_{s} and ρ_{dm}. The green and the yellow lines represent the minimum value and the maximum value of ρ_{dm} measured using rotation curves in the literature and the SHM value, respectively.

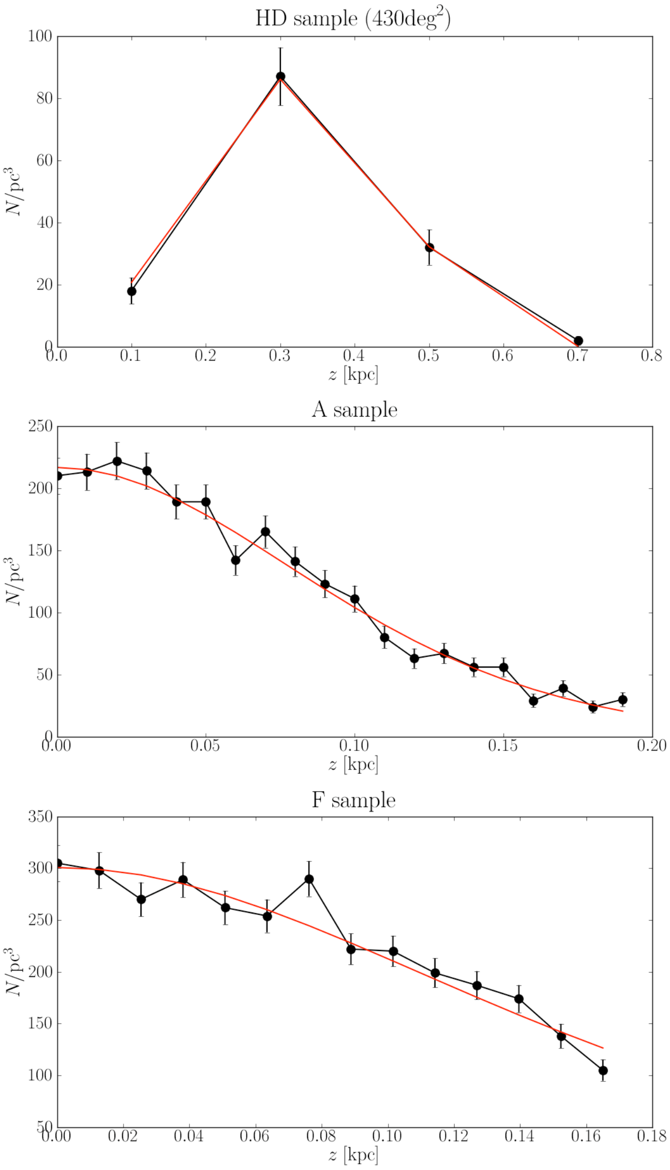

Figure 2.20: The recovered density fall-off for the three tracers considered, assuming isothermality of all the disc populations: the HD sample from Holmberg & Flynn (2004) (first panel); and the A and F star samples from Holmberg & Flynn (2000) (second and third panels). Similarly good fits were obtained for the maximally non-isothermal model.

unknown parameters. Given sufficiently good data, we showed that our MA method can recover the correct local dark matter density even in the face of disc inhomogeneities, non-isothermal tracers and non-separability of the z-motion. Finally, we illustrated the power of our approach by applying it to *Hipparcos* data from the literature.

Our key results are as follows:

1. As noted previously by Bahcall (1984c), data up to high z ($|z| \sim 0.6\,\mathrm{kpc}$ – i.e. significantly larger than the Milky Way disc scale height) are required to break a degeneracy between the local dark matter density ρ_{dm}, and the local visible matter density ρ_{s}.

2. Methods that assume that the distribution function of a tracer population is a function only of the vertical energy $f = f(E_z)$ become systematically biased if the motion of the tracers is not truly separable in z. This effect becomes important when fitting to data that extend to heights larger than the disc scale height – as is necessary to break the ρ_{dm}-ρ_{s} degeneracy (c.f. point (i), above). The initial conditions in our simulation were separable, but as the disc evolves and reaches a true equilibrium, the distribution function is no longer separable. If we assume that $f = f(E_z)$, then this introduces a systematic error that we have no way to correct. For this reason, we favour moment based methods that assume nothing about the form of f.

3. We introduced a new minimal assumption (MA) method for recovering the local matter and dark matter densities ρ_{tot} and ρ_{dm}. Our method is based on solving the combined Jeans-Poisson equations using an MCMC technique to marginalise over the unknown parameters. We showed that our MA method can correctly recover both ρ_{dm} and ρ_{s} even in the face of disc inhomogeneities, non-separability of the z-motion, and vertical non-isothermality of the tracers, provided that the run of dispersion with height of the tracers $\overline{v_{z,i}^2}(z)$ is known.

4. Our derived MA method is very sensitive to the precise form of $\overline{v_{z,i}^2}(z)$ for the tracers. For this reason, we interpolate the measured data (marginalising out any velocity uncertainties), rather than assuming a functional form.

By contrast, the form of $\overline{v_{z,i}^2}(z)$ for the other disc components in the mass model is not important; we may safely assume that these are isothermal.

5. We applied our new MA method to recent data from Holmberg & Flynn (2000, 2004). We first made the assumption that the star tracer populations (A, F, K stars) were isothermal. This recovered $\rho_{\rm dm} = 0.003^{+0.009}_{-0.007}\,{\rm M}_\odot\,{\rm pc}^{-3}$ (90 per cent confidence), consistent with previous determinations. If, however, we assume instead a non-isothermal profile similar to the blue disc stars from SDSS DR-7 (Abazajian et al., 2009) measured by Bond et al. (2010), we obtain a fit with a very similar χ^2 value, but with $\rho_{\rm dm} = 0.033^{+0.008}_{-0.009}\,{\rm M}_\odot\,{\rm pc}^{-3}$ (90 per cent confidence). This illustrates the importance of measuring $\overline{v_{z,i}^2}(z)$ for the tracers.
6. A combination of good statistics, precise knowledge of the local amount of visible matter, and a good measure of $\overline{v_{z,i}^2}(z)$ for the tracers is crucial for obtaining an accurate unbiased measure of $\rho_{\rm tot}$ and $\rho_{\rm dm}$. This will become possible with future generation Galactic surveys.

2.6 Appendix

2.6.1 Introduction of dimensionless variables

In Section 2.2.1 and 2.2.2 we presented the basic equations used to calculate the potential in the MA and HF method. In this Appendix we re-write these equation (namely equations 2.8, 2.14 and 2.11) using dimensionless variable to simplify the calculations (Bahcall, 1984a,b,c).

The Poisson equation 2.11 can be rewritten as:

$$\frac{\partial^2 \Phi}{\partial z^2} = 4\pi G \nu_{0,1} \left(\sum_{i=1}^{N} \frac{\nu_i(z)}{\nu_{0,1}} + \epsilon \right) \tag{2.27}$$

with $\epsilon = \rho_{\mathrm{dm}}/\nu_{0,1}$ ($i = 1$ indicates the population with the largest scale height).

The following dimensionless variables can then be introduced:

$$\phi = \frac{\Phi}{\overline{v^2_{z,1}}} \tag{2.28}$$

$$z_1 = \sqrt{\frac{\overline{v^2_{z,1}}}{2\pi G \nu_{0,1}}} \tag{2.29}$$

$$x = z/z_1 \tag{2.30}$$

$$\alpha_i = \overline{v^2_{z,1}}/\overline{v^2_{z,i}} \tag{2.31}$$

$$\xi_i = \nu_{0,i}/\nu_{0,1} \tag{2.32}$$

$$\epsilon = \rho_{\mathrm{dm}}/\nu_{0,1} \tag{2.33}$$

and the solution to equation 2.13 becomes:

$$\nu_i(z) = \nu_{0,i} \exp[-\alpha_i \phi(z)] \tag{2.34}$$

Using this and the above dimensionless quantities we can write:

$$\frac{d^2\phi}{dx^2} = 2\sum_{i=1}^{N} \xi_i \exp(-\alpha_i \phi) + 2\epsilon \tag{2.35}$$

with $\phi(0) = 0$ and $d\phi(0)/dx = 0$. For a specified ratio of the mass densities in the plane (ξ_i) and the velocity dispersions ($\alpha_i^{1/2}$), equation 2.35 can then be integrated numerically for any ϵ.

Finally, for the minimal assumption (MA) method, we must define an additional dimensionless variable:

$$\alpha_{i,z} = \overline{v_{z,1}^2}(0)/\overline{v_{z,i}^2}(z) \tag{2.36}$$

In this way we can write the solution to equation 2.13 and 2.11 as:

$$\nu_i(z) = \xi_i \frac{\alpha_{i,z}}{\alpha_i} \exp\left(-\int_0^x \alpha_{i,z} \frac{d\phi}{dx} dx\right) \tag{2.37}$$

$$\frac{d^2\phi}{dx^2} = 2\left[\sum_{i=1}^{N} \xi_i \frac{\alpha_{i,z}}{\alpha_i} \exp\left(-\int_0^x \alpha_{i,z} \frac{d\phi}{dx} dx\right) + \epsilon\right]. \tag{2.38}$$

2.6.2 The SPH analysis method

The local density, velocity dispersion and derivatives for the Jeans equation terms are extracted from the simulation using weighted sums over the particles as in Smoothed Particle Hydrodynamics (Gingold & Monaghan, 1977; Lucy, 1977; Monaghan, 1992).

The density is given by:

$$\nu_i = \sum_{j}^{N} m_j W(|\mathbf{r}_{ij}|, h_i) \tag{2.39}$$

where h_i and m_j are the smoothing length and mass of particle i and j, respectively; we define $\mathbf{r}_{ij} = \mathbf{r}_i - \mathbf{r}_j$ and similarly for other vectors; and W is a symmetric kernel that obeys the normalisation condition:

$$\int_V W(|\mathbf{r} - \mathbf{r}'|, h) \mathrm{d}^3 r' = 1 \tag{2.40}$$

and the property:

$$\lim_{h\to 0} W(|\mathbf{r}-\mathbf{r}'|, h) = \delta(|\mathbf{r}-\mathbf{r}'|) \tag{2.41}$$

In the limit $N \to \infty, h \to 0$ (and using $m_j/\nu_j \to \mathrm{d}^3r'$) equation 2.39 recovers the continuum density.

The smoothing lengths h_i were adapted to ensure a fixed enclosed mass $M_{\text{p1sec:SPH}} = mN_{\text{p1sec:SPH}}$ where m is the mass of a particle and $N_{\text{p1sec:SPH}} = 128$ is the neighbour number. We used the standard cubic spline smoothing kernel for W (Monaghan, 1992).

The velocity dispersion tensor is given by:

$$\sigma_{ab,i} = \frac{1}{\nu_i}\sum_j^N m_j v_{a,j} v_{b,j} W(|\mathbf{r}_{ij}|, h_i) \tag{2.42}$$

where $a, b = [0, 1, 2]$ give the index of the velocity vector and velocity dispersion tensor, respectively.

Apart from the gradient of the gravitational potential that was taken directly from the tree (this is just the acceleration), gradients were calculated using a second order accurate polynomial reconstruction at each point in the collisionless fluid, as in Maron & Howes (2003) and references therein. Briefly, assuming that the fluid is smooth (and therefore differentiable), we can perform a polynomial expansion at second order about a point, i:

$$\begin{aligned} q_{ij} &= a_0 + a_1 x_{ij} + a_2 y_{ij} + a_3 z_{ij} + a_4 x_{ij}^2 + a_5 y_{ij}^2 + a_6 z_{ij}^2 + \\ &\quad a_7 x_{ij} y_{ij} + a_8 x_{ij} z_{ij} + a_9 y_{ij} z_{ij} + O(h^3) \end{aligned} \tag{2.43}$$

where $\mathbf{x_{ij}} = \mathbf{r}_{ij}/h_i = [x_{ij}, y_{ij}, z_{ij}]$ and q_i is the quantity we wish to differentiate at particle i (e.g. the density).

The coefficients of this expansion can then be determined by inverting the following 10×10 matrix equation:

$$\mathbf{Ma} = \mathbf{q} \tag{2.44}$$

where:

$$\mathbf{a}^{\mathrm{T}} = [a_0, a_1, a_2, a_3, a_4, a_5, a_6, a_7, a_8, a_9] \tag{2.45}$$

$$\begin{aligned}\mathbf{q}^{\mathrm{T}} &= \textstyle\sum_j^N m_j q_j \overline{W}_{ij} \quad [1, x_{ij}, y_{ij}, z_{ij}, x_{ij}^2, y_{ij}^2, z_{ij}^2, \\ &\qquad\qquad\qquad x_{ij}y_{ij}, x_{ij}z_{ij}, y_{ij}z_{ij}]\end{aligned} \tag{2.46}$$

$$\begin{aligned}\mathbf{M} \;=\; \sum_j^N m_j \overline{W}_{ij} & \left(\begin{array}{ccc} 1 & x_{ij} & y_{ij} \cdots \\ x_{ij} & x_{ij}^2 & x_{ij}y_{ij} \cdots \\ y_{ij} & y_{ij}x_{ij} & y_{ij}^2 \cdots \\ z_{ij} & z_{ij}x_{ij} & z_{ij}y_{ij} \cdots \\ x_{ij}^2 & x_{ij}^3 & x_{ij}^2y_{ij} \cdots \\ y_{ij}^2 & y_{ij}^2x_{ij} & y_{ij}^3 \cdots \\ z_{ij}^2 & z_{ij}^2x_{ij} & z_{ij}^2y_{ij} \cdots \\ x_{ij}y_{ij} & x_{ij}^2y_{ij} & x_{ij}y_{ij}^2 \cdots \\ x_{ij}z_{ij} & z_{ij}x_{ij}^2 & x_{ij}z_{ij}y_{ij} \cdots \\ y_{ij}z_{ij} & y_{ij}z_{ij}x_{ij} & z_{ij}y_{ij}^2 \cdots \end{array} \right. \\ & \begin{array}{llll} \cdots z_{ij} & x_{ij}^2 & y_{ij}^2 & z_{ij}^2 \cdots \\ \cdots x_{ij}z_{ij} & x_{ij}^3 & x_{ij}y_{ij}^2 & x_{ij}z_{ij}^2 \cdots \\ \cdots y_{ij}z_{ij} & y_{ij}x_{ij}^2 & y_{ij}^3 & y_{ij}z_{ij}^2 \cdots \\ \cdots z_{ij}^2 & z_{ij}x_{ij}^2 & z_{ij}y_{ij}^2 & z_{ij}^3 \cdots \\ \cdots x_{ij}^2z_{ij} & x_{ij}^4 & x_{ij}^2y_{ij}^2 & x_{ij}^2z_{ij}^2 \cdots \\ \cdots y_{ij}^2z_{ij} & y_{ij}^2x_{ij}^2 & y_{ij}^4 & y_{ij}^2z_{ij}^2 \cdots \\ \cdots z_{ij}^3 & z_{ij}^2x_{ij}^2 & z_{ij}^2y_{ij}^2 & z_{ij}^4 \cdots \\ \cdots x_{ij}y_{ij}z_{ij} & y_{ij}x_{ij}^3 & x_{ij}y_{ij}^3 & x_{ij}y_{ij}z_{ij}^2 \cdots \\ \cdots x_{ij}z_{ij}^2 & z_{ij}x_{ij}^3 & x_{ij}z_{ij}y_{ij}^2 & x_{ij}z_{ij}^3 \cdots \\ \cdots y_{ij}z_{ij}^2 & y_{ij}z_{ij}x_{ij}^2 & z_{ij}y_{ij}^3 & y_{ij}z_{ij}^3 \cdots \end{array} \\ & \left. \begin{array}{lll} \cdots x_{ij}y_{ij} & x_{ij}z_{ij} & y_{ij}z_{ij} \\ \cdots x_{ij}^2y_{ij} & x_{ij}^2z_{ij} & x_{ij}y_{ij}z_{ij} \\ \cdots x_{ij}y_{ij}^2 & y_{ij}x_{ij}z_{ij} & y_{ij}^2z_{ij} \\ \cdots z_{ij}x_{ij}y_{ij} & x_{ij}z_{ij}^2 & y_{ij}z_{ij}^2 \\ \cdots x_{ij}^3y_{ij} & x_{ij}^3z_{ij} & x_{ij}^2y_{ij}z_{ij} \\ \cdots x_{ij}y_{ij}^3 & y_{ij}^2x_{ij}z_{ij} & y_{ij}^3z_{ij} \\ \cdots z_{ij}^2x_{ij}y_{ij} & x_{ij}z_{ij}^3 & y_{ij}z_{ij}^3 \\ \cdots x_{ij}^2y_{ij}^2 & y_{ij}x_{ij}^2z_{ij} & x_{ij}y_{ij}^2z_{ij} \\ \cdots z_{ij}x_{ij}^2y_{ij} & x_{ij}^2z_{ij}^2 & x_{ij}y_{ij}z_{ij}^2 \\ \cdots z_{ij}x_{ij}y_{ij}^2 & y_{ij}x_{ij}z_{ij}^2 & y_{ij}^2z_{ij}^2 \end{array} \right)\end{aligned} \tag{2.47}$$

and $\overline{W}_{ij} = \frac{1}{2}[W_{ij}(h_i) + W_{ij}(h_j)]$ is the symmetrised smoothing kernel (the superscript $^{\mathrm{T}}$ means transpose).

Having determined all of the coefficients of $\mathbf{a}$ (by solving $\mathbf{a} = \mathbf{M}^{-1}\mathbf{q}$), the gradients of q evaluated at i then simply follow as:

$$\frac{\partial q_i}{\partial x} = a_1; \frac{\partial q_i}{\partial y} = a_2; \frac{\partial q_i}{\partial z} = a_3 \tag{2.48}$$

2.6.3 Results for the evolved simulation (cylinders)

In Section 2.3.3.2 we applied the HF and the MA method to the evolved simulation, considering several wedge shaped volumes at a Galactocentic distance $R = 8.5\,\mathrm{kpc}$ around the disc. These wedge-shaped volumes allowed us to sample the star particles sufficiently well that we could study systematic errors on the recovery of the local density, without being affected by sampling errors.

In this Appendix, we consider also the effects of sample error on the evolved simulation. We show the results for smaller cylindrical volumes at $R = 8.5\,\mathrm{kpc}$ identical to those used to study the unevolved simulation in Section 2.3.3.1. These volumes have a sampling and a shape similar to the *Hipparcos* data analysed by Holmberg & Flynn (2000) ($\sim 2000 - 3000$ within $|z| < 200\,\mathrm{pc}$). In Figure 2.21, we show the results for the MA method using cylindrical volumes. Now, due to the smaller volume sampled, the velocity dispersion $\overline{v_z^2}(z)$ is quite noisy. To deal with this problem, we use the MCMC to marginalise over the velocity errors. At each iteration at the MCMC, we draw a value of $\overline{v_z^2}(z)$ for each z-bin. We assume a Gaussian error distribution with a width corresponding to the uncertainty on $\overline{v_z^2}(z)$. (Note that this approach is readily adapted to real data where $\overline{v_z^2}(z)$ is also likely to be noisy and uncertain.) As can be seen in Figure 2.21, we can recover the correct value of the local visible, dark matter and total densities inside the errors for most of the volumes. Because of the poorer sampling, the uncertainties on the local density values are larger than the those obtained with the wedges (see Figure 2.16).

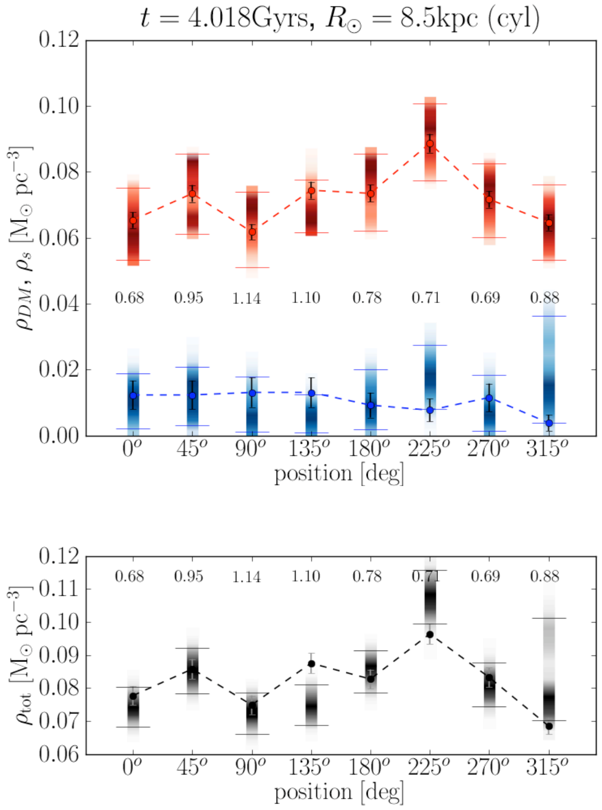

Figure 2.21: Models explored by the MCMC for the MA method for 8 cylindrical ‘Solar neighbourhood’ volumes applied to the evolved simulation at $R = 8.5\,$kpc. *Upper panel:* recovered values of dark and visible matter density. *Lower panel*: recovered values of the total (dark+visible) matter density. The symbols and colours are as in Figure 2.15.

Acknowledgments

We would like to thank Lawrence M. Widrow and John Dubinski for providing us with their latest version of the GalactICS code and the parameters for the initial condition of our Milky Way like galaxy; Chris Flynn for giving us the *Hipparcos* data from Holmberg & Flynn (2004) and for many useful comments; and Hanni Lux for providing the structure of the MCMC code used in this work. Justin I. Read would like to acknowledge support from SNF grant PP00P2_128540/1.

Chapter 3

A new determination of the local dark matter density from the kinematics of K dwarfs

This chapter has been published
in MNRAS 425, 1445-1458, 2012 (Garbari et al., 2012);
its author are Silvia Garbari, Chao Liu, Justin I. Read and George Lake.

Abstract

We apply a new method to determine the local disc matter and dark halo matter density to kinematic and position data for $\sim$ 2000 K dwarf stars taken from the literature. Our method assumes only that the disc is locally in dynamical equilibrium, and that the 'tilt' term in the Jeans equations is small up to $\sim 1\,\mathrm{kpc}$ above the plane. We present a new calculation of the photometric distances to the K dwarf stars, and use a Monte Carlo Markov Chain to marginalise over uncertainties in both the baryonic mass distribution, and the velocity and distance errors for each individual star. We perform a series of tests to demonstrate that our results are insensitive to plausible systematic errors in our distance calibration, and we show that our method recovers the correct answer from a dynamically evolved N-body simulation of the Milky Way. We find a local dark matter density of $\rho_{\mathrm{dm}} = 0.025^{+0.014}_{-0.013}\,\mathrm{M_{\odot}pc^{-3}}$ ($0.95^{+0.53}_{-0.49}\,\mathrm{GeV\,cm^{-3}}$) at 90% confidence assuming no correction for the non-flatness of the local rotation curve, and $\rho_{\mathrm{dm}} = 0.022^{+0.015}_{-0.013}\,\mathrm{M_{\odot}pc^{-3}}$ ($0.85^{+0.57}_{-0.50}\,\mathrm{GeV\,cm^{-3}}$) if the correction is included. Our 90% lower bound on ρ_{dm} is larger than the canonical value typically assumed in the literature, and is at mild tension with extrapolations from the rotation curve that assume a spherical halo. Our

result can be explained by a larger normalisation for the local Milky Way rotation curve, an oblate dark matter halo, a local disc of dark matter, or some combination of these.

3.1 Introduction

The local dark matter density is an average over a small volume, typically a few hundred parsecs, around the Sun. It provides constraints on the local halo shape and allows us to predict the flux of dark matter particles in laboratory detectors. The latter is required to extract information about the nature of a dark matter particle from such experiments, at least in the limit of a few tens to hundreds of detections (?). The Galactic halo shape can be constrained by combining two methods of determining the local dark matter density. Firstly, one can infer it from the Galactic rotation curve ($\rho_{\mathrm{dm}}^{\mathrm{ext}}$). This requires an assumption about the shape of the Galactic halo (typically spherical; e. g. Sofue et al., 2009; Weber & de Boer, 2010; Catena & Ullio, 2010). Secondly, one can calculate the dark matter density locally from the vertical kinematics of stars near the Sun (ρ_{dm}) (e. g. Bahcall, 1984c; Holmberg & Flynn, 2000). If $\rho_{\mathrm{dm}} < \rho_{\mathrm{dm}}^{\mathrm{ext}}$, this suggests a prolate dark matter halo for the Milky Way; while $\rho_{\mathrm{dm}} > \rho_{\mathrm{dm}}^{\mathrm{ext}}$, could imply either an oblate halo or a dark disc (Lake, 1989; Read et al., 2008; Read et al., 2009).

Determining the local matter density from the kinematics of stars in the Solar Neighbourhood has a long history dating back to Oort (1932, 1960) in the 1930's. Oort used the classical method of solving the combined Poisson-Boltzmann equations for a sample of stars, assumed to be stationary in the total matter distribution of the disc. He found 50% more mass than the sum of known components. A more modern study by Bahcall (1984c) introduced a new method that described the visible matter as a sum of isothermal components. He also found dynamically significant dark matter in the disc[1] (Bahcall, 1984b). Using faint K dwarfs at the South Galactic Pole, Bahcall et al. (1992) confirmed his earlier result that more than 50% of the mass was dark, although with a lower statistical significance.

---

[1] We should be careful about what we mean by 'dark matter in the disc'. Early studies like Oort (1932) were typically interested in missing disc-like matter (a 'thin dark disc'); more modern studies try to constrain a significantly more extended dark matter halo that has a near-constant dark matter density up to $\sim 1\,\mathrm{kpc}$. Even the 'dark disc' predicted by recent cosmological simulations (Read et al., 2008; Read et al., 2009) is sufficiently hot that its dark matter distribution is approximately constant up to $\sim 1\,\mathrm{kpc}$. Throughout this paper when we talk about 'dark matter in the disc' we refer to a constant density dark matter component within the disc volume.

However, the early studies by Oort (1932, 1960) and Bahcall (1984c,b) assumed that different tracers could be simply averaged to form a single tracer population. Kuijken & Gilmore (1989a) demonstrated that the two samples of F stars analysed by Bahcall (1984c) were not compatible (i.e. they had different spatial density distribution, but no evidence for a difference in their kinematics) and therefore should not be averaged. They re-analysed the K giant sample used by Bahcall (1984b), assigning more realistic errors to the density profile and using a more detailed fit to the velocity data, finding a value of total matter density compatible with the observed one. They concluded that the determination of the local volume density remained limited by systematic and random errors with the available data.

With the launch of the ESA satellite Hipparcos (1997), the kinematics and position of tracer stars were measured with much higher accuracy. The improved distance measures give a much more accurate measurement of the local luminosity function, so that the total amount of visible matter can be better estimated as well. The latest dynamical measurements of the local density of matter – $\rho_{\rm tot}$ – from Hipparcos data show no compelling evidence for a significant amount of dark matter in the disc (Crézé et al., 1998; Holmberg & Flynn, 2000). Holmberg & Flynn (2000) found $\rho_{\rm tot} = 0.102 \pm 0.01 {\rm M}_\odot {\rm pc}^{-3}$, with a contribution of about $0.095 {\rm M}_\odot {\rm pc}^{-3}$ in visible matter, consistent with the Kuijken & Gilmore (1989)'s value.

In addition to the local volume density, several authors have calculated the local *surface density* of gravitating matter, probing up to larger heights above the disc plane (typically ~ 1 kpc; e.g. Kuijken & Gilmore, 1989b; Kuijken & Gilmore, 1989, 1991; Holmberg & Flynn, 2004). Using faint K dwarfs at the South Galactic Pole, and using a prior from the rotation curve, Kuijken & Gilmore (1989, 1991) find $\rho_{\rm dm}^{\rm KG} = 0.010 \pm 0.005$ ${\rm M}_\odot$ ${\rm pc}^{-3}$, consistent with that expected from the rotation curve assuming a spherical Galactic dark matter halo[2] (e. g. Sofue et al., 2009; Weber & de Boer, 2010; Catena & Ullio, 2010). A similar result was found in the post-Hipparcos era by Holmberg & Flynn (2004). Recently, Moni Bidin et al. (2012) have estimated the surface density using tracers at heights $1.5 < z < 4$ kpc above the disc, making a rather stronger claim (incompatible with the earlier results of Kuijken & Gilmore (1991) and Holmberg & Flynn (2004)) that there

---

[2] Note that this consistency with the rotation curve is somewhat circular since this is input as a prior in their analysis.

is no dark matter near the Sun. However, Bovy & Tremaine (2012) demonstrate that this result is erroneous and owes to one of ten assumptions used by Moni Bidin et al. (2012) being false. Furthermore, Sanders (2012) estimate that the velocity dispersion gradients derived by Moni Bidin et al. (2012) could be biased by up to a factor of two, which would also significantly alter their determination of ρ_{dm}.

With next generation surveys round the corner (e.g. Gaia; Jordan, 2008), a significant improvement in the number of precision astrometric, photometric and spectroscopic measurements is expected. For this reason, Garbari et al. (2011) (hereafter Paper I[3]) revisited the systematic errors in determining ρ_{dm} from Solar Neighbourhood stars; these will likely soon become the dominant source of error, if they are not already. We were the first to use a high resolution N-body simulation of an isolated Milky Way-like galaxy to generate mock data. We used these mock data to study a popular class of mass modelling methods in the literature that fit an assumed distribution function to a set of stellar tracers (Holmberg & Flynn, 2000; Binney & Tremaine, 2008). We found that realistic mixing of stars due to the formation of a bar and spiral arms (similar to those observed in the Milky Way) breaks the usual assumption that the distribution function is separable, leading to systematic bias in the recovery of ρ_{dm}. We then introduced a new method that avoids this assumption by fitting instead moments of the distribution function (i.e. that solves the Jeans-Poisson equations). Our Minimal Assumption method (or MA method) uses a Monte Carlo Markov Chain technique (hereafter MCMC) to marginalise over remaining model and measurement uncertainties. Given sufficiently good data, we showed that our method recovers the correct local dark matter density even in the face of disc inhomogeneities, non-isothermal tracers and a non-separable distribution function.

In this article, we apply our MA method to real data from the literature. The key advantages of our new method over previous works are that: (i) we use a 'minimal' set of assumptions; (ii) we use a MCMC to marginalise over both model and measurement uncertainties; and (iii) we require no prior from the Milky Way rotation curve as has been commonly used in previous works (Kuijken & Gilmore, 1989, 1991; Holmberg & Flynn, 2000, 2004). This latter means that we can compare our determination to that derived from the rotation curve to constrain the Milky Way halo shape. Our method requires at least one

---

[3] Paper I (Garbari et al., 2011) constitutes the content of Chapter 2 of this thesis.

equilibrium stellar tracer population with known density fall off $\nu(z)$ and vertical velocity dispersion $\sigma_z^2(z)$, both as a function of height z. The requirements for a suitable sample of stellar tracers are that: (i) they are in dynamical equilibrium with the Galactic potential (i.e. they must be sufficiently dynamically old to have completed many vertical oscillations through the Galactic plane); (ii) they are available in sufficient numbers to give good statistical precision; (iii) they have reliable distances and vertical velocities v_z; (iv) the sample completeness needs to be sufficiently well understood in order to measure the density fall off as a function of the distance z from the disc plane; and (v) they extend up to 2-3 times the disc scale height (in order to break a degeneracy between the disc and dark matter densities; see Paper I[4]). While full six dimensional phase space information is now available for a large number of stars (e.g. RAVE Steinmetz 2003; Steinmetz et al. 2006; Zwitter et al. 2008; and SEGUE Yanny et al. 2009), these surveys are magnitude rather than volume complete, with additional survey selection effects based on colour. This makes it difficult to reliably estimate $\nu(z)$ for a given tracer population. For this reason, we return to the volume complete K-dwarf data from Kuijken & Gilmore (1989) for our disc tracers – the 'KG' data. These data consist of a photometric sample of 2016 K dwarf stars, complete in the z-range $\sim 0.2 - 1.5\,\mathrm{kpc}$, with a spectroscopic sample of 580 K dwarfs (most of which are included in the photometric catalogue). We use data from Hipparcos and SEGUE (Kotoneva et al., 2002; Zhang, 2012) to perform a new photometric distance measurement for each K dwarf star. We model the local gravitational potential using the baryonic mass distribution of the Galactic disc by Flynn et al. (2006).

This article is organised as follows. In Section 3.2, we present the K dwarf data from Kuijken & Gilmore (1989) (hereafter KG989II) and describe our new distance determinations (3.2.1). In Section 3.3, we summarise our MA mass modelling method (3.3.1) and, for comparison, the method adopted by KG89II (3.3.2). In Section 3.3.3, we test both methods on a mock data set derived from a dynamically evolved N-body simulation. In Section 3.4, we apply our MA method to the KG data and present our results. Finally in Section 3.5, we summarise and present our conclusions.

---

[4] Section 2.3.3.1 of this thesis.

3.2 Data

KG89II present a catalogue of 2016 K stars with photometry in B and V bands, and another of 580 K dwarfs (most of which are also included in the photometric catalogue) including radial velocities, at South Galactic pole (figure 3.1). The stellar density fall off of these tracers was derived from star counts. At large z, the mean metallicity of the stars is known to decrease below the Solar Neighbourhood value. Such a gradient translates into an absolute magnitude gradient, since the position of the main sequence in the colour-magnitude diagram changes with the metallicity: metal poor dwarfs are fainter than metal rich ones at the same temperature or colour (the opposite is true for giant stars). So, if there is a vertical metallicity gradient, the photometric parallaxes used for the derivation of the density fall off – $\nu(z)$ – will be systematically wrong as one moves away from the plane. Unfortunately, the metallicity could not be measured directly for these stars, so KG89II derived the density fall off using an assumed constant metallicity gradient for the K dwarfs. They considered two different gradients to estimate the magnitude of the uncertainties, namely $d[\mathrm{Fe/H}]/dz = 0$ (constant metallicity) and $d[\mathrm{Fe/H}]/dz = -0.3\,\mathrm{dex\,kpc^{-1}}$ (in their analysis KG89II consider this latter as the fiducial metallicity gradient for K dwarfs).

The tracers' vertical distance determination is fundamental for our analysis. Twenty years after KG89II's study, we can re-calibrate the distances for these stars using modern survey data to estimate the metallicity distribution function of K dwarfs at different z, and Hipparcos parallaxes to calibrate the photometric distances. Our distance re-calibration procedure is described, next.

3.2.1 A new distance determination for the K dwarfs

To calculate the vertical distances z for KG89II's sample, we must derive a relationship between the metallicity [Fe/H], the vertical distance z and the absolute magnitude M_V of K dwarf stars in the disc. Since the metallicity is not included in KG89II's catalogue, we can only hope to derive a distance distribution function $P_*(z)$ for each star of the sample, based on an observed metallicity distribution function for these stars.

We consider two different catalogues of K dwarfs with distances and metallicity for our calibration. The first catalogue by Kotoneva et al. (2002) consists of 431 K dwarfs from Hipparcos, representing a complete catalogue of the metal content

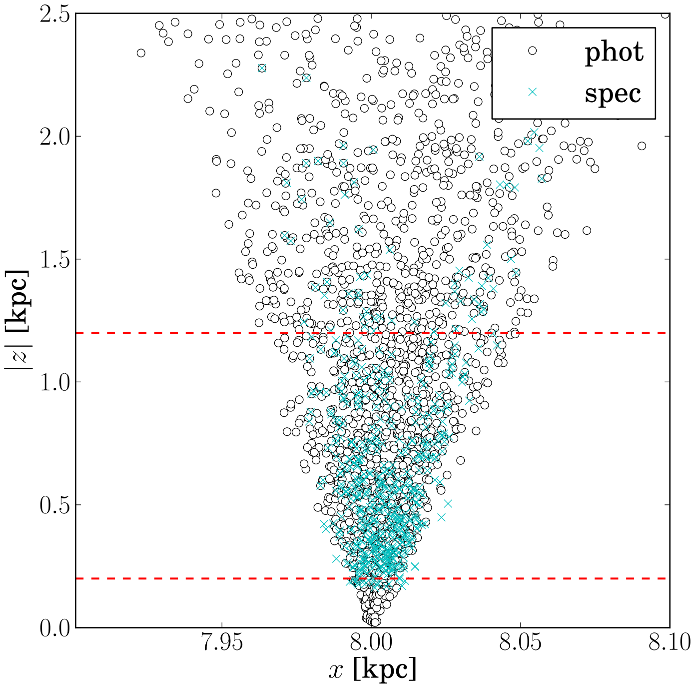

Figure 3.1: Spatial distribution of the K dwarf sample from KG89II. Blue crosses: spectroscopic sample; empty circles: photometric sample. The red dashed lines mark the range of $200 < z < 1200\,$pc use in our analysis (see Section 3.2.1).

in nearby K dwarfs extending up to $z \sim 100\,$pc. The vertical distances z for these stars are very accurately determined from Hipparcos parallaxes. The second catalogue by Zhang (2012) contains 5000 SEGUE K dwarfs spanning a much wider range of z, namely between 300 and 2000 pc. However, in this case, the distance determination for these stars is much less certain: the distance errors are about 10%.

We combine these two catalogues to build the metallicity distribution function (MDF) $Q([{\rm Fe/H}](z), z)$ for K dwarfs. Comparing the SEGUE metallicity distribution function at $z = 500\,$pc with the MDF from Kotoneva et al. (2002) for $z < 100\,$pc (see the red and black solid histograms in figure 3.2, respectively), we notice that the two MDFs have very similar shape, but shifted means. There is a vertical metallicity gradient from 0 to 500 pc of $\sim -0.4\,{\rm dex\,kpc^{-1}}$ (corresponding to a shift of $-0.2\,$dex; see figure 3.2 black dotted histogram). At larger height than this, the gradient is weaker: the SEGUE MDF at 1 kpc (dashed red histogram) is similar to the one at 500 pc. We adopt the Kotoneva et al. (2002) MDF in the Galactic plane, then we apply a linear metallicity gradient of $\sim -0.4\,{\rm dex\,kpc^{-1}}$ between 100 pc and 500 pc to match the SEGUE MDF at $z = 500\,$pc; we extend this shifted Kotoneva et al. (2002)'s MDF up to $z = 800\,$pc, and we adopt the SEGUE MDF for $z > 800\,$pc, as shown in figure 3.3. We explore an alternative $Q([{\rm Fe/H}](z), z)$ for the K dwarfs in Appendix 3.6.1.

With the metallicity distribution function $Q([{\rm Fe/H}](z), z)$ for K dwarfs, we next derive the distance probability distribution $P_*(z)$ for each star of the KG89II's catalogue. This requires calculating the relationship between z-distance and metallicity [Fe/H] for each star.

Figure 3.4 shows the absolute magnitude M_V (ordinate) of Kotoneva et al. (2002)'s K dwarfs as a function of colour index $B - V$ (abscissa) and metallicity [Fe/H] (colours). We fit this using a polynomial:

$$\begin{aligned} M_V = & a_{0,0} + a_{1,0}(B-V) + a_{0,1}[{\rm Fe/H}] + a_{2,0}(B-V)^2 + \\ & a_{1,1}(B-V)[{\rm Fe/H}] + a_{0,2}[{\rm Fe/H}]^2 + a_{0,3}(B-V)^3 \\ & a_{2,1}(B-V)^2[{\rm Fe/H}] + a_{1,2}(B-V)[{\rm Fe/H}]^2 \end{aligned} \tag{3.1}$$

The best-fit parameters are [−5.795, 27.92, 0.1291, −22.74, −2.003, 0.04917, 7.113, 1.02, −0.04274], with an error of $\sim 0.03\,$mag.

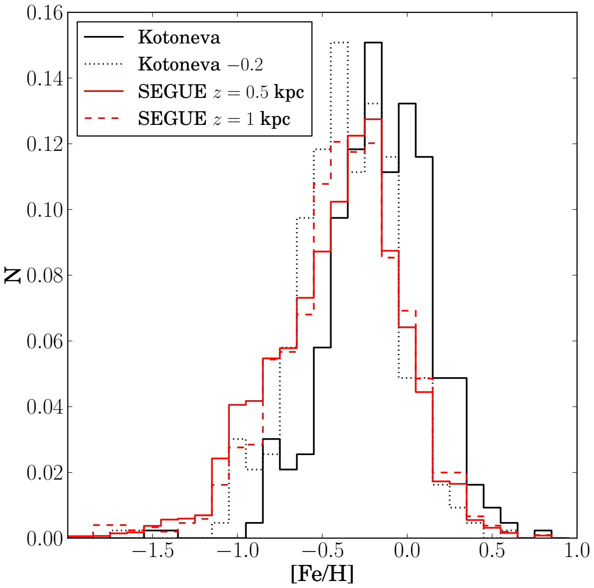

Figure 3.2: The $z \lesssim 100$ pc MDF (black solid histogram) from Kotoneva et al. (2002). A shift of 0.2 dex (black dotted histogram) approximately overlaps the MDF from SEGUE K dwarfs computed at $z \sim 500$ pc (red solid histogram). The red dashed histogram is the SEGUE MDF at $z \sim 1000$ pc.

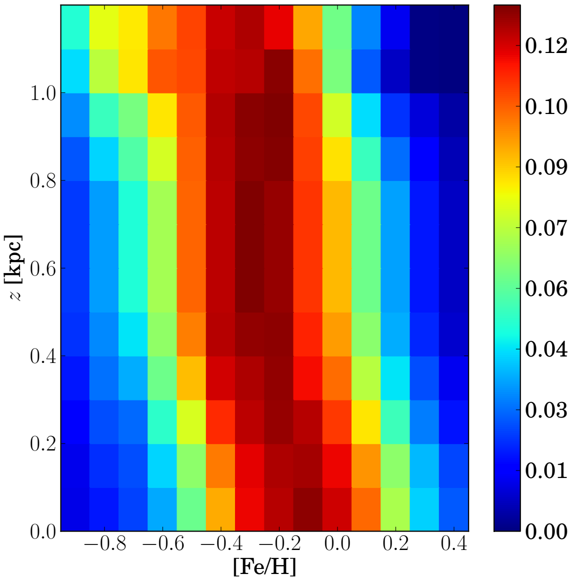

Figure 3.3: Combined MDF of Kotoneva et al. (2002) and SEGUE (Zhang, 2012). The colours show the probability values of [Fe/H] given z.

Once we have $M_V = M_V(B - V, [\mathrm{Fe/H}])$, we write the distance modulus as:

$$d = 10^{\frac{V - A_V - M_V + 5}{5}} = d(V, B - V, [\mathrm{Fe/H}]) \tag{3.2}$$

where V is the apparent magnitude and A_V is the extinction; we use the value $A_V = 0.062$ mag from Schlegel et al. (1998), given the mean Galactic coordinates of KG89II's data. The vertical distance z for a single star is then:

$$z_* = z_*(l, b, d) = z_*(l, b, B - V, [\mathrm{Fe/H}]) \tag{3.3}$$

where l and b are the Galactic longitude and latitude. We know l, b and $B-V$ for each star of KG89II's sample, so the only free parameter is [Fe/H]. This means that the vertical distance for each star will be given by a probability distribution $P_*(z)$ corresponding to a metallicity distribution $P_*([\mathrm{Fe/H}])$ for that star:

$$P_*(z) = P_*([\mathrm{Fe/H}](z)) \tag{3.4}$$

In practice, this equation must be solved iteratively because [Fe/H] is itself a function of z through equation 3.3. The iterative process proceeds as follows:

1. We start the first iteration by assuming that the distance distribution function of a single star is $P_*(z) = 1$ for all the possible $z([\mathrm{Fe/H}])$ calculated using equation 3.3.

2. The MDF marginalised over z for a single star is given by:

   $$P_*([\mathrm{Fe/H}]) = \int_0^\infty Q([\mathrm{Fe/H}](z), z) P_*(z) dz \tag{3.5}$$

   where $Q([\mathrm{Fe/H}](z), z)$ is the observed MDF at each z for all K dwarfs as described previously.

3. A new $P_*(z)$ is calculated through equation 3.4, using the $P_*([\mathrm{Fe/H}])$ just computed.

4. We restart steps 2 to 3 to calculate $P_*([\mathrm{Fe/H}])$ with the new $P_*(z)$ until it converges. For all stars, we obtained convergence in less than 5 iterations.

The density fall off of the photometric sample and the velocity dispersion of the spectroscopic one, obtained with our new distance estimates, are shown

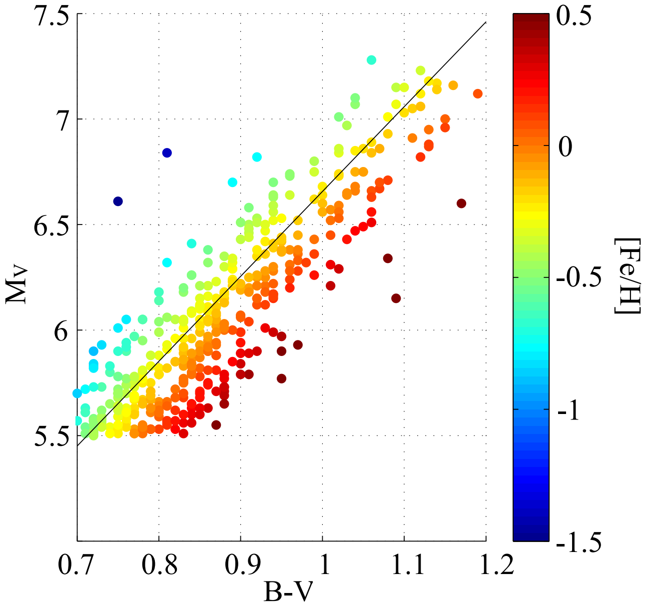

Figure 3.4: M_V as a function of colour $B - V$ and metallicity [Fe/H] for 431 K dwarfs selected from Kotoneva et al. (2002) (at heights $z < 100\,\mathrm{pc}$). The [Fe/H] is coded by colour. The black line is a linear fit to the data between $[\mathrm{Fe/H}] = -0.7$ and $0\,\mathrm{dex}$.

in figure 3.5. For our analysis, we use the density and the velocity dispersion profiles only over the range $200 < z < 1200\,\mathrm{pc}$ (red dashed lines). This assures that our sample is volume complete and avoids significant contamination by K giant stars Kuijken & Gilmore (1989). The corresponding quantities computed by KG89II, assuming a metallicity gradient of $-0.3\,\mathrm{dex/kpc}$, are plotted as a comparison (empty circles). Our new density profile and velocity dispersion do not differ greatly from those of KG89II; they are compatible within the quoted errors. In Appendix 3.6.1, we explore the effect of a rather extreme variation in the assumed MDF – ignoring Kotoneva et al. (2002) and SEGUE data – finding that our results are not sensitive to plausible changes in our distance calibration. The referee of this article pointed out that the study of Kotoneva et al. (2002) has been updated by Casagrande et al. (2007). The two studies are very much compatible, but the scatter in equation 3.1 of 0.03 mag becomes 0.27 mag when the newer data are used. We tested the impact of this larger scatter in magnitude on the distance calibration, finding that the density and velocity dispersion profile remain unchanged in the range of z of interest, with a negligible increase in the uncertainties.

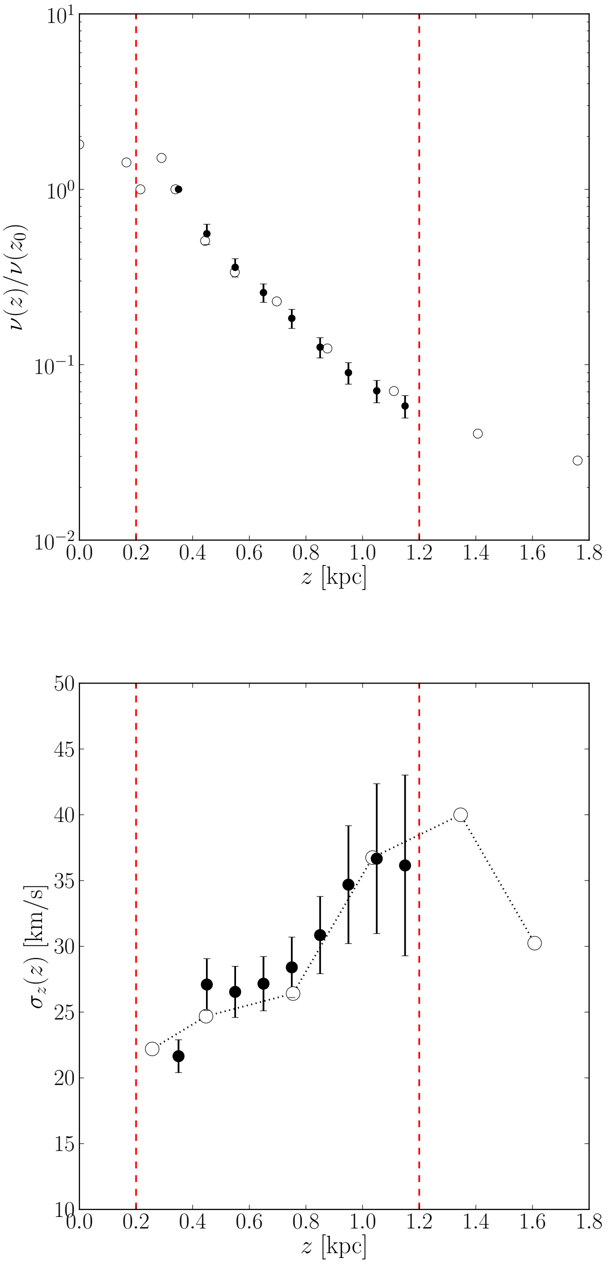

Figure 3.5: *Upper panel:* K dwarf stellar density profile (filled circles with error bars) derived from a Monte Carlo sampling of $P_*(z)$ for each star. As a comparison, the density profile (assuming a metallicity gradient of $-0.3\,$dex/kpc) from KG89II is plotted as empty circles. *Lower panel*: The similarly derived vertical velocity dispersion as a function of z (filled circles with error bars). The corresponding determination by KG89II is represented by the empty circles. In both panels, the two red dashed lines show the range of z considered in our analysis, over which the photometric sample is volume complete and we avoid significant contamination from K giants stars.

3.3 Method

3.3.1 The MA method

The MA method presented in Paper I uses the Poisson-Jeans system to predict the density fall off of a tracer population in a given gravitational potential. The comparison between this predicted density fall off and the observed one allows us to constrain the gravitational potential and, consequently, the underlying dark matter distribution.

Here we summarise the basic equations; for a detailed description of the MA method see Section 2.1 of Paper I[5].

The MA method is based on three main assumptions:

1. The system is in equilibrium (steady state assumption).
2. The dark matter density is constant over the range of $|z|$ considered.
3. The 'tilt' term $\frac{1}{R}\frac{\partial}{\partial R}\left(R\nu\sigma_{Rz}^2\right)$ in the cylindrical Jeans equation:

$$\frac{1}{R}\frac{\partial}{\partial R}\left(R\nu\sigma_{Rz}^2\right)+\frac{\partial}{\partial z}\left(\nu_i\sigma_z^2\right)+\nu_i\frac{\partial\Phi}{\partial z}=0 \tag{3.6}$$

   is negligible compared to all other terms. Here ν, σ_z^2 and σ_{Rz}^2 are the number density and the velocity dispersion components of a tracer population moving in potential Φ.

With these assumptions, the Jeans equation becomes a function only of z and we can neglect the other two Jeans equations in R and θ:

$$\sigma_z^2\frac{\partial\nu}{\partial z}+\nu\left(\frac{\partial\Phi}{\partial z}+\frac{\partial\sigma_z^2}{\partial z}\right)=0. \tag{3.7}$$

Solving this equation for a single tracer population, we obtain its density $\nu(z)$ at each height z:

$$\frac{\nu(z)}{\nu(z_0)}=\frac{\sigma_z^2(z_0)}{\sigma_z^2(z)}\exp\left(-\int_{z_0}^{z}\frac{1}{\sigma_z^2(z)}\frac{d\Phi}{dz}dz\right) \tag{3.8}$$

Given the density at the midplane $\rho_{{\rm s},j}(0)$ and the vertical velocity dispersion $\sigma_{z,j}^2(z)$ as a function of z for each of the gas and stellar populations in the local

---

[5] Section 2.2.1 of this thesis.

disc, we can model the full disc density distribution as a superposition of such elements:

$$\rho_{\rm s}(z) = \sum_j \rho_{{\rm s},j}(0) \frac{\sigma^2_{z,j}(0)}{\sigma^2_{z,j}(z)} \exp\left(- \int_0^z \frac{1}{\sigma^2_{z,j}} \frac{d\Phi}{dz} dz \right). \tag{3.9}$$

In Paper I, we showed that accurate measurement of the vertical velocity dispersion of the tracers $\sigma_z^2(z)$ is crucial, however in the mass modelling we can assume that all the visible matter components are isothermal – i.e. $\sigma^2_{z,j} = \sigma^2_{z,j}(0)$ – and equation 3.9 simplifies to:

$$\rho_{\rm s}(z) = \sum_j \rho_{{\rm s},j}(0) \exp\left(- \frac{\Phi(z)}{\sigma^2_{z,j}(0)} \right). \tag{3.10}$$

The Poisson equation then determines the potential Φ from the density. In cylindrical polar coordinates, this is given by:

$$\frac{\partial^2 \Phi}{\partial z^2} = 4\pi G(\rho_{\rm s}(z) + \rho^{\rm eff}_{\rm dm}) \tag{3.11}$$

with:

$$\rho^{\rm eff}_{\rm dm} = \rho_{\rm dm}(R) - (4\pi G R)^{-1} \frac{\partial}{\partial R} V_c^2(R) \tag{3.12}$$

where $\rho_{\rm dm}(R)$ is the halo mass density (following assumption 2, this is assumed to be independent of z in the volume considered); and $V_c(R) = (R\partial\Phi/\partial R)^{1/2}$ is the (total) circular velocity at a distance R (in the plane) from the centre of the Galaxy. For a flat rotation curve, the second term vanishes and $\rho^{\rm eff}_{\rm dm}(R) = \rho_{\rm dm}(R)$. The rotation curve correction can be calculated from the Oort constants A and B (Binney & Merrifield, 1998):

$$(4\pi G R)^{-1} \frac{\partial V_c^2}{\partial R} = \frac{B^2 - A^2}{2\pi G} \tag{3.13}$$

We solve equations 3.10 and 3.11 numerically for a given tracer population, adopting the following procedure:

1. We make initial trial guesses for $\rho_{{\rm s},j}(0)$, $\rho_{\rm dm}$, and the vertical velocity dispersion for the visible matter component in the plane $\sigma^2_{z,j}(0)$.

2. We solve equation 3.10 to obtain $\Phi(z)$ and its first derivative $\frac{\partial \Phi}{\partial z}$, with $\Phi(0) = \frac{\partial\Phi}{\partial z}\big|_0 = 0$.

3. We insert this result into equation 4.2 for the vertical density fall off of the tracers $\nu_{\mathrm{p}}(z)$ and we compare this with the observed distribution $\nu(z)$ to obtain a goodness of fit.

This procedure requires many input parameters, such as the normalisations and dispersions of each of the disc components, and the vertical dispersion profile of the tracers (typically poorly constrained). To explore the parameter space and marginalise over the uncertainties, we use a Monte Carlo Markov Chain (MCMC) method.

In Paper I we showed that our method is able to recover the correct value of the local dark matter density, even in presence of large visible matter density fluctuations due to the spiral arms. Notice that the MA requires no prior from the Milky Way rotation curve, as has been commonly used in previous works; this means that we can compare our determination to that derived from the rotation curve to constrain the Milky Way halo shape.

3.3.1.1 Application of the MA method to real data

When we apply the MA method to real data, we must deal with distance and velocity uncertainties, and account for survey geometry and/or the sample completeness. In particular, the K dwarf data from KG89II are not assigned distances, but instead, as described in Section 3.2.1, a z probability distribution function $P_*(z)$ for each star of the sample. In addition, the vertical velocities for each star are measured with an uncertainty of about $0.5 - 1\,$km/s. To marginalise over these uncertainties, we proceed in the following way:

1. For each model n of the MCMC, we select a different vertical distance z_n^* for each star in the sample, according to its z distribution function $P_*(z)$. We make sure that for each star included in both the spectroscopic and the photometric sample we pick a unique z_n^* value. For each star of the spectroscopic sample we also draw a vertical velocity value $v_{z,n}^*$ from a Gaussian distribution, according to its velocity error bar.

2. We bin the data in z to construct the observed density fall off $\nu_n(z)$ and velocity dispersion $\sigma_{z,n}^2(z)$ for the tracers, selecting stars with z between 0.2 and 1.2 kpc. The velocity dispersion is calculated using the velocity scale algorithm described in Beers et al. (1990).

3. We use the trial guesses for $\rho_{{\rm s},j,n}(0)$, $\sigma^2_{z,j,n}(0)$ and $\rho_{{\rm dm},n}$ to solve equation 3.10 and 3.11 to obtain $\Phi_n(z)$ and its first derivative $\frac{\partial\Phi_n}{\partial z}$.

4. We insert this result and the vertical velocity dispersion of the tracers $\sigma^2_{z,n}(z)$ into equation 4.2 to predict the tracers' density fall off. When applying the MA method to the real data, we add the visible matter surface density $\Sigma_{\rm s}$ as a further constraint. For each model of the MCMC we compute $\Sigma_{\rm s}$ as

$$\Sigma_{{\rm s},n} = 2\int_0^\infty \rho_{\rm s}(z)dz = \int_0^\infty \sum_j \rho_{{\rm s},j,n}(0)\exp\left(-\frac{\Phi_n(z)}{\sigma^2_{z,j,n}}\right) \tag{3.14}$$

5. We compare the predicted density fall off $\nu_{n,{\rm p}}(z)$ with $\nu_n(z)$, the predicted visible matter surface density $\Sigma^{\rm p}_{{\rm s},n}$ with the observed one ($\Sigma_{\rm s}$) and we calculate the corresponding χ^2_n, accepting or rejecting the model n.

6. When a model is accepted, we restart from 1 with the following model $(n+1)$ and so on, exploring the whole parameter space.

3.3.2 The KG method

KG89II used the K dwarf data to calculate the total surface density at the Sun position $\Sigma(R_\odot)$. Their approach (the KG method) is similar to the method adopted later by Holmberg & Flynn (2000, 2004) (the HF method), that we analysed in detail in Paper I.

Instead of measuring the vertical velocity dispersion of the tracers as a function of z to predict the density fall off, the HF method uses the tracers' velocity distribution function in the mid-plane of the Galactic disc $f_z(v_{z,0})$; assuming that the distribution function is separable, $f = f_{R,\theta}(v_R, v_\theta, R) \times f_z(v_z, z)$. Holmberg & Flynn (2000, 2004) integrate this distribution function over z-velocities to predict the density fall off of the tracers (see Section 2.2 of Paper I[6] for more details):

$$\nu(z) = \int_{-\infty}^{\infty} f_z(v_z, z)dv_z = 2\int_{\Phi(z)}^{\infty} \frac{f_z(E_z)dE_z}{\sqrt{2[E_z - \Phi(z)]}} \tag{3.15}$$

where $f_z(z, v_z) = f_z(E_z)$ and $E_z = \frac{1}{2}v_z^2 + \Phi(z)$ is the vertical energy. This equation

---

[6] Section 2.2.2 of this thesis.

can be written as:

$$\nu(z) = 2\int_{\sqrt{2\Phi(z)}}^{\infty} \frac{f_z(v_{z,0})v_{z,0}dv_{z,0}}{\sqrt{v_{z,0}^2 - 2\Phi(z)}} \tag{3.16}$$

where $v_{z,0}$ is the vertical velocity at the Galactic mid-plane ($z = 0$).

The MA demands only that the tilt term in the Jeans equation (3.6) is *small* with respect to the other terms, the HF method requires the stronger assumption that the z-motion (and so the distribution function) is completely separable from the motion in the radial and azimuthal directions; this latter implies that the tilt term is *exactly zero*.

The HF approach has the advantage of exploiting the whole available information about the shape of the velocity distribution function of the tracers. However, we demonstrated in Paper I that when the separability of the distribution function is not fulfilled, the HF method leads to biased results. Using a high resolution simulation of a Milky Way like galaxy, we showed that the onset of spiral arms and a bar can cause significant radial mixing that breaks the separability of the motion in the z and R directions, violating this key assumption of the HF method. This effect becomes increasingly important with height z. It is important to notice that the HF method can not be corrected for this bias since the separability of the potential (and of the distribution function) lies at the heart of the method. By contrast, in the MA method, the separability of the potential enters only in the neglected tilt term of the Jeans equation (that is assumed to be small as compared to the other terms). If the tilt term is for some reason large – i.e. the radial derivative of the density weighted tilt of the velocity ellipsoid is large – a correction can straightforwardly be applied to our MA method. However, we expect the tilt term to be small (see Paper I and Binney & Tremaine, 2008), and so we do not consider such a correction in this paper.

KG89II's approach relies on the same key assumption about the distribution function as the HF method. In most studies, the density $\nu(z)$ of the tracers is known to better precision than the velocity distribution $f_z(v_z, z)$. For this reason, KG89II work in the opposite direction with respect to Holmberg & Flynn (2000, 2004) and predict $f_z(v_z, z)$ from the observed $\nu(z)$. Applying an inverse Abel transform to equation 3.15, they obtain:

$$f_z(E_z) = \frac{1}{\pi}\int_{E_z}^{\infty} \frac{-d\nu/d\Phi}{\sqrt{2(\Phi - E_z)}}d\Phi. \tag{3.17}$$

so there is a unique relation between $\nu(\Phi)$ and $f_z(E_z)$. Notice that $f_z(E_z)$ depends on $\nu(\Phi(z))$ only at large z, where the potential exceeds E_z, i.e. beyond $z = \Phi^{-1}(E_z)$. Thus an additional key advantage of the KG method is that one can model the potential at large distances from the Galactic plane, ignoring the detailed distribution of matter at small z. KG89II parameterised the gravitational potential $\Phi(z)$ above the bulk of the disc matter (where it is sensitive only to the total surface density of gravitating matter) as:

$$\Phi(z) = K(\sqrt{z^2 + D^2} - D) + Fz^2 \tag{3.18}$$

where D is the disc scale height, K is proportional to the total disc surface density $\Sigma(R_\odot)$, and $F \propto \rho_{\rm dm}^{\rm eff}$ (the effective halo density). KG89II used a range of Galactic mass models (calculated using different values of the disc mass M, the radial disc scale-length $R_{\rm d}$, the circular velocity $V_c(R_\odot)$ and Sun position $R_\odot$) to *ensure* consistency with the Galactic rotation curve (assuming a spherical Milky Way halo) and therefore to obtain a relation between F and K. Note that already this is different from our MA approach where we use no information about the rotation curve to constrain our mass models.

Given the observed space density of a tracer population $\nu(z)$ and a set of gravitational potential models $\Phi(z)$, one can solve equation 3.17. To reduce the noise in the differential of $\nu(z)$, KG89II fitted it with a double exponential. KG89II then used the derived $f_z(E_z)$ for each potential model $\Phi(z)$ to compute the likelihood of the spectroscopic sample:

$$\mathcal{L} = \prod\nolimits_* \frac{f_z(E_{z,*})}{\int_0^\infty f_z(E_z)dE_z} \tag{3.19}$$

where the product is over all stars in the spectroscopic sample, and select the potential parameters that maximise this likelihood function $\mathcal{L}$.

The KG method, like the HF method, uses the full shape of the observed velocity distribution function, maximising the use of the available information. It is also convenient because it does not require a detailed model of the gravitational potential or an accurately measured tracer density fall off close to the Galactic plane. However, its drawback is that, like the HF method, it relies on a key assumption that the vertical distribution function is only a function of E_z. In the following section we test, using the high resolution N-body simulation described in Paper I, how this assumption affects the result derived using the KG method.

3.3.3 Testing the methods using an N-body simulation

Before applying the MA method to the real K dwarf data, we use the most dynamically evolved stage of the simulation described in Paper I as a mock data set, to test the effect of the velocity errors and of the asymmetric distance distribution function $P_*(z)$ on the MA method's result. Then we use the same mock data to probe how the non-separability of the tracers' distribution function affects the KG method.

The mock data consist of a high resolution (30 million disc star particles and 15 million halo dark matter particles) N-body simulation of an isolated Milky Way like galaxy. The initial conditions were built to contain some thousand stars in the volume size required for our analysis. With the dynamical evolution of the simulation, the disc developed a bar and spiral arms. For more details about the simulation features and how it compares to the real Milky Way, see Section 3.1 of Paper I[7].

We consider several volumes in the disc of the simulated galaxy at a distance of $R_\odot = 8.5\,\mathrm{kpc}$ from the centre. The MA method solves the Jeans equation for a one-dimentional slab (equation 3.7), so the radial size of the volumes, $\Delta R = 0.25\,\mathrm{kpc}$, is chosen to fulfil this approximation, but still contain an enough large number of stars (see Section 3.3.1.1 of Paper I[8] for more details).

As described in Section 3.3.1.1, we assign a different velocity value $v^*_{z,n}$ and a different z^*_n to each star at every iteration n of the MCMC. In the application of the MA method to the simulation, the velocity values are drawn from a Gaussian distribution centred on the true velocity value and with a width of 1 km/s, while the z values are selected from a lognormal distribution around the true value. Because of the numerical resolution of the simulation, we cannot fit the density profile up to 1.2 kpc, since at such height we quickly run out of star particles and the velocity dispersion is poorly measured, so we use stars with $0.2 \leq z \leq 0.75\,\mathrm{kpc}$. For the simulation data, we model the visible mass distribution as a

---

[7] Section 2.3.1 of this thesis.

[8] Section 2.3.3.1 of this thesis.

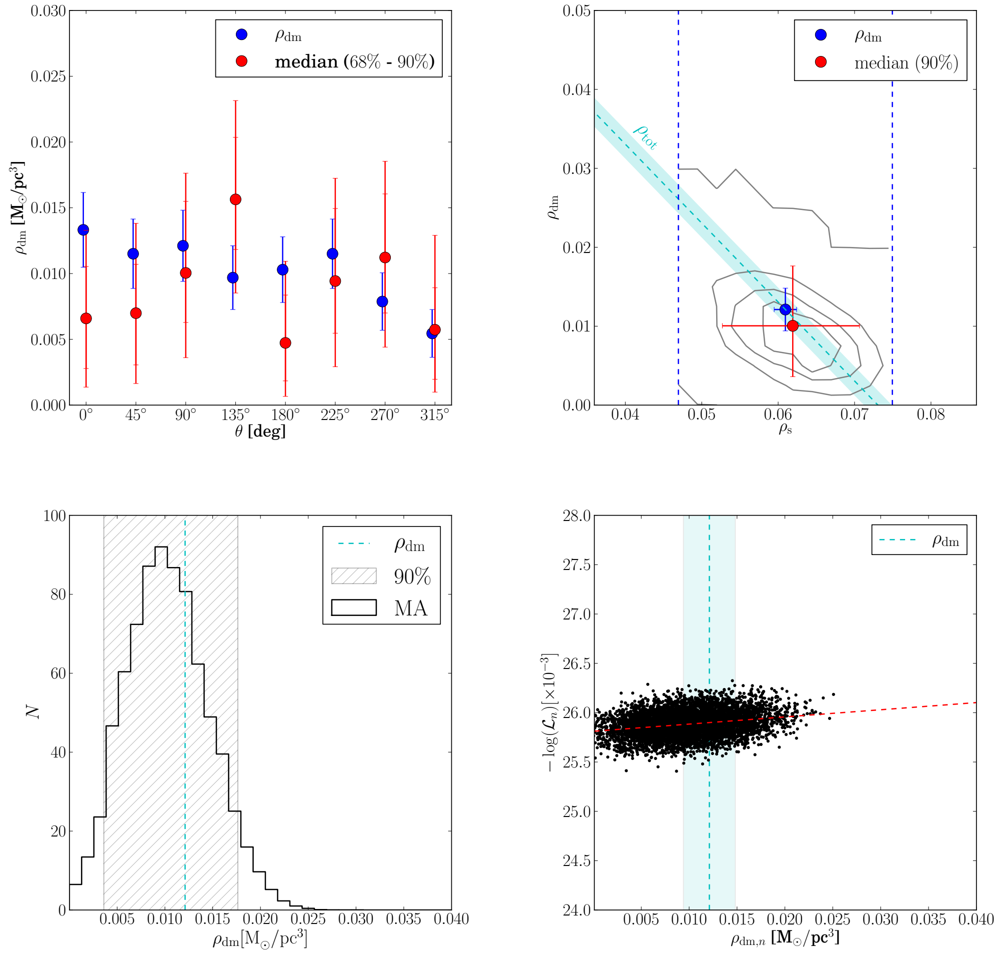

Figure 3.6: Results for recovering $\rho_{\rm dm}$ and $\rho_{\rm s}$ from the simulation. *Top left panel*: The recovered dark matter density (red filled circles) for all 8 volumes analysed around the disc (90% and 68% confidence intervals are shown). The actual value of the dark matter density is marked as a blue filled circle. *Top right panel*: The density of models explored by the MCMC projected onto $\rho_{\rm dm}$-$\rho_{\rm s}$ space for the 90° volume. The blue dot shows the true value for $\rho_{\rm dm}$ and $\rho_{\rm s}$; the diagonal cyan blue line shows the total matter density; and the red dot shows the median recovered $\rho_{\rm dm}$ and $\rho_{\rm s}$, with 90% errors marked. *Bottom left panel*: Histogram of the recovered $\rho_{\rm dm}$ from the MCMC mode ensemble for this same volume. The striped grey area is the 90% confidence interval. The cyan dashed line and shaded area give the actual value of $\rho_{\rm dm}$ with error bars. *Bottom right panel:* Testing the effect of assuming a separable distribution function. Each dot in this plot shows the likelihood L_n of each MCMC model calculated assuming a separable distribution function (see equation 3.17; the plot shows $-\log(\mathcal{L}_n)$, so the more likely models have a *lower* ordinate value). The red dashed line shows a fit to the points. Notice that assuming that the distribution function is separable produces a bias towards low $\rho_{\rm dm}$ (the true distribution function for the simulation is not separable; see figure 3.7). This bias effect was observed in all the volumes considered.

single component, characterised by its mass density $\rho_{{\rm s},j} = \rho_{\rm s}(0)$ and its velocity dispersion on the midplane $\sigma^2_{z,j} = \sigma^2_z(0)$. We let the dark matter density freely vary between 0 and 0.2 $\rm M_\odot\,pc^{-3}$, and the other parameters – $\rho_{\rm s}(0)$ and $\sigma^2_z(0)$ – vary inside their error bars. We adopted Poisson errors for the velocity dispersion $\sigma^2_z(0)$ and the current uncertainties on the total visible matter density in the plane (i.e. 0.014 $\rm M_\odot\,pc^{-3}$, see Section 3.4.1) for $\rho_{\rm s}(0)$. We include the rotation curve correction term, which can be easily computed for the simulation, in the calculation. We test convergence of our MCMC chains by starting with $\rho_{\rm dm}$ seeded at two different values (namely $\rho_{\rm dm} = 0$ and $\rho_{\rm dm} = 0.2\,\rm M_\odot\,pc^{-3}$) and running until the two chains are statistically indistinguishable.

In figure 3.6, the results for the MA method are shown. The upper left panel shows the results for eight different volumes around the simulated disc. Notice that in all cases, the mean correct answer (blue filled circles) is recovered within the 90% confidence interval, while for four out of eight of the patches (with a fifth at 45° extremely close) it is recovered with the 68% confidence interval. This is consistent with our confidence intervals having the meaning of a purely statistical error, despite each patch being systematically different (each patch samples a different region of the disc with different local dynamics). The remaining three panels focus on the results for the volume at 90°. The top right panel shows the density of models explored by the MCMC projected onto $\rho_{\rm dm}$-$\rho_{\rm s}$ space; the bottom left panel shows a histogram of the dark matter density for all the models explored by the MCMC; and the bottom right panel explores the effect of assuming a separable distribution function (of which more, next).

In Paper I, we noticed that, at this evolved stage of the simulation, the distribution function $f(v_R, v_\theta, v_z, R, z)$ of the tracers is not separable. This leads to the HF method producing biased results – either underestimating or overestimating the local dark matter density (see Section 3 of Paper I[9] for more details).

The separability of the distribution function lies at the heart of the KG method too. To reproduce a KG-like method, we consider all $\nu_n(z)$ and model potentials $\Phi_n(z)$ explored by our MA method MCMC chain. For each model in the chain, we then calculate a distribution function $f_{z,n}(E_z(v_z, \Phi))$ through equation 3.17 and use it to compute the likelihood $\mathcal{L}_n$ of the velocity data via equation 3.19.

In practice, the integral in the denominator of equation 3.19 is calculated numerically from $E_z^{\rm min} = 1$ to $E_z^{\rm max} = 7000\,\rm km^2\,s^{-2}$, which is chosen to avoid

---

[9] Section 2.3.3.2 of this thesis.

the divergence at $E_z = 0$ and to ensure we cover all energies of interest (the contribution of the high energy tail of $f_{z,n}(E_z)$ is negligible with respect to the low energy part; see figure 3.7).

In the bottom right panel of figure 3.6, the likelihoods $\mathcal{L}_n$ of the velocity data are plotted against the corresponding values of the local dark matter density for the different MCMC models $\rho_{{\rm dm},n}$. This panel shows that there is an anti-correlation between the computed likelihood $\mathcal{L}_n$ and the corresponding value of the local dark matter density $\rho_{{\rm dm},n}$: the likelihood of the velocity data is larger (i.e. $-\log(\mathcal{L}_n)$ is lower) for gravitational potential models with low $\rho_{{\rm dm},n}$; this means that we expect the KG method to artificially favour low dark matter density values. For all the explored volumes around the disc, we always obtain this same anti-correlation, so the bias on $\rho_{\rm dm}$ will have always the same sign.

To understand this effect, in figure 3.7 we show the distribution function $f_z(E_z)$ calculated from the same density profile $\nu(z)$, but using three potentials with different values of $\rho_{\rm dm}$, namely $\rho_{\rm dm} = 0$ (blue dashed line), the true value of $\rho_{\rm dm}$ (orange dashed line) and twice the true $\rho_{\rm dm}$ (red dashed line); the black line represents the actual distribution function of the stars in the volume. The potential corresponding to the true value of the dark matter density does not predict the distribution function correctly, while with $\rho_{\rm dm} = 0$ we obtain a better agreement with the measured $f_z(E_z)$. It is clear from this plot that the likelihood of models with low dark matter density, calculated through equation 3.19, will be higher than the true model. Therefore the KG method will be biased towards low $\rho_{\rm dm}$.

3.4 Results

3.4.1 Measuring the local matter and dark matter density

In the previous section, we showed that the MA method is able to recover the correct dark matter density within our 90% confidence interval, even in presence of asymmetric distance errors, velocity uncertainties and a non-separable distribution function. We now apply the MA method to the real K dwarf data, proceeding as described in Section 3.3.1.1. The mass distribution in the Galactic disc is modelled as a superposition of 15 isothermal components, listed in Table 3.1. As parameters to fit in the MCMC, we use the local dark matter density $\rho_{\rm dm}$,

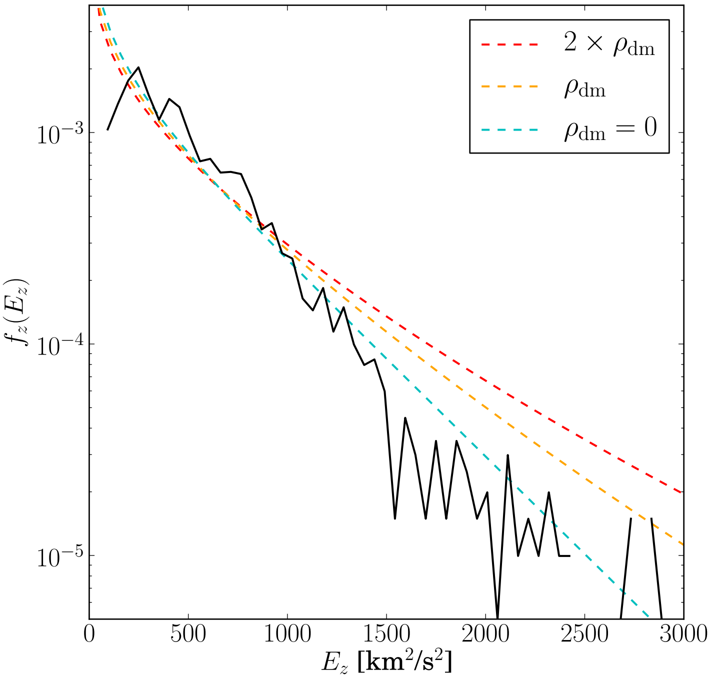

Figure 3.7: The distribution function – f – of the tracers in the simulation. The black line shows distribution function measured directly from the simulation averaged over a volume $8.375 < R < 8.625\,$kpc; $0.2 < z < 0.75\,$kpc. The orange dashed line shows $f_z(E_z)$ predicted from the density fall off $\nu(z)$ via equation 3.17, assuming the correct value of $\rho_{\rm s}$ and $\rho_{\rm dm}$ in the computation of the gravitational potential. The blue and red dashed lines show $f_z(E_z)$ predicted from $\nu(z)$, assuming $\rho_{\rm dm} = 0$ and twice $\rho_{\rm dm}$, respectively. All distribution functions are normalised by the integral of $f_z(E_z)$ between the minimum and the maximum E_z of the star particles in the volume considered.

the total visible density in the midplane $\rho_{\rm s}(0)$, and the relative fractions of the visible components $\rho_{{\rm s},j}(0)/\rho_{\rm s}(0)$ and their velocity dispersions in the midplane $\sigma_{z,j}$. We allow the densities and the velocity dispersions of the different components to vary within their measured uncertainties (the errors for each component are given in Table 3.1). We let the total visible density in the plane $\rho_{\rm s}(0)$ vary within its observed range: $\rho_{\rm s}(0) = 0.0914 \pm 0.0140\,{\rm M}_\odot\,{\rm pc}^{-3}$ (extrapolated from Table 3.1); and we let the dark matter density vary between 0 and $0.2\,{\rm M}_\odot\,{\rm pc}^{-3}$. For each model explored by the MCMC, we calculated the visible surface density $\Sigma^{\rm p}_{{\rm s},n}$ through equation 3.14 and compare it with the total surface density we obtain from Table 3.1, i.e. $\Sigma^{\rm obs}_{\rm s} \pm \Delta\Sigma^{\rm obs}_{\rm s} = 49.4 \pm 4.6$ ${\rm M}_\odot\,{\rm pc}^{-2}$, to calculate the total χ^2:

$$\chi^2 = \chi^2_{\rm surf} + \chi^2_\nu \tag{3.20}$$

where:

$$\chi^2_{\rm surf} = \frac{(\Sigma^{\rm obs}_{\rm s} - \Sigma^{\rm p}_{{\rm s},n})^2}{(\Delta\Sigma^{\rm obs}_{\rm s})^2} \tag{3.21}$$

and

$$\chi^2_\nu = \sum_{i=1}^{9} \frac{(\nu_{n,i} - \nu_{n,{\rm p},i})^2}{(\Delta\nu_{n,i})^2}, \tag{3.22}$$

where the sum is extended to all the bins and $\Delta\nu_{n,i}$ are the uncertainties on the density fall off.

The rotation curve correction term can be calculated from the Oort constants A and B. To determine the Oort constants, we must use stellar tracers that are well-mixed. The most recent estimates of A and B from F giants (Branham, 2010) and K-M giants (Mignard, 2000) from *Hipparcos* give $A = 14.85 \pm 7.47\,{\rm km\,s^{-1}\,kpc^{-1}}$ and $B = -10.85 \pm 6.83\,{\rm km\,s^{-1}\,kpc^{-1}}$ and $A = 14.5 \pm 1.0\,{\rm km\,s^{-1}\,kpc^{-1}}$ and $B = -11.5 \pm 1.0\,{\rm km\,s^{-1}\,kpc^{-1}}$, respectively. Averaging these two values we obtain a correction term of $-0.0033 \pm 0.0050\,{\rm M}_\odot\,{\rm pc}^{-3}$. We test for convergence of the MCMC by starting several chains at different initial values of all the parameters and running until they are statistically equivalent (after removing an initial burn-in phase of 100 accepted models for each chain).

The results for the MA method applied to the real K dwarf data are shown in figure 3.8. The upper panel shows the density of the models explored by the MCMC (grey contours) in the $\rho_{\rm s} - \rho_{\rm dm}$ plane; the median with 90% errors is shown by the black dot and corresponds to $\rho_{\rm dm} = 0.025^{+0.014}_{-0.013}\,{\rm M}_\odot\,{\rm pc}^{-3}$

Table 3.1: The disc mass model taken from Flynn et al. 2006. For each component in the table, we give the local mass density in the midplane $\rho(0)$ in $\mathrm{M_\odot pc^{-3}}$; the total column density Σ in $\mathrm{M_\odot pc^{-2}}$; and the vertical velocity dispersion $\sigma_{z,j}(0)$ in $\mathrm{km\,s^{-1}}$. Uncertainties on the densities are assumed to be 50% for all the gas components (indicated with *) and 20% for all of the stellar components. The largest uncertainties come from the gas that remains poorly constrained (compare, for example, compilations in Flynn et al. 2006, Binney & Merrifield (1998) and Ferrière (2001)). For the thick disc, the column density is well known, while the velocity dispersion and the volume density are poorly known such that they should have larger error bars. However, these two quantities are essentially nuisance parameters for our analysis here. Since they anti-correlate and – as pointed out by Kuijken & Gilmore (1989b) – the local gravitational potential is mainly constrained by the column density, we simply assume small errors for both here such that the integrated column agrees with the observed value.

Component	$\nu_{i,0}(0)$ $[\mathrm{M_\odot\,pc^{-3}}]$	Σ_i $[\mathrm{M_\odot pc^{-2}}]$	$\sigma_z^2(0)^{1/2}$ $[\mathrm{km\,s^{-1}}]$
H_2^*	0.021	3.0	4.0 ± 1.0
HI(1)*	0.016	4.1	7.0 ± 1.0
HI(2)*	0.012	4.1	9.0 ± 1.0
Warm gas*	0.0009	2.0	40.0 ± 1.0
Giants	0.0006	0.4	20.0 ± 2.0
$M_V < 2.5$	0.0031	0.9	7.5 ± 2.0
$2.5 < M_V < 3.0$	0.0015	0.6	10.5 ± 2.0
$3.0 < M_V < 4.0$	0.0020	1.1	14.0 ± 2.0
$4.0 < M_V < 5.0$	0.0022	1.7	18.0 ± 2.0
$5.0 < M_V < 8.0$	0.007	5.7	18.5 ± 2.0
$M_V > 8.0$	0.0135	10.9	18.5 ± 2.0
White dwarfs	0.006	5.4	20.0 ± 5.0
Brown dwarfs	0.002	1.8	20.0 ± 5.0
Thick disc	0.0035	7.0	37.0 ± 5.0
Stellar halo	0.0001	0.6	100.0 ± 10.0

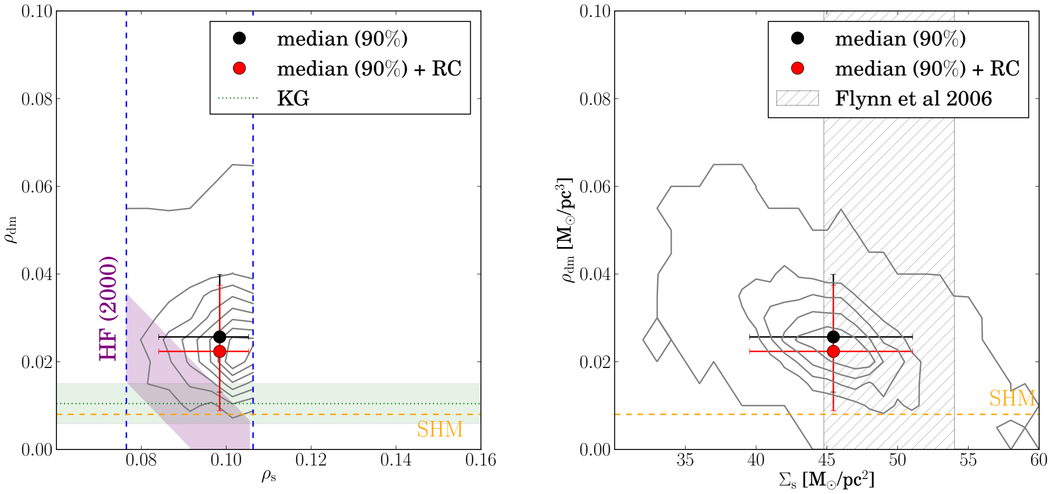

Figure 3.8: *Upper Panel:* The recovered visible and dark matter densities. The grey contours are the density of models explored by the MCMC. The black dot shows the median recovered value of $\rho_{\rm s}$ and $\rho_{\rm dm}$ with 90% errors marked; the red dot shows the same but including a correction for the local non-flatness of the Milky Way rotation curve (-0.0033 ± 0.0050 M$_\odot$ pc^{-3}). The purple area represents the values estimated by Holmberg & Flynn (2000) (this appears as a diagonal stripe since these authors only constrained $\rho_{\rm dm} + \rho_{\rm s}$). The blue-dashed lines show our priors on $\rho_{\rm s}$. The horizontal dashed orange line marks the Standard Halo Model value of $\rho_{\rm dm}$ (0.008 M$_\odot$ pc^{-3}). The green area marks the range of $\rho^{\rm KG}_{\rm dm}$ we extrapolate from KG91. *Lower Panel:* The recovered dark matter density as a function of the visible matter surface density $\Sigma_{\rm s}$. The meaning of the symbols is the same as in the upper panel. The striped grey area is the range in the visible matter surface density determined by Flynn et al. (2006).

($0.95^{+0.53}_{-0.49}$ GeV cm^{-3})[10]; adding the rotation curve correction, we obtain $\rho_{\rm dm} = 0.022^{+0.015}_{-0.013}$ M$_\odot$pc^{-3} ($0.85^{+0.57}_{-0.50}$ GeV cm^{-3}, see the red dot in figure 3.8).

We expect the MA method to primarily constrain the total matter density in the plane $\rho_{\rm s} + \rho_{\rm dm}$, which means that we should see an oblique degeneracy between $\rho_{\rm s}$ and $\rho_{\rm dm}$ in the $\rho_{\rm s} - \rho_{\rm dm}$ plane, as was observed for the simulation (see figure 3.6). However, unlike the simulation that has only one visible matter component in the disc, our real-data mass model comprises some 15 separate components with different scale heights. This introduces new freedoms that wash out the oblique degeneracy in the $\rho_{\rm s} - \rho_{\rm dm}$ plane. If we plot instead, however, the *total surface density* of visible matter in the disc (bottom panel of figure 3.8) the

---

[10] 1 GeV cm^{-3} $\simeq$ 0.0263158 M$_\odot$ pc^{-3}.

degeneracy is once again clearly visible as a diagonal elongation of the MCMC model density contours. Notice that many of the models explored by the MCMC lie outside of the range given by the Flynn et al. 2006 mass model (grey striped band). This simply means that the prior we placed on Σ_{s} is not very strong. However, the full area explored is in good agreement with the more conservative measurements of the total visible matter surface density by Kuijken & Gilmore (1991) (hereafter KG91), namely $\Sigma_{\mathrm{s}} = 48 \pm 8\ \mathrm{M}_\odot\,\mathrm{pc}^{-2}$; and by Flynn & Fuchs (1994), $\Sigma_{\mathrm{s}} = 49 \pm 9\ \mathrm{M}_\odot\,\mathrm{pc}^{-2}$. Even if we include only models that lie within the grey striped region, our recovered ρ_{dm} is little affected.

In Appendix 3.6.2, we test the robustness of our result, exploring how it changes if one considers either only the low z bins ($0.2 < z < 0.7\,\mathrm{kpc}$) or only the high z bins ($0.6 < z < 1.2\,\mathrm{kpc}$). We find that the low z data do not provide any information about ρ_{dm}, but they still favour low Σ_{s} compared to the prior we imposed. The low z bins present a noisier and not monotonically increasing velocity dispersion, however they are better constrained and dominate the χ^2 fit. Using the high z data, we lose information about the disc and Σ_{s} settles into the centre of its prior distribution; this leads to a systematically lower ρ_{dm}, since the sum of the two is well constrained. This tells us that the origin of our high ρ_{dm} is the slightly lower Σ_{s} required by the velocity dispersion data near the plane.

We also tested the effect of changing the assumed errors on the baryonic mass model. We first reduce them to an optimistic 10% error for the stellar normalisations and 30% for the gas normalisations; this has little affect on the resulting determination of ρ_{dm} because sufficient freedom remains in our mass model to allow degeneracies between ρ_{dm} and the baryonic components (this reflects the broken degeneracy seen in figure 3.8). We then increased the errors by removing the prior on $\rho_{\mathrm{s}}(0)$ altogether. This also has a small effect on our recovered ρ_{dm}. This confirms the results shown in Appendix 3.6.2 that it is the velocity dispersion data, not our prior that are constraining our mass model. The low z ($\lesssim 500\,\mathrm{pc}$) data constrain the surface density profile of the disc, while the high z data ($\gtrsim 500\,\mathrm{pc}$) are dynamically sensitive to dark matter.

The green horizontal stripe in the upper panel of figure 3.8 marks the value of ρ_{dm} we extrapolate from KG89II and KG91. KG91, using the same K dwarf data analysed in this paper, determine the total dynamical surface density up to 1.1 kpc: $\Sigma_{\mathrm{dyn}} = 71 \pm 6\ \mathrm{M}_\odot\,\mathrm{pc}^{-2}$. If we subtract from this the contribution of the observed visible matter $\Sigma_{\mathrm{s}} = 48 \pm 8\ \mathrm{M}_\odot\,\mathrm{pc}^{-2}$, we can calculate ρ_{dm}, assumed to be constant in the range $0 < z < 1.2\,$kpc, as:

$$\rho_{\rm dm}^{\rm KG} = \frac{\Sigma_{\rm dyn} - \Sigma_{\rm s}}{2 \cdot 1100} \tag{3.23}$$

This gives: $\rho_{\rm dm}^{\rm KG} = 0.010 \pm 0.005$ $\mathrm{M}_\odot\,\mathrm{pc}^{-3}$.

Our new result from our MA method is in tension with $\rho_{\rm dm}^{\rm KG}$, obtained from the same data set. This could owe either to our different distance calibration or to our new MA method that does not require any assumption about the separability of the distribution function (see Section 3.3.3). In figure 3.5, we already showed that our new distance calibration does not significantly affect the velocity dispersion and the density fall off of the K dwarfs. In addition, in Appendix 3.6.1, we explore the effect of using a constant metallicity gradient for the K-dwarfs of $-0.3\,\mathrm{dex\,kpc}^{-1}$, exactly as assumed by KG89II. This metallicity distribution is not compatible with modern data; we only use it to illustrate the sensitivity of our results to the MDF of the K dwarf stars, and to fully understand why our determination of $\rho_{\rm dm}$ is larger than that of KG91. Using the KG89II's MDF, our recovered value of $\rho_{\rm dm}$ is slightly smaller and therefore in better agreement with KG89II and KG91. However, our median recovered value remains significantly larger than the upper bound of the KG91 result. This suggests that our new distance determinations are not the primary reason for the systematic shift.

In our tests on the N-body simulation (Section 3.3.3), we showed that, when the distribution function of the tracers is not separable, the method adopted by KG89II leads to a systematic underestimate of $\rho_{\rm dm}$. In the lower panel of figure 3.9, we plot the likelihood $\mathcal{L}_n$ of each model explored by our MCMC – calculated through equation 3.19 – against the corresponding value of $\rho_{\rm dm}$. Unlike the similar plot for our simulation data (figure 3.6, bottom panels), there is now a significant vertical dispersion in the models. This owes to the increased freedom present in our 15-parameter mass model for the real-data. However, the highest likelihood models (the bottom envelope of points in the plot) show a similar trend as seen for the simulation data: higher likelihood models have systematically smaller $\rho_{\rm dm}$. We conclude that the primary difference for our larger value of $\rho_{\rm dm}$ as compared to KG89II is that our MA method requires no assumption about the separability of the distribution function.

In the upper panel of figure 3.9, we plot a histogram of $\rho_{\rm dm}$ from all the models explored by the MCMC. The striped area is the 90% confidence interval (corresponding to the black dot of figure 3.8); the result including the rotation curve correction is shown by the red error bar. Notice that our 90% *lower bound* is larger than the Standard Halo Model[11] typically assumed in the literature (marked by the vertical dashed orange line). For a comparison, we plot the ranges of ρ_{dm} at the solar radius obtained by Iocco et al. (2011), combining microlensing and rotation curve measurements, and using different halo models: the blue error bar corresponds to a spherical halo, while the cyan and purple bars correspond to oblates halos with potential flattening $q = 0.9$ and $q = 0.7$, respectively. The magenta bar represents the dark matter density in presence of a dark disc, contributing $0.25 - 1.5$ times the dark matter (spherical) halo density, as predicted by Read et al. (2009).

From figure 3.9, we can see that our recovered density is in mild tension with the result for a spherical Milky Way halo. Moving to an oblate halo significantly reduces this tension, however a flattening of $q = 0.7$ is likely inconsistent with measurements of the halo shape from the Sagittarius stream of stars (e.g. Ibata et al., 2001). If we wish to explain our median value for ρ_{dm} that is very much larger than the canonical SHM value assumed in the literature, we require a local disc of dark matter that raises ρ_{dm} without significantly altering the rotation curve. Interestingly, our median value is in excellent agreement with the range of dark discs predicted for our Galaxy by Read et al. (2008); Read et al. (2009).

3.5 Discussion and conclusions

We have presented a new measurement of the local matter and dark matter densities from the kinematics of K dwarf stars near the Sun. We presented a new photometric distance calibration for the the K dwarf data of KG89II (the KG data), derived using modern survey catalogues and the Hipparcos satellite data. We then used these data as tracers of the local gravitational potential to calculate the visible (ρ_{s}) and dark matter (ρ_{dm}) densities at the solar position $R_\odot$ and the surface density of the Milky Way disc up to 1.1 kpc above the plane (Σ_s).

To determine ρ_{dm} and ρ_{s}, we applied our new mass modelling method (presented already in Paper I) that relies on a minimum set of assumptions (the MA method) to the rejuvenated KG data. The key advantages of our new method are

---

[11] The SHM is an isothermal sphere model for the Milky Way's dark matter halo with a value of the dark matter velocity dispersion assumed to be $\sigma_{\mathrm{iso}} \simeq 270\,\mathrm{km\,s^{-1}}$.

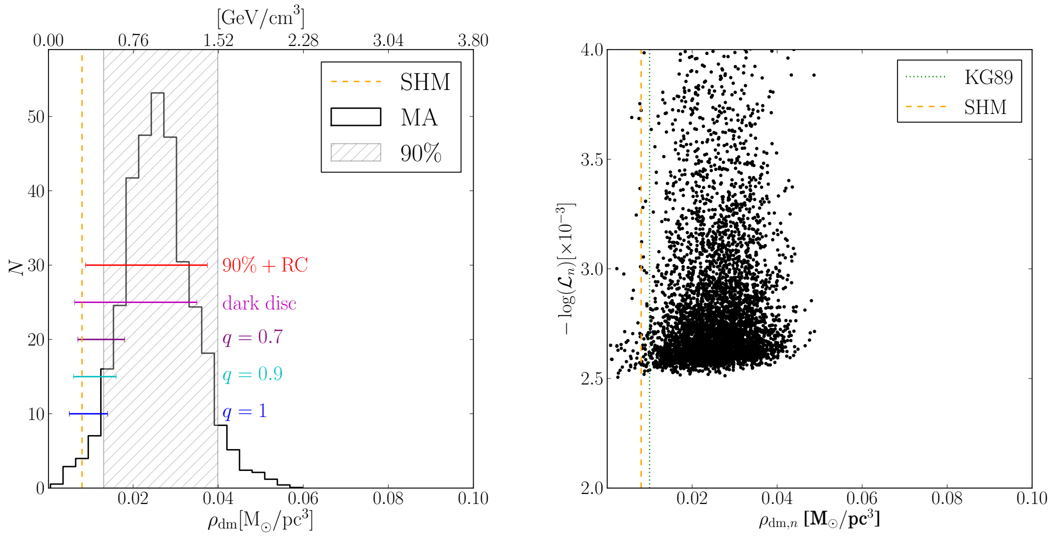

Figure 3.9: *Upper panel:* A histogram of the recovered $\rho_{\rm dm}$ from our MCMC chains for the MA method applied to the real K dwarf data. The striped grey area is the 90% confidence interval. The orange dashed line is the SHM value of $\rho_{\rm dm}$; the blue, cyan and purple error bars correspond to the value of $\rho_{\rm dm}$ obtained by Iocco et al. (2011) from a combination of microlensing and rotation curve data, with a spherical halo (potential flattening $q = 1$) and two oblate halos, with $q = 0.9$ and $q = 0.7$, respectively. The magenta error bar is the value of $\rho_{\rm dm}$ expected if the Milky Way has a dark disc contributing $0.25 - 1.5$ times the density of the (spherical) halo. The red error bar corresponds to our result after adding the rotation curve correction. *Lower panel:* The effect of assuming a separable distribution function. Each dot shows the likelihood of a given MCMC model calculated assuming a separable distribution function. Notice that the assumption of separability biases the result towards low $\rho_{\rm dm}$. The orange and the green dashed lines have the same meaning as in the upper panel of 3.8.

that: (i) we do not require any hypothesis about the shape of the tracers' velocity distribution function; (ii) we use a MCMC to marginalise over uncertainties in the distances and velocities of the tracer stars, and the underlying baryonic mass model for the visible disc; and (iii) we require no prior from the Milky Way rotation curve as has been commonly used in previous works. This latter means that we can compare our determination to that derived from the rotation curve to constrain the Milky Way halo shape. We used a dynamically evolved high resolution N-body simulation of a Milky Way-like galaxy as a mock data set to test our MA method, finding that we could correctly recover $\rho_{\rm dm}$ and $\rho_{\rm s}$ within our 90% confidence interval (for eight sample Solar neighbourhood-like volumes) even in the face of disc inhomogeneities, non-isothermal tracers, asymmetric distance errors and a non-separable tracer distribution function. Furthermore, we confirmed the result from our Paper I that assuming a separable distribution function (as has been typically done in the modern literature) leads to a biased determination of $\rho_{\rm dm}$.

Applying our MA method to the K dwarf data, we obtain a new measurement of the local dark matter density: $\rho_{\rm dm} = 0.025^{+0.014}_{-0.013}$ $\rm M_\odot\,pc^{-3}$ ($0.95^{+0.53}_{-0.49}$ GeV cm^{-3}); which, adding a correction for the local non-flatness of the rotation curve correction term ($\simeq -0.0033 \pm 0.0050$, see Sections 3.3.1 and 3.4), gives: $\rho_{\rm dm} = 0.022^{+0.015}_{-0.013}$ $\rm M_\odot pc^{-3}$ ($0.85^{+0.57}_{-0.50}$ GeV cm^{-3}). Our new value is systematically larger than the results from KG89II and KG91 derived from the same data. We show that this primarily owes to our new MA modelling method (and the fact that it does not assume a separable distribution function for the tracers); our new distance determination for the K dwarfs plays a more minor role. At the same time we determine a value of the local visible matter density of $\rho_{\rm s} = 0.098^{+0.006}_{-0.014}$ $\rm M_\odot\,pc^{-3}$ that largely reflects the prior from our baryonic mass model. Our median value of the local dark matter density is larger than previous determinations. However, we stress that this is only a 90% confidence result (in one out of eight patches in our simulated mock data, our method over-estimated $\rho_{\rm dm}$ by $\sim 90\%$).

Our error bars are larger than is often quoted in the literature, however they reflect the full combination of model systematic, measurement and statistical uncertainties. Other recent determinations either rely on the rotation curve and therefore a strong assumption about the Milky Way halo shape, or require a large number of assumptions with associated (and typically unmodelled) systematic errors.

In addition to measuring $\rho_{\rm dm}$ and $\rho_{\rm s}$, we also obtain an estimate of the baryonic disc mass up to $z = 1.1$ kpc above the disc plane: $\Sigma_{\rm s} = 45.5^{+5.6}_{-5.9}\,{\rm M_\odot pc^{-2}}$ at 90% confidence. This is slightly lower than the mean of the prior from our baryonic mass model: $\Sigma_{\rm vis} = 49.4 \pm 4.6$ $\rm M_\odot\,pc^{-2}$. Splitting the number into the contribution from stars and stellar remnants: $\Sigma_* = 33.4^{+5.5}_{-5.2}$ $\rm M_\odot\,pc^{-2}$ and gas: $\Sigma_{\rm g} = 12.00^{+1.9}_{-2.0}$ $\rm M_\odot\,pc^{-2}$, we see that our model favours slightly lower surface density in both the gas and the stars than the mean of our priors ($\Sigma_{\rm g}^{\rm obs} = 13.3 \pm 3.4$ $\rm M_\odot\,pc^{-2}$, $\Sigma_*^{\rm obs} = 36.1 \pm 3.0$ $\rm M_\odot\,pc^{-2}$).

It is this tendency for our models to favour lower disc surface density that leads to our high median value for $\rho_{\rm dm}$ (see figure 3.8 and Appendix 3.6.2). Unfortunately, current estimates of the stellar and gaseous inventory in the Solar neighbourhood are too uncertain to confirm or rule out our favoured $\Sigma_{\rm s}$ (e.g. Bovy et al., 2012; Ferrière, 2001).

Despite our large error bars, our new value for $\rho_{\rm dm}$ has some potentially interesting implications. Firstly, it is larger at 90% confidence than the Standard Halo Model value of $\rho_{\rm dm}^{\rm SHM} = 0.008$ $\rm M_\odot\,pc^{-3}$ ($0.30\,{\rm GeV\,cm^{-3}}$), usually adopted in the literature. This is particularly important for direct detection experiments because it implies a larger flux of dark matter particles and therefore a greater chance of detection. Secondly, our result is in mild tension with the value of $\rho_{\rm dm}^{\rm ext}$ extrapolated from the rotation curve measurements, assuming a spherical dark matter halo. If confirmed by better data, this means that the halo of our Galaxy is oblate and/or that we have a disc of dark matter in the Galaxy, as predicted by recent cosmological simulations (see upper panel of figure 3.9]).

3.6 Appendix

3.6.1 Testing the robustness of the MDF

The most uncertain quantity in our re-analysis of KG89II's data is the variation of the K dwarfs' metallicity distribution function with z, $Q([{\rm Fe/H}](z), z)$. In this appendix, we investigate how the adopted metallicity distribution function affects the result of our analysis by exploring a different model for this function. We use the gradient adopted by KG89II, i.e. $-0.3\,{\rm dex\,kpc^{-1}}$, and set the mean metallicity to 0 at $z = 0$ (see upper left panel of figure 3.10). This MDF is *not* compatible with modern metallicity data for the K dwarfs (see figure 3.2); we use it simply to illustrate our sensitivity to the assumed MDF, and to aid comparisons with the earlier KG89II results.

In figure 3.10, we show the velocity dispersion (upper right panel) and the density fall off (lower left panel) of the tracers derived using the above MDF. In the lower right panel of figure 3.10, the recovered dark and visible matter density are shown. The value of $\rho_{\rm dm}$ obtained is slightly lower than that derived using our default MDF, namely $\rho_{\rm dm} = 0.022^{+0.013}_{-0.012}\,{\rm M_\odot\,pc^{-3}}$, or $\rho_{\rm dm} = 0.018^{+0.014}_{-0.013}\,{\rm M_\odot\,pc^{-3}}$ including the rotation curve correction. However, our median value for $\rho_{\rm dm}$ is still high and the overall result remains in tension with the SHM value (even when using this incorrect MDF). We conclude that our results are robust to plausible variations in the assumed MDF.

In addition to the above, we also tested the impact of a different extinction value used in equation 3.2 on our results. We chose $A_V = 0$ and $A_V = 0.1$. For $A_V = 0$ ($A_V = 0.1$) the distances are slightly overestimated (underestimated) with respect to the extinction values considered in this article. This does not affect much the density fall off, but it translates mainly in a slightly flatter (steeper) velocity dispersion. This leads to a small decrease (increase) of the recovered value of $\rho_{\rm dm}$. However the impact of the extinction is very small compared to the other test shown in this Appendix.

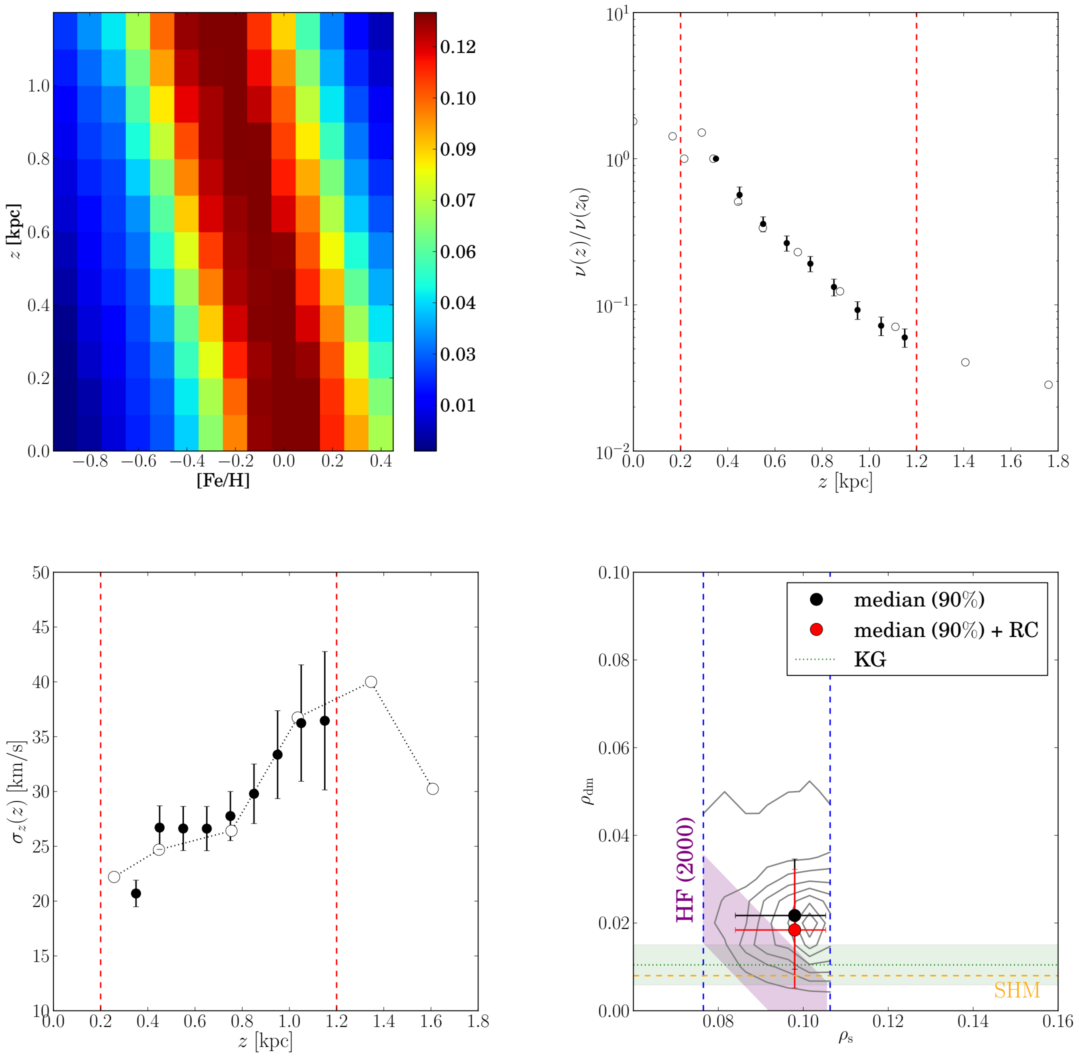

Figure 3.10: *Left upper panel:* The MDF adopted by KG89II: a constant metallicity gradient with height of 0.3 dex kpc^{-1} normalised to a metallicity of 0. dex at $z = 0$ kpc. *Right upper panel*: Stellar density profile derived from Monte Carlo sampling the probability distribution of z (dots with error bars). As a comparison, the density profile from KG89II is plotted as empty circles. The two red dashed lines show the completeness range. *Lower left panel*: The vertical velocity dispersion as a function of z. The black dots with error bar are derived from the probability distribution of z. *Lower right panel*: The projection of MCMC models onto the ρ_{dm}-ρ_{s} plane for our MA method applied to the K dwarf data, using the MDF shown in the top left panel to determine the distances. The colours and the symbols are as in figure 3.8.

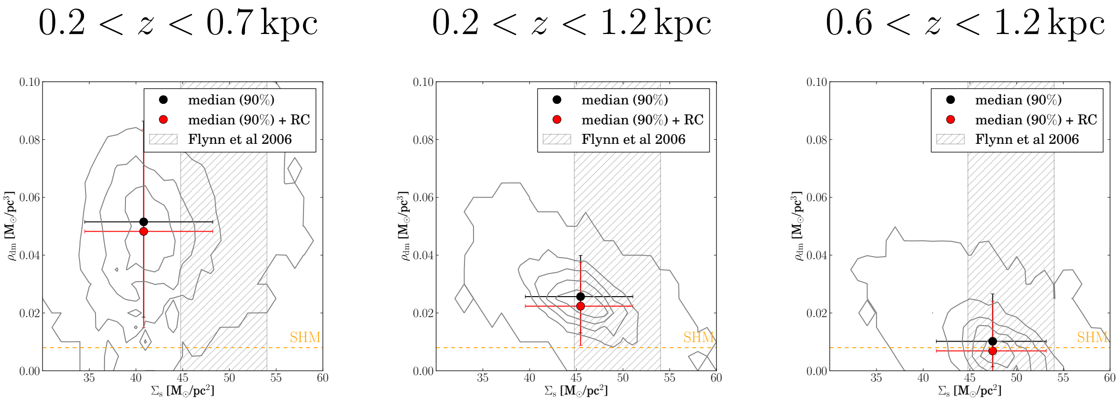

Figure 3.11: The recovered dark matter density as a function of the visible matter surface density $\Sigma_{\rm s}$. *Left panel:* considering only low z bins ($0.2 < z < 0.7$ kpc); *central panel:* considering the full z range: $0.2 < z < 1.2$ kpc (as lower panel of figure 3.8); *right panel:* considering only high z bins ($0.6 < z < 1.2$ kpc). The meaning of the symbols is the same as in figure 3.8. The striped grey area is the range in the visible matter surface density determined by Flynn et al. (2006), that we used as a (weak) prior.

3.6.2 Exploring the robustness of our $\rho_{\rm dm}$ determination

In this Appendix, we explore the robustness of our determination of $\rho_{\rm dm}$ by analysing a low z ($0.2 < z < 0.7$ kpc) and a high z ($0.6 < z < 1.2$ kpc) subset of the KG data. The results are shown in Figure 3.11. If we consider only the low z data (left panel), there is no information about the dark matter density. However, the data still favour low $\Sigma_{\rm s}$ compared to our prior. If only the high z data are used (right panel), we lose the information about the disc and $\Sigma_{\rm s}$ settles into more or less the centre of its prior distribution. This leads to a systematically lower $\rho_{\rm dm}$. The above suggests that the origin of our high median $\rho_{\rm dm}$ is the lower $\Sigma_{\rm s}$ favoured by the velocity dispersion data close to the plane.

Acknowledgments

We would like to thank Lan Zhang for kindly supplying the SDSS data we used to calculate the K dwarfs' metallicity distribution function. We thank Glenn Van de Ven for providing us the biweight code for the calculation of the velocity dispersions and for useful discussions. We would like to thank the referee Chris Flynn for a careful reading of the manuscript and useful comments. Finally, we would like to thank Fabio Iocco, Miguel Pato and Jo Bovy for useful discussions. We thanks Scott Tremaine for very useful comments that aided the clarity of our work. Justin I. Read would like to acknowledge support from SNF grant PP00P2_128540/1.

Chapter 4

Mapping the dark matter density in the Milky Way disc

This chapter presents ongoing work in collaboration with David Von Rickenbach, Justin Read and Chao Liu. In this chapter the results of the semester project “Mapping the dark matter density in the Milky Way disc” accomplished by David von Rickenbach – supervised by Justin Read and me – are presented in Section 4.3.

Abstract

We aim to measure, for the first time, the density of dark matter $\rho_{\mathrm{dm}}(R)$ at different radii in the disc of our Galaxy to probe the existence of an accreted disk of dark matter in the Milky Way (Lake, 1989). Such a disc, predicted by recent cosmological simulations, would contribute $0.25 - 1.5$ times the non-rotating halo density at the solar position (Read et al., 2008; Read et al., 2009). The large local dark matter density value obtained in Garbari et al. (2012)[1], provide support for this prediction. We first use N-body simulations as mock data sets to test the performance of the ‘Minimal Assumption’ (MA) method presented in Garbari et al. (2011)[2] at different radial positions in the Galactic disc and to study the detectability of the possible presence of a dark matter disc. Then we present a suitable sample of tracers that will be analysed to map $\rho_{\mathrm{dm}}(R)$. We choose Red Clump stars from the the PPMXL catalogue (Roeser et al., 2010), extending out to $R \sim 13\,\mathrm{kpc}$ from the Galactic centre, since these have good distance determinations. The preliminary analysis of the simulations indicates that the MA method recovers the dark matter density in the Galactic even at larger radii, where the

---

[1] Garbari et al. (2012) constitutes the content of Chapter 3 of this thesis.

[2] Garbari et al. (2011) constitutes the content of Chapter 2 of this thesis.

disc is more affected by the presence of non-equilibrium features (flares and warps) and can detect the presence of a dark disc. The analysis of the Red Clump stars and their distance and velocity determinations is ongoing.

4.1 Introduction

Recent cosmological simulations (Read et al., 2008; Read et al., 2009) predict that – once baryonic matter is included – a disc of dark matter is expected to form in our Galaxy from accreted satellites. The formation of this dark matter disc owes to the dynamical action of the accreting satellites against the baryonic disc. The stellar disc is the dominant component in mass inside the solar radius and its dynamical friction causes satellites to be preferentially dragged into the disc plane (Quinn & Goodman, 1986; Quinn et al., 1993). Satellites having a low inclination orbit with respect to the disc plane, are torn apart by tidal forces and not only accrete their stars into a Galactic disc, but also deposit their dark matter into a thick *dark disc* (Lake, 1989). This accreted dark matter disc is predicted to contribute $\sim 0.25 - 1.5$ times the density of the halo density at the Sun position and to rotate slower than the stellar disc (Read et al., 2009). Unlike tidal streams, the dark disc is an equilibrium structure and it is predicted in all the disc galaxies forming in a hierarchical cosmology.

The presence of a dark disc in the Milky Way would have important consequences for dark matter detection experiments. Weakly Interacting Massive Particles (WIMPs) are currently the favourite candidate for dark matter particles, as they are well motivated and detectable (Jungman et al., 1996). Many experiments have been recently designed to detect WIMPs in the lab (Aprile et al., 2005; CDMS Collaboration, 2009; Bernabei et al., 2008). Predicting the flux of dark matter particles through the Earth is fundamental for these experiments, both to design the detectors and to interpret any signal (Jungman et al., 1996). Although the dark disc has a local density comparable to the dark halo, its low velocity with respect to the Earth has the effect of boosting the capture of WIMPs in the Earth and the Sun (Bruch et al., 2009), increasing the annual modulation signal and enhancing the flux at low recoil energy (up to a factor of 3 in the 5-20 keV range; Bruch et al., 2009), that allows the particle mass to be determined. For this reason, we must determine whether the Milky Way has a significant dark disc and measure its properties.

Recently Garbari et al. (2011) (see Chapter 3) developed a new unbiased method - the 'MA method' - to calculate the local dark matter $\rho_{\rm dm}$ from the kinematics of stars in the vicinity of the Sun. The large local dark matter density (namely $\rho_{\rm dm} = 0.022^{+0.015}_{-0.013}\,{\rm M}_{\odot}{\rm pc}^{-3}$) obtained applying the MA method to K dwarfs in the solar neighbourhood (Garbari et al., 2012, see Chapter 3), is in tension with the Standard Halo Model[3] value (0.008 $\rm M_{\odot}\,pc^{-3}$), usually assumed in the literature, and favours an oblate shape for the dark matter halo and/or support the presence of a dark matter disc in our Galaxy.

In this work we map, for the first time, the dark matter density in the plane of the Milky Way, applying the MA method to stellar tracers at different Galactocentric positions R. These local determinations of $\rho_{\rm dm}$, are independent of any assumptions about the global potential of the Milky Way. Therefore, these measurements, combined with the extrapolation of $\rho_{\rm dm}$ from rotation curves, can provide constraints on the halo shape and/or on the possible presence of a dark disc. For the latter, it is important to study in more detail the expected signature of dark discs' density distribution.

To investigate how the MA method can be applied at different radial positions in the Milky Way disc, we need to test it on some mock data set. For this purpose we run two high resolution N-body simulations of mergers between a Milky Way like galaxy and a satellite galaxy, with two different orbit inclinations:

1. High inclination merger (60° with respect to the main galaxy's disc plane): this kind of merger will strongly damage the Milky Way disc, creating non-equilibrium features such as flares and warps. The analysis of this simulation allows us to determine how the presence of these structures in our Galaxy affect the method.

2. Low inclination merger (10°): we expect a dark disc forming in this merger. This simulation is used to determine whether the MA method can detect a dark disc and how its density changes as a function of radius. This result fixes which minimum data resolution necessary to detect the dark disc, distinguishing its contribution to $\rho_{\rm dm}$ from the Galactic halo.

We then apply the MA method to a suitable sample of tracers in the disc plane. We choose Red Clump stars from the PPMXL catalogue (Roeser et al.,

---

[3] The SHM is an isothermal sphere model for the Milky Way's dark matter halo with a value of the dark matter velocity dispersion assumed to be $\sigma_{\rm iso} \simeq 270\,{\rm km\,s^{-1}}$.

2010) catalogue, extending out to $R \sim 13\,\mathrm{kpc}$ from the Galactic centre. These stars are good distance indicators and they are bright giants extending far away in the disc, so they can be observed in a broad range of Galactocentric radii.

This work is in progress and the results for the real data are not ready yet, so in this chapter I will describe the project and the data, and present the preliminary results for the simulations. This work is a collaboration with David von Rickenbach, Justin Read and Chao Liu. I set up and run the simulations used for the tests and accomplished the numerical implementation of the MA method. David von Rickenbach, supervised by Justin Read and me, has accomplished the analysis of the simulations and applied the MA method to them. The data analysis is made in collaboration with Chao Liu.

The chapter is organised as follows: in Section 4.2 the basic equations of MA method are summarised. In Section 4.3 we describe the N-body simulation used as mock data set and results of the application of the MA method to them. Finally, in Section 4.4 we describe the data. The analysis of the data and the determination of the velocity dispersion and density profiles is ongoing, so we must defer the application of the MA method to those data to future works. In Section 4.5 we present our conclusion for this first part of the project.

4.2 Method

We apply the Minimal Assumptions method, presented in Garbari et al. (2011), to stellar tracers in several volumes at different radial position in the Galactic disc. The MA method (described in details in Section 2.2.1, see Section 1.2.2 for the complete theoretical derivation) solves the Poisson-Jeans system to predict the density fall off $\nu(z)$ of a tracer population in a given gravitational potential. The gravitational potential Φ and, consequently, the visible and dark matter densities (ρ_{s} and ρ_{dm}) in the analysed volume, are constrained comparing this predicted density fall off with the observed one.

The MA method is based on only three hypothesis:

1. The system is in equilibrium (steady state assumption).

2. The dark matter density is constant over the range of $|z|$ considered.

3. The 'tilt' term $\frac{1}{R}\frac{\partial}{\partial R}\left(R\nu\sigma_{Rz}^2\right)$ in the cylindrical Jeans equation:

$$\frac{1}{R}\frac{\partial}{\partial R}\left(R\nu\sigma_{Rz}^2\right)+\frac{\partial}{\partial z}\left(\nu_i\sigma_z^2\right)+\nu_i\frac{\partial\Phi}{\partial z}=0 \tag{4.1}$$

   is negligible compared to all other terms. Here ν, σ_z^2 and σ_{Rz}^2 are the number density and the velocity dispersion components of a tracer population moving in potential Φ.

With the above assumptions, the Jeans equation becomes a function only of z and we can neglect the other two Jeans equations in R and θ. This equation has a simple solution for $\nu(z)$:

$$\frac{\nu(z)}{\nu(z_0)}=\frac{\sigma_z^2(z_0)}{\sigma_z^2(z)}\exp\left(-\int_{z_0}^{z}\frac{1}{\sigma_z^2(z)}\frac{d\Phi}{dz}dz\right). \tag{4.2}$$

In Chapter 2 we showed that, given the density $\rho_{{\rm s},j}(0)$ and the vertical velocity dispersion $\sigma_{z,j}^2(0)$ at the midplane for each of the gas and stellar populations in the local disc, we can model the full disc density distribution as a superposition of isothermal populations:

$$\rho_{\rm s}(z)=\sum_j\rho_{{\rm s},j}(0)\exp\left(-\frac{\Phi(z)}{\sigma_{z,j}^2(0)}\right). \tag{4.3}$$

In this way, we can write the Poisson equation in cylindrical coordinates as:

$$\frac{\partial^2\Phi}{\partial z^2}=4\pi G(\rho_{\rm s}(z)+\rho_{\rm dm}^{\rm eff}) \tag{4.4}$$

with:

$$\rho_{\rm dm}^{\rm eff}=\rho_{\rm dm}(R)-(4\pi GR)^{-1}\frac{\partial}{\partial R}V_c^2(R) \tag{4.5}$$

where $\rho_{\rm dm}(R)$ is the halo mass density (following assumption 2, this is assumed to be independent of z in the volume considered); and $V_c(R)=(R\partial\Phi/\partial R)^{1/2}$ is the (total) circular velocity at a distance R (in the plane) from the centre of the Galaxy.

We solve equations 4.3 and 4.4 numerically for a given tracer population, adopting the following procedure:

1. We make initial trial guesses for $\rho_{{\rm s},j}(0)$, $\rho_{\rm dm}$, and the vertical velocity dispersion for the visible matter component in the plane $\sigma_{z,j}^2(0)$.

2. We solve equation 4.3 to obtain $\Phi(z)$ and its first derivative $\frac{\partial\Phi}{\partial z}$, with $\Phi(0) = \frac{\partial\Phi}{\partial z}\Big|_0 = 0$.
3. We insert this result into equation 4.2 for the vertical density profile of the tracers $\nu_{\rm p}(z)$ and compare this with the observed distribution $\nu(z)$ to obtain a goodness of fit.

This procedure requires many input parameters, such as the normalisations and dispersions of each of the disc components, and the vertical dispersion profile of the tracers (typically poorly constrained). To explore the parameter space and marginalise over the uncertainties, we use a Monte Carlo Markov Chain (MCMC) method.

4.3 Testing the method on N-body simulations

When we consider stellar tracers at large radii in the Galactic disc, the hypothesis 1 of Section 4.2 could not be fulfilled because of the presence of asymmetric non-equilibrium features such as warps and flares in the outer regions of the disc. For this reason, before applying the MA method to data at large radii in the Galactic, we test the possible effect of these non-equilibrium features on the method, using numerical simulations as mock data sets. The simulations are also used to predict the density distribution at different radii when a dark disc is present.

4.3.1 The simulations

We run two high resolution N-body simulation of mergers between a Milky Way like galaxy (the Milky Way like disc described in Section 2.3) and a satellite galaxy (namely LLMC described in Read et al., 2008), with two different orbit inclinations: a high inclination merger (60° with respect to the main galaxy's disc plane, simulation LLMC60) and a low inclination merger (10°, simulation LLMC10). Both simulations were run with the parallel tree code PKDGRAV (Stadel, 2001). The features of the galaxy models and of the satellites' orbits are reported in Tables 4.1 and 4.2.

The initial Milky Way like disc (MW), before the merger, is thin and symmetric (see upper panel of figure 4.1, the stellar disc is shown in red, while the dark matter halo is in black). Then we merge this initial disc with a satellite galaxy

Table 4.1: Simulation parameters for the Milky Way like galaxy (MW) and the satellite (LLMC). The columns show from left to right: the number of star and dark matter particles (N_* and $N_{\rm DM}$); the force softenings (ϵ_* and $\epsilon_{\rm DM}$); and the masses of each component (M_* and $M_{\rm DM}$). Where two force softenings are given, these are for the low mass inner and higher mass outer halo particles.

Galaxy model	N_* $[10^6]$	$N_{\rm DM}$ $[10^6]$	ϵ_* [kpc]	$\epsilon_{\rm DM}$ [kpc]	M_* $[10^{10}\,{\rm M}_\odot]$	$M_{\rm DM}$ $[10^{10}\,{\rm M}_\odot]$
MW	30.5	15	0.015	0.045	6	45.4
LLMC	0.75	2	0.015	0.024; 0.234	0.3	10

Table 4.2: The initial satellite orbits for the low (LLMC10) and the high (LLMC60) inclination simulations. The columns give from left-to-right-hand side: the initial phase space coordinates of the satellite (x, y, z and v_x, v_y, v_z); the initial inclination to the Milky Way disc (i); and the eccentricity (e) of the orbits.

Simulation	(x, y, z) [kpc]	(v_x, v_y, v_z) [km/s]	i	e
LLMC10	(29.5, 0.27,-5.2)	(-6.3, 89.3, 0.35)	10°	0.8
LLMC60	(15, 0.12, -26)	(-1.2, 80.1, 2.0)	60°	0.8

(LLMC) at different orbit inclinations and evolve the simulation for $\sim 4\,$Gyr. As expected in the case of the low inclination merger (LLMC10 simulation), the satellite's dark matter is dragged to the disc plane by dynamical friction and a dark disc is formed (see middle panel of figure 4.1, the dark disc is shown in blue), while the stellar disc (in red) is heated and becomes thicker. When the orbit of the accreting satellite is nearly perpendicular to the disc plane, as for the high inclination merger simulation (LLMC60), the stellar disc is not only heated, but also damaged and distorted, becoming less symmetric (see lower panel of figure 4.1, red line). In this case the dark disc is not visible and the accreted dark matter has a nearly spherical distribution (blue line).

Notice that the stellar disc no longer resembles the Milky Way thin disc. No gas has been included in our pure N-body simulations, so it could not cool and re-form a thin disc after the merger. For this reason it is not worth evaluating the effect of multiple mergers with N-body simulations: a second satellite merging afterwards would undergo a weaker dragging effect of this heated thick disc, forming a much weaker dark disc.

Furthermore, the presence of the accreted baryonic disc causes the halo of

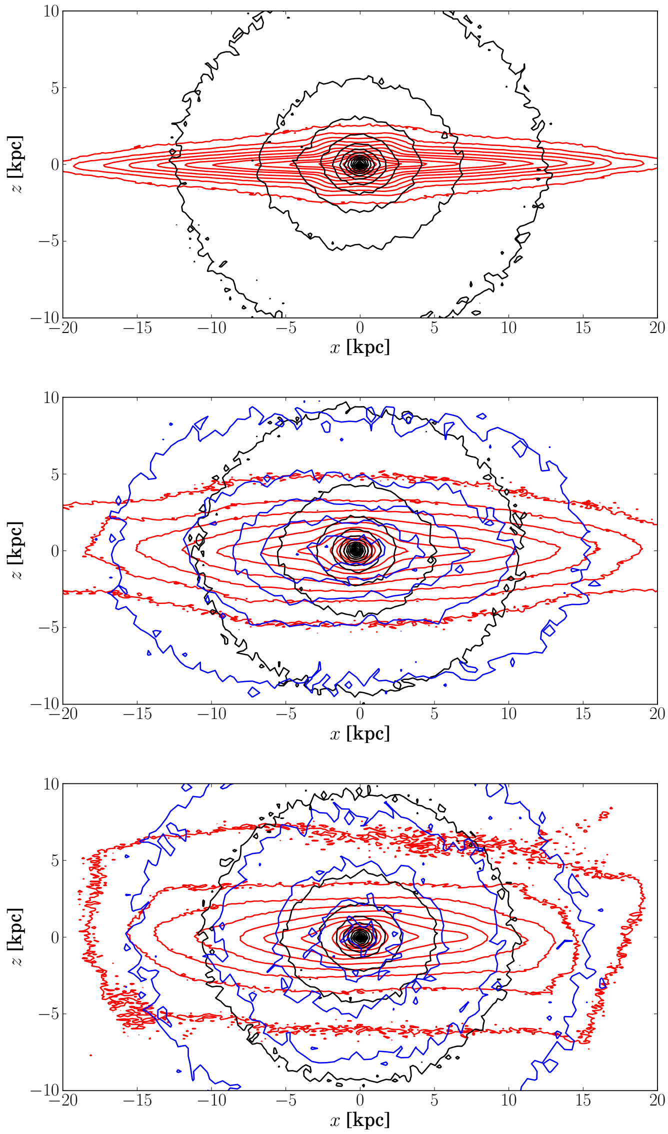

Figure 4.1: The disc of the galaxy in the simulations seen edge on (x-z plane). The black and red lines are the iso-density contours for the dark matter (of the Milky Way like galaxy only) and star (Milky Way like galaxy + accreted) particles, respectively. The blue line represents the distribution of the accreted dark matter particles *Upper panel:* the disc of the Milky Way like galaxy before the merger (MW simulation). The stellar disc looks thin and the dark matter distribution is nearly spherical. *Middle panel:* The disc of the simulated Galaxy at the end of the low inclination merger (LLMC10). After the merger the stellar disc looks thicker and the accreted dark matter distribution close to the plane is flattened (the dark disc). *Lower panel:* The disc of the galaxy at the end of the high inclination merger (LLMC60). After the high inclination merger the disc of the galaxy is damaged: it becomes thicker and distorted.

the main galaxy to become more oblate. In figure 4.2 the comparison between the average dark matter density in spherical shells (in blue) and in cylindrical bins on the disc plane (in red) at different radii is shown. The difference between the blue and the red curve owes to the oblateness of the dark matter halo: if it were perfectly spherical symmetric, the two lines would have overlapped. Notice that in the case of the low inclination merger this difference is even larger in the central bins: this reflects the additional presence of the dark disc. We can appreciate this better in figure 4.3, where the midplane dark matter density, calculated from particles initially belonging to the main galaxy (in purple) and from accreted particles (in orange), is shown. For the low inclination simulation we can see a contribution of the accreted dark matter density at the solar position ($R_\odot \simeq 8.5\,\mathrm{kpc}$) of about one third of the halo density (upper panel of 4.3, purple line). The contribution to the dark matter density at the Sun position from the accreted satellite in the high inclination merger is much lower (lower panel of 4.3, purple line).

4.3.2 Measuring the dark matter density at large radii

We now apply the MA method to the two simulations to test how well this technique performs in presence of asymmetric non-equilibrium features in the outer disc (as in LLMC60) and a dark disc (as in LLMC10).

For each simulation, we consider four different azimuthal angles around the disc at a distance of 90° from each other; for each angular position we take into consideration three different volumes at galactocentric distances of 8.5, 10.5 and 12.5 kpc. Each volume has a wedge shape with a radial size of 0.25 kpc and is about 1 kpc wide; we fit the density fall-off of the tracers up to 0.75 kpc.

The mass model for the visible matter is made of a single isothermal components, whose midplane density and velocity dispersion are measured from the simulations. In the MCMC, we let the local dark matter density vary in the range $[0, 0.5]\,\mathrm{M_\odot\,pc^{-3}}$ and the visible mass density on the midplane $\rho_{\mathrm{s}}(0)$ vary in the range $\pm 0.014\,\mathrm{M_\odot\,pc^{-3}}$ around the actual value measured for the simulation. This range for the visible matter density has been chosen to match the current observational uncertainties on ρ_{s} in the Solar vicinity.

As we did in Chapter 3 (and in Garbari et al., 2012), we should apply the same kind of position and velocity uncertainties, present in the real data, to the

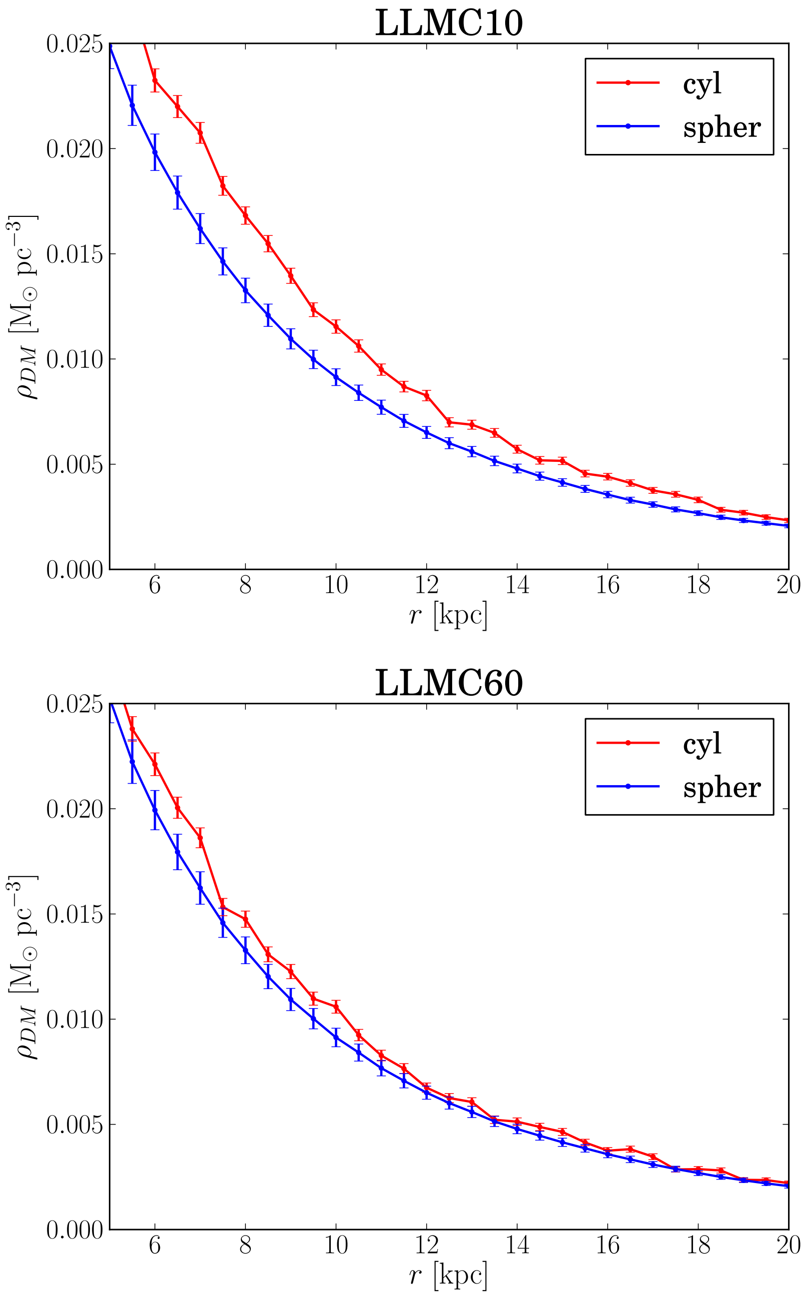

Figure 4.2: The average density of dark matter in spherical shells (in blue) and in cylindrical bins in the disc plane (in red) at different galactocentric radii. The *upper panel* refers to the low inclination merger simulation (LLMC10) and the *lower panel* to the high inclination one (LLMC60). The error bars represent Poisson errors.

simulated galaxies, to test the performance of the method. Since the analysis of the Red Clump data has not been completed, we test the method assuming 10%

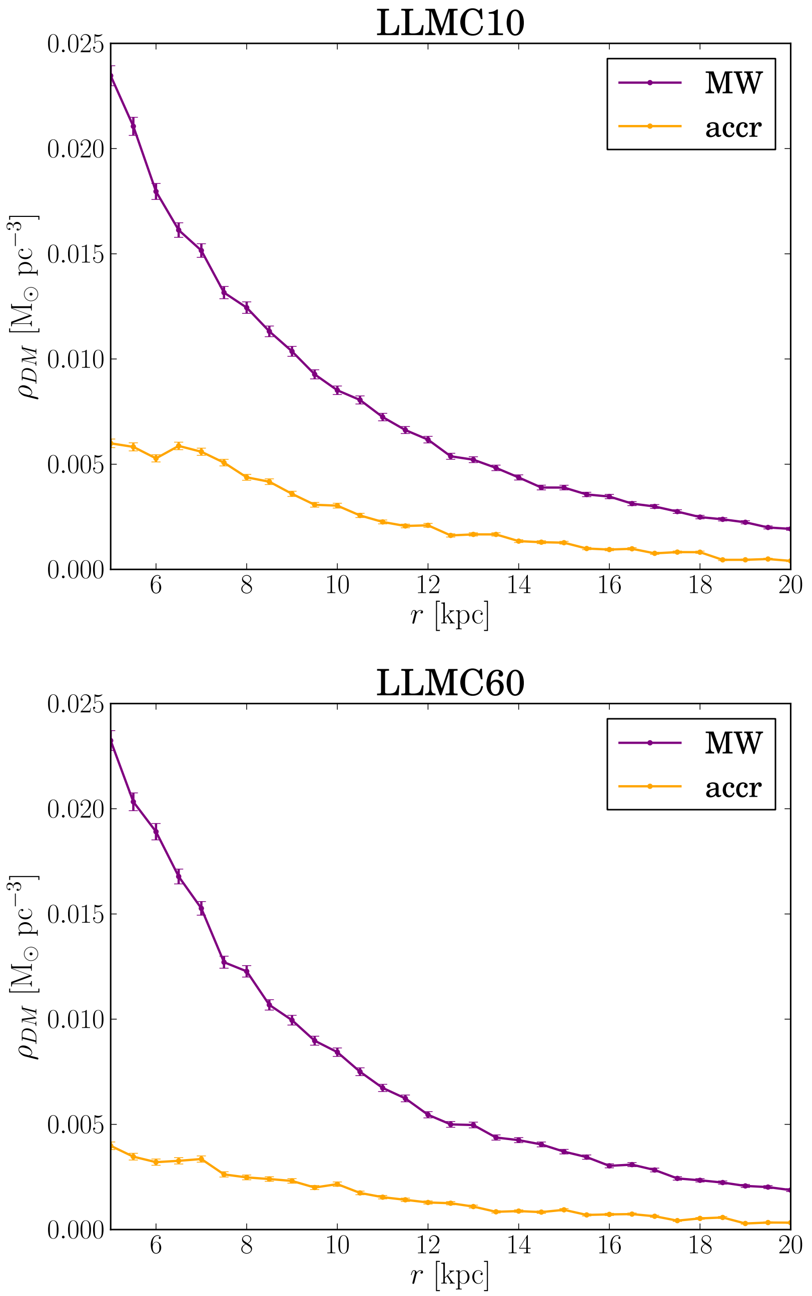

Figure 4.3: The average midplane density of dark matter at different galactocentric radii, calculated from particles initially belonging to the main galaxy (in purple) and accreted particles (in orange). The *upper panel* refers to the low inclination merger simulation (LLMC10) and the *lower panel* to the high inclination one (LLMC60). The error bars represent Poisson errors.

errors on both the velocity dispersion and the density fall-off of the tracers. To account for these errors, at each iteration of the MCMC, we sample a different realisation of $\sigma_z(z)$ and $\nu(z)$ for each z-bin, from a Gaussian distribution centred in the average profiles and with width corresponding to 10% errors. Notice that the quality of data we have for the Red Clump stars will not allow us to sample the velocity and position errors for each single star, as we did for the K dwarfs in Garbari et al. (2012).

The results for the low and high inclination merger simulations at different Galactocentric radii are shown in middle and lower panels of figure 4.4. For a comparison, in the upper panels of figure 4.4 we show the performance of the method for the isolated Milky Way like disc (simulation MW). The plots refer to a particular angular position in the disc for each simulation: the MCMC chain is still running for most of the other volumes. In these plots the crosses represent the true value of the stellar and dark matter density in the midplane for each volume (with Poisson error bars). The red and blue data points represent the median of the model distribution explored by the MCMC for $\rho_{\rm s}$ and $\rho_{\rm dm}$, with 90% and 68% confidence intervals error bars. Notice that the dark matter density contribution is higher for the LLMC10 simulation, especially at lower radii, due to the presence of the dark disc. The much lower stellar density in the two merger simulations looks unrealistic and owes to the heating of the disc after the mergers; as mentioned earlier, this is an effect of the lack of gas in these N-body simulations that prevents a new thin disc to be formed from cooling.

In almost all the cases the MA method recovers the correct value of $\rho_{\rm s}$ and $\rho_{\rm dm}$ inside the 90% confidence intervals. Only in the most external radius explored for the LLMC10 simulation, the result is at tension with the correct value of $\rho_{\rm dm}$. However we expect the method to fail in recovering the correct answer occasionally due to statistical fluctuations: in fact with 90% confidence interval, the method should “fail” on average one time in ten. When we will have the results for the other volumes, this will boost our statistics, so we will be able to understand if this failure is related to some feature at large radii or just statistical fluctuations. Furthermore the number of MCMC iterations for this particular volume is still much lower than for all the others and we do not know whether the results for it have converged: we will present the full analysis of the simulation in future work.

From these preliminary tests we see that the error bars we obtain are much larger than the difference between $\rho_{\rm dm}$ in presence of a dark disc and without, at a given radius. However for the LLMC10 simulation we recover steeply decreasing values of $\rho_{\rm dm}$ with increasing R: this does not happen for the LLMC60 simulation and is less evident for the isolated Galaxy. If this is observed for the other volumes, it would mean that the method can detect the change of $\rho_{\rm dm}$ with R, when the dark disc is present. The analysis of volumes at $R < R_\odot$ could enhance this effect, since in those regions the dark disc can contribute more to $\rho_{\rm dm}$. Furthermore, the LLMC10 simulation includes just one merger with a satellite galaxy, however we expect the Milky Way to undergo several such events during its evolution: the superposition of the effects of more mergers could create a larger dark disc in the Milky Way.

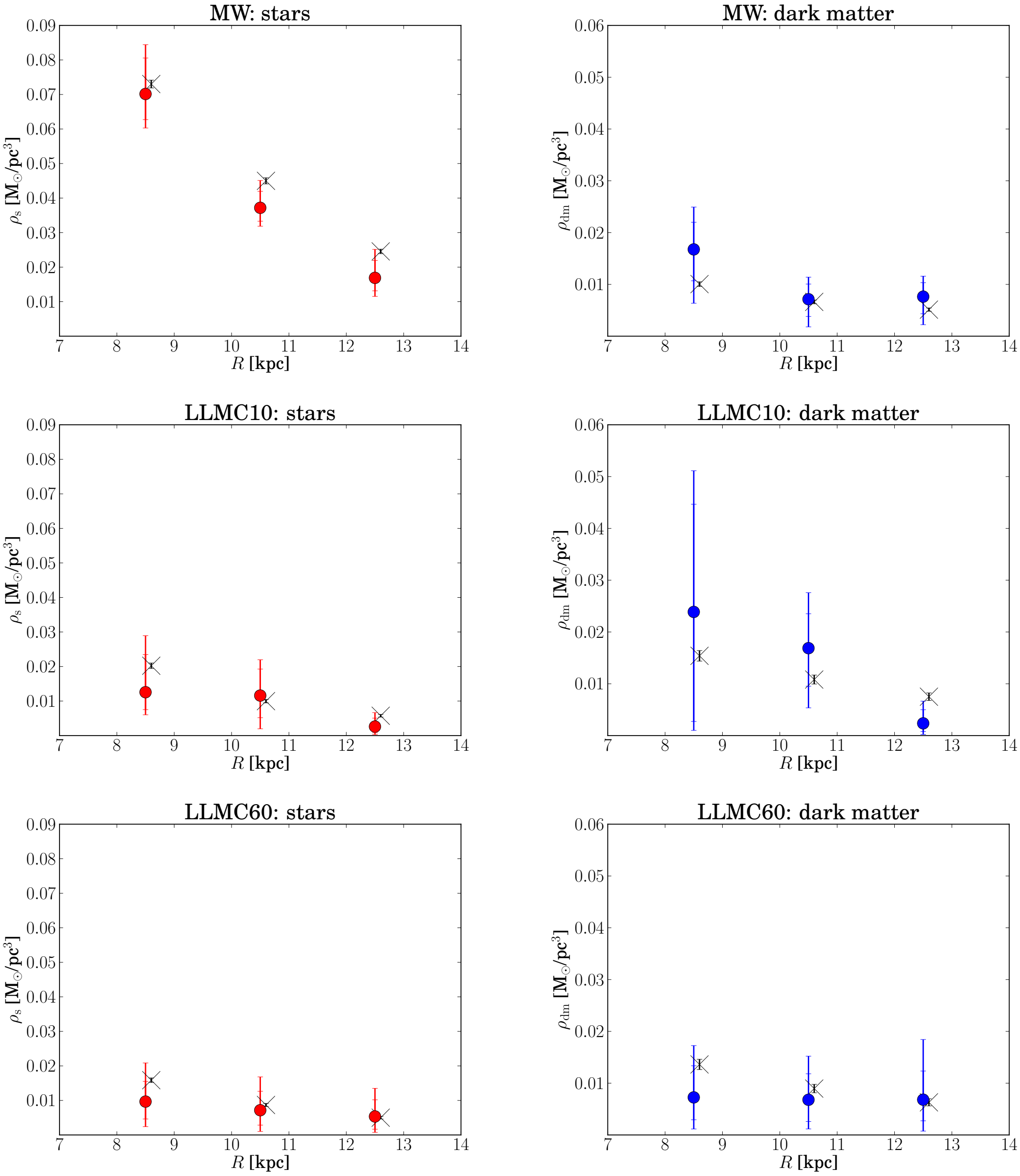

Figure 4.4: The results of the MA method for the isolated Milky Way like disc (*upper panels*) and for the two merger simulation LLMC10 (*middle panels*) and LLMC60 (*lower panels*), at different radial positions, namely $R = 8.5$, 10.5 and 12.5 kpc. The left (right) panels refer to the stellar (dark matter) density. The data points represent the median of the MCMC models distribution with 68% and 90% confidence intervals error bars. The crosses represent the actual values of the stellar (dark matter) density in the midplane, with Poisson error bars.

4.4 The data

To map the dark matter density as a function of radius in the disc of the Milky Way, we need a sample of stars that are well mixed with the potential and have distance and velocity determinations. We choose the Red Clump stars from the PPMXL catalogue (Roeser et al., 2010); this catalogue is a combination of proper motion data from the USNO-B1.0 (Monet et al., 2003) and accurate astrometric positions from the Two Micron All Sky Survey (2MASS, Skrutskie et al., 2006).

The Red Clump stars are the metal rich equivalent of the Horizontal Branch stars, and theoretical models predict that their absolute luminosity depends weakly on their age and chemical composition.

This class of stars matches our needs: a) they are old (metal-rich) stars located around the whole disc; b) they have good distance estimates; c) they are bright giants and extend far away in the disc, so they can be observed at a broad range of Galactocentric radii; d) the extinction along their line of sight is easily determined.

Although Red Clumps are relatively easy to recognise in the color-magnitude diagram (see figure 4.5), it is non trivial to distinguish them individually from other stars. The main contaminants are the K dwarfs around the Sun. If a K dwarf is classified as a Red Clump star, it would be assigned a distance that is 25 times larger than its true vale. The contamination is more signicant for faint stars than for bright stars. Consequently, the stellar density could be much more biased at large distances than closer to the Sun. Hence, it is critical to purify the giant samples before measuring the stellar density.

The analysis of the samples is in progress, therefore we defer to future work the determination of the density profile and of the velocity dispersion of the Red Clump stars and the application of the MA method to these samples.

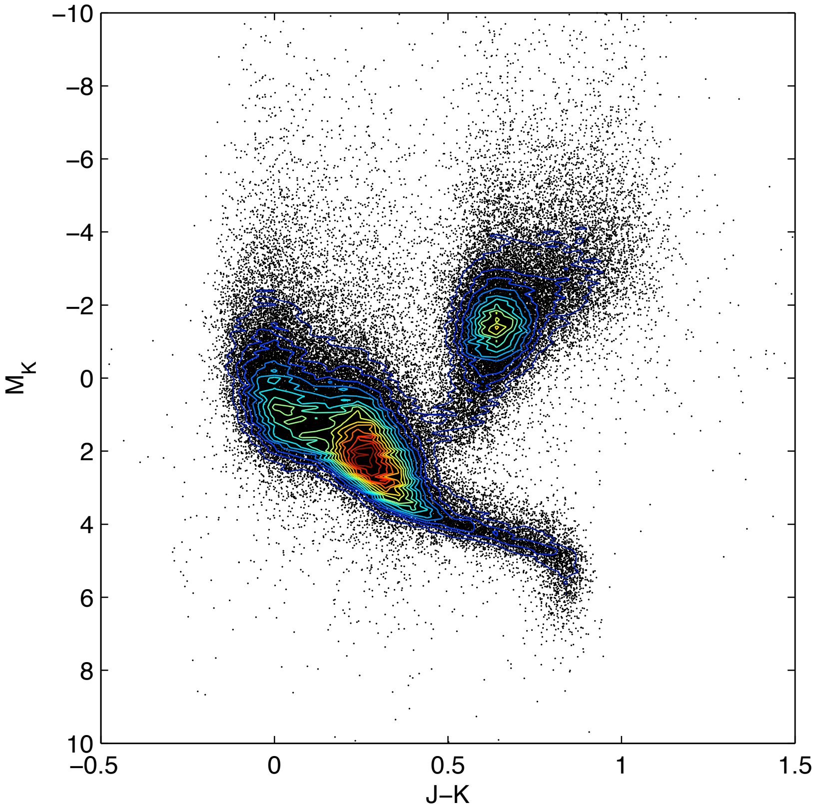

Figure 4.5: Colour-magnitude diagram in $(J-K)_0 - M_K$ for 2MASS stars cross matched with *Hipparcos* in order to obtain the absolute magnitude. The red clump is very easy to identify on the right side.

4.5 Summary and conclusions

This project aims to provide a first map of the density of dark matter in the disc of the Milky Way to measure the distribution of dark matter and probe the presence of a dark disc (Lake, 1989; Read et al., 2008; Read et al., 2009). We apply the MA method (Garbari et al., 2011, 2012) to stellar tracers at different Galactocentric radii. We choose Red Clump stars, since they are bright, are seen at large distances from the Sun and have good distance estimates. The analysis of the data is still ongoing and the result from this part of the project will be presented in future works.

Before applying the MA method to real data, we test its performance on mock data sets. For this purpose, we ran two high resolution simulation of a Milky Way like galaxy merging with a satellite at two different inclinations (namely 10° and 60° with respect to the Galactic disc). In the high inclination case, the disc of the main Galaxy becomes thicker and presents non-equilibrium features such as warps and flares. We use this simulation to test the performance of the MA method in the presence of non-equilibrium features. In the low inclination merger, both the accreted stars and dark matter particles are dragged into the disc plane by dynamical friction. In this case, the stellar disc is heated and a thick dark disc is formed. We use this second simulation to understand whether the method can detect such a dark disc. The preliminary results are:

- the MA method recovers the correct visible and dark matter density even if face of non-equilibrium features in the outer disc, such as warp and flares.
- even if the uncertainties are comparable to the difference in ρ_{dm} at a given radius, the method is sensitive to the steeper decrease of ρ_{dm} when a dark disc is present (see left panels of figure 4.4). If this will be confirmed by the analysis of the other volumes in the simulation, it would imply that the method can detect the dark disc, even if its contribution to the dark matter density is low. Data from the inner disc will be analysed: in fact at these radial positions the contribution of the dark disc is expected to be much larger. Finally the Galaxy underwent several mergers during its evolution, so we expect a larger contribution from the dark disc than the one created in our simulation.

The next steps are: i) the full analysis of the simulations, introducing more realistic observational errors, and different volumes around the disc plane to increase the statistics; ii) the completing of the data analysis to determine the velocity dispersion and density profile of the Red Clump stars at different Galactocentric positions and the application of the MA method to these data.

Chapter 5

Conclusions

This thesis focuses on the determination of the dark matter density – $\rho_{\rm dm}$ – in the disc of our Galaxy, through the kinematics of stellar tracers. The measurement of $\rho_{\rm dm}$ and of the matter surface density in the Milky Way disc is a hot current topic.

Future surveys will provide accurate velocity and position measurements for a very large number of stars in our Galaxy, so the systematic errors will dominate. Hence, I studied the systematic problems in determining $\rho_{\rm dm}$ from solar neighbourhood stars (Chapter 2, Garbari et al., 2011). My approach used a high resolution N-body simulation of an isolated Milky Way-like galaxy as a mock data set. I examined a popular class of methods in the literature based on the distribution function of stars. To measure the local dark matter density, we must study the vertical motion of the stellar tracers up to a height of about 2-3 times the Galactic disc scale height. I found that realistic mixing of stars owing to the formation of a bar and spiral arms (as seen in our Galaxy) breaks a key assumption that the distribution function is separable. This leads to a systematic bias in the recovery of $\rho_{\rm dm}$, when separability is assumed. I then introduced a new method based on moments of the Jeans equations. This method relies on a Minimal set of Assumptions (the "MA" method), combined with a Monte Carlo Markov Chain technique to marginalise over unknown parameters and observational uncertainties on the velocities and positions of the stars. Given sufficiently good data (in particular a good measure of the vertical velocity dispersion as a function of z for the tracer population), I showed that the MA method can recover the correct local dark matter density despite the effect of disc inhomogeneities, non-isothermal tracers and a non-separable distribution function.

I then applied the MA method to data in the literature (Chapter 3, Garbari et al., 2012), recalibrating the stellar distances for these stars with magnitude-metallicity distribution functions from modern surveys. In addition, I determined how additional complications (such as asymmetric distance errors and velocity errors) influence the final result, adding problems that are present in the real data to our mock data, and marginalising over the observational uncertainties. The application of the MA method to the K dwarf data with the improved distance determination leads to a large value of the local dark matter density of $\rho_{\rm dm} = 0.022^{+0.015}_{-0.013}\ {\rm M_{\odot}pc^{-3}}$ ($0.85^{+0.57}_{-0.50}\,{\rm GeV\,cm^{-3}}$) at 90% confidence level. This value is larger than the canonical value and mildly in tension with extrapolations from the rotation curve that assume a spherical halo. Despite the large error bars, this new value for $\rho_{\rm dm}$, if confirmed by better data, has interesting implications. It would mean a larger flux of dark matter particles and therefore a greater chance of detection. Also it means that either the halo of our Galaxy is oblate and/or that there is a disc of dark matter in the Galaxy, as predicted by recent cosmological simulations (Read et al., 2008; Read et al., 2009). Other dynamical tracers in the Milky Way may support this. Loebman et al. (2012) have recently estimated the Milky Way halo shape out to $\sim 20\,{\rm kpc}$ for the Galactic centre using reconstructed SDSS data fit with the axisymmetric Jeans equations, finding evidence for a very flattened dark matter halo locally. An oblate halo is also consistent – although not required – with the globular cluster stream NGC 5466, probing a similar region of the Milky Way potential (Lux et al., 2012). However, a flattened halo near the disc might be at tension with recent measurements from SDSS data by Zhang et al. (2012), finding $\rho_{\rm dm} = 0.0065 \pm 0.0023\ {\rm M_{\odot}pc^{-3}}$.

Finally I presented an ongoing project (Chapter 4) – in collaboration with David Von Rickenbach, Justin Read and Chao Liu – to map the dark matter density at different radial positions in the disc, for the first time. This project will probe the structure of the Milky Way and its formation, by comparing these results with the predictions from simulations, in particular probing the existence of an accreted disc of dark matter. We used N-body simulations to generate mock data sets that test the performance of the MA method at large R and study the detectability of a dark matter disc. In particular I ran two high resolution N-body simulations of mergers between a Milky Way like galaxy and a satellite galaxy, with two different orbit inclinations: i) a high inclination merger which strongly damage the Milky Way disc, creating non-equilibrium features such as flares and warps; and ii) a low inclination merger. The analysis of the first simulation allows us to determine how the presence of these structures in our Galaxy affects the method. The second simulation is used to understand whether the MA method can detect a dark disc and how its density is predicted to change as a function of radius. Then I presented a suitable sample of tracers that will be analysed to map $\rho_{\rm dm}(R)$. We chose Red Clump stars from the the PPMXL catalogue (Roeser et al., 2010), extending out to $R \sim 13\,\rm kpc$ from the Galactic centre, as they have distance estimates. The preliminary analysis of the simulations indicates that the MA method can recover the dark matter density in the Galactic even at larger radii, where the disc is more affected by the presence of non-equilibrium features (flares and warps) and is able to detect the presence of a dark disc, even if its contribution to the dark matter density in the disc is low. The next steps are: i) the completing of the data analysis to determine the velocity dispersion and density profile of the Red Clump stars and the application of the MA method to the data. ii) Once the analysis of the data will be completed, we will apply more realistic errors to the simulated data too and include different volumes around the disc plane to increase our statistics.

Glossary

Symbols and units

Symbol	**Value**	**Description**
pc	$3.08568025 \times 10^{16}\,\mathrm{m}$	parsec
G	$6.674 \times 10^{-8}\,\mathrm{cm^3 g^{-1} s^{-2}}$	Gravitational constant
$\mathrm{M}_\odot$	$1.9891 \times 10^{30}\,\mathrm{kg}$	Solar mass
$R_\odot$	$\sim 8 - 8.5\,\mathrm{kpc}$	Galactocentric distance of the Sun

Notations

Vectors are represented by bold symbols, e.g. $\mathbf{F}$; scalars are represented by italic symbols, e.g. m.

Time derivatives are indicated with a dot, e.g. $\frac{da}{dt} = \dot{a}$ and $\frac{d^2a}{dt^2} = \ddot{a}$.

Bibliography

Aaronson M., 1983, ApJL, 266, L11

Abazajian K. N., Adelman-McCarthy J. K., Agüeros M. A., Allam S. S., Allende Prieto C., An D., Anderson K. S. J., Anderson S. F., Annis J., Bahcall N. A., et al. 2009, ApJS, 182, 543

Aguirre A., Schaye J., Quataert E., 2001, ApJ, 561, 550

Aprile E., Giboni K. L., Majewski e. a., 2005, New Astronomy Reviews, 49, 289

Baer H., Brhlik M., 1998, Phys. Rev. D, 57, 567

Bahcall J. N., 1984a, ApJ, 276, 156

Bahcall J. N., 1984b, ApJ, 287, 926

Bahcall J. N., 1984c, ApJ, 276, 169

Bahcall J. N., Flynn C., Gould A., 1992, ApJ, 389, 234

Bahcall J. N., Sarazin C. L., 1977, ApJL, 213, L99

Bailer-Jones C. A. L., 2009, in Andersen J., Bland-Hawthorn J., Nordström B., eds, IAU Symposium Vol. 254 of IAU Symposium, “what will gaia tell us about the galactic disk?”. pp 475–482

Bailin D., Love A., 1994, Supersymmetric gauge field theory and string theory. Graduate student series in physics, Institute of Physics Pub.

Bailin J., Kawata D., Gibson B. K., Steinmetz M., Navarro J. F., Brook C. B., Gill S. P. D., Ibata R. A., Knebe A., Lewis G. F., Okamoto T., 2005, ApJL, 627, L17

Baudis L., 2006, International Journal of Modern Physics A, 21, 1925

Baudis L., Klapdor-Kleingrothaus H. V., 2000, ArXiv Astrophysics e-prints

Beers T. C., Flynn K., Gebhardt K., 1990, AJ, 100, 32

Belokurov V., Zucker D. B., Evans N. W., Wilkinson M. I., Irwin M. J., Hodgkin S., Bramich D. M., Irwin J. M., Gilmore G., Willman B., Vidrih S., Newberg H. J., Wyse R. F. G., Fellhauer M., Hewett e. a., 2006, ApJL, 647, L111

Bernabei R., Belli P., Cappella F., Cerulli R., Dai C. J., D'Angelo A., He H. L., Incicchitti A., Kuang H. H., Ma J. M., Montecchia F., Nozzoli F., Prosperi D., Sheng X. D., Ye Z. P., 2008, European Physical Journal C, 56, 333

Bienayme O., Robin A. C., Creze M., 1987, A&A, 180, 94

Binney J., Merrifield M., 1998, Galactic Astronomy

Binney J., Tremaine S., 2008, Galactic Dynamics: Second Edition. Princeton Univ. Press, Princeton, NJ

Bond N. A., Ivezić Ž., Sesar B., Jurić M., Munn J. A., Kowalski A., Loebman S., et al 2010, ApJ, 716, 1

Borriello A., Salucci P., 2001, MNRAS, 323, 285

Bourassa R. R., Kantowski R., 1975, ApJ, 195, 13

Bovy J., Rix H.-W., Hogg D. W., 2012, ApJ, 751, 131

Bovy J., Tremaine S., 2012, arXiv:1205.4033

Boyarsky A., Ruchayskiy O., Shaposhnikov M., 2009, Annual Review of Nuclear and Particle Science, 59, 191

Branham Jr. R. L., 2010, MNRAS, 409, 1269

Bruch T., Peter A. H. G., Read J., Baudis L., Lake G., 2009, Physics Letters B

Bruch T., Read J., Baudis L., Lake G., 2009, ApJ, 696, 920

Carr J., Lamanna G., Lavalle J., 2006, Reports on Progress in Physics, 69, 2475

Casagrande L., Flynn C., Portinari L., Girardi L., Jimenez R., 2007, MNRAS, 382, 1516

Catena R., Ullio P., 2010, Journal of Cosmology and Astroparticle Physics, 8, 4

CDMS Collaboration 2009, Physical Review Letters, 102, 011301

Chwolson O., 1924, Astronomische Nachrichten, 221, 329

Clowe D., Bradač M., Gonzalez A. H., Markevitch M., Randall S. W., Jones C., Zaritsky D., 2006, ApJl, 648, L109

Clowe D., Randall S. W., Markevitch M., 2007, Nuclear Physics B Proceedings Supplements, 173, 28

Cole S., Percival W. J., Peacock J. A., Norberg P., Baugh C. M., Frenk C. S., Baldry I., Bland-Hawthorn J., Bridges T., et al 2005, MNRAS, 362, 505

Crézé M., Chereul E., Bienayme O., Pichon C., 1998, A&A, 329, 920

de Blok W. J. G., McGaugh S. S., Bosma A., Rubin V. C., 2001, ApJL, 552, L23

Debattista V. P., Moore B., Quinn T., Kazantzidis S., Maas R., Mayer L., Read J., Stadel J., 2008, ApJ, 681, 1076

Dehnen W., 2002, in E. Athanassoula, A. Bosma, & R. Mujica ed., Disks of Galaxies: Kinematics, Dynamics and Peturbations Vol. 275 of Astronomical Society of the Pacific Conference Series, Our Galaxy. pp 105–116

Dehnen W., Binney J., 1998, MNRAS, 294, 429

Drimmel R., Spergel D. N., 2001, ApJ, 556, 181

Dubinski J., 1994, ApJ, 431, 617

Dubinski J., Carlberg R. G., 1991, ApJ, 378, 496

Duffy L. D., van Bibber K., 2009, New Journal of Physics, 11, 105008

Einstein A., 1936, Science, 84, 506

Ettori S., Gastaldello F., Leccardi A., Molendi S., Rossetti M., Buote D., Meneghetti M., 2010, A&A, 524, A68

Feast M., 2000, MNRAS, 313, 596

Ferrière K. M., 2001, Reviews of Modern Physics, 73, 1031

Flynn C., Freeman K. C., 1993, A&AS, 97, 835

Flynn C., Fuchs B., 1994, MNRAS, 270, 471

Flynn C., Holmberg J., Portinari L., Fuchs B., Jahrei H., 2006, MNRAS, 372, 1149

Freeman K. C., 1970, ApJ, 160, 811

Fuchs B., Wielen R., 1993, in S. S. Holt & F. Verter ed., Back to the Galaxy Vol. 278 of American Institute of Physics Conference Series, Kinematical constraints on the dynamically determined local mass density of the Galaxy. pp 580–583

Gaitskell R. J., 2004, Annual Review of Nuclear and Particle Science, 54, 315

Garbari S., Liu C., Read J. I., Lake G., 2012, MNRAS, 425, 1445 (Paper II)

Garbari S., Read J. I., Lake G., 2011, MNRAS, 416, 2318 (Paper I)

Gates E., Gyuk G., Turner M., 1995, ApJl, 449, L123

Gates E. I., Gyuk G., Turner M. S., 1995, Physical Review Letters, 74, 3724

Geha M., Willman B., Simon J. D., Strigari L. E., Kirby E. N., Law D. R., Strader J., 2009, ApJ, 692, 1464

Gingold R. A., Monaghan J. J., 1977, MNRAS, 181, 375

Gnedin N. Y., Hamilton A. J. S., 2002, MNRAS, 334, 107

Graff D. S., Freese K., 1996, ApJL, 456, L49

Guo Q., White S., Li C., Boylan-Kolchin M., 2010, MNRAS, 404, 1111

Helmi A., 2004, ApJL, 610, L97

Hoekstra H., Yee H. K. C., Gladders M. D., 2002, ApJ, 577, 595

Holmberg J., Flynn C., 2000, MNRAS, 313, 209

Holmberg J., Flynn C., 2004, MNRAS, 352, 440

Ibata R., Lewis G. F., Irwin M., Totten E., Quinn T., 2001, APJ, 551, 294

Iocco F., Pato M., Bertone G., Jetzer P., 2011, Journal of Cosmology and Astroparticle Physics, 11, 29

Jarosik N., Bennett C. L., Dunkley J., Gold B., Greason M. R., Halpern M., Hill R. S., Hinshaw G., Kogut A., Komatsu e. a., 2011, ApJS, 192, 14

Jing Y. P., Suto Y., 2002, ApJ, 574, 538

Jordan S., 2008, Astronomische Nachrichten, 329, 875

Jungman G., Kamionkowski M., Griest K., 1996, Physics Reports, 267, 195

Kazantzidis S., Kravtsov A. V., Zentner A. R., Allgood B., Nagai D., Moore B., 2004, ApJL, 611, L73

Klypin A., Zhao H., Somerville R. S., 2002, ApJ, 573, 597

Komatsu E. e. a., 2011, ApJs, 192, 18

Kotoneva E., Flynn C., Chiappini C., Matteucci F., 2002, MNRAS, 336, 879

Kuijken K., Gilmore G., 1989a, MNRAS, 239, 651

Kuijken K., Gilmore G., 1989b, MNRAS, 239, 571

Kuijken K., Gilmore G., 1989, MNRAS, 239, 605 (KG89II)

Kuijken K., Gilmore G., 1991, APJ letters, 367, L9 (KG91)

Lacey C. G., Ostriker J. P., 1985, ApJ, 299, 633

Lake G., 1989, AJ, 98, 1554

Lange A. E., Ade P. A., Bock J. J., Bond J. R., Borrill J., Boscaleri A., Coble K., Crill B. P., de Bernardis P., Farese P., Ferreira P., Ganga K., Giacometti M., Hivon E., et al H., 2001, Phys. Rev. D, 63, 042001

Law D. R., Majewski S. R., 2010, ApJ, 714, 229

Loebman S. R., Ivezic Z., Quinn T. R., Governato F., Brooks A. M., Christensen C. R., Juric M., 2012, ArXiv e-prints

Lucy L. B., 1977, AJ, 82, 1013

Lux H., Read J. I., Lake G., Johnston K. V., 2012, MNRAS, 424, L16

Macciò A. V., Dutton A. A., van den Bosch F. C., Moore B., Potter D., Stadel J., 2007, MNRAS, 378, 55

Maron J. L., Howes G. G., 2003, ApJ, 595, 564

Martin N. F., Ibata R. A., Chapman S. C., Irwin M., Lewis G. F., 2007, MNRAS, 380, 281

Mateo M. L., 1998, ARA&A, 36, 435

Mignard F., 2000, AaP, 354, 522

Milgrom M., 1983, ApJ, 270, 365

Moffat J. W., 2006, Journal of Cosmology and Astroparticle Physics, 3, 4

Monaghan J. J., 1992, ARA&A, 30, 543

Monet D. G., Levine S. E., Canzian B., Ables H. D., Bird A. R., Dahn C. C., Guetter H. H., Harris H. C., et al. H., 2003, AJ, 125, 984

Moni Bidin C., Carraro G., Méndez R. A., 2012, APJ, 747, 101

Moore B., Kazantzidis S., Diemand J., Stadel J., 2004, MNRAS, 354, 522

Ng Y. K., Bertelli G., Chiosi C., Bressan A., 1997, A&A, 324, 65

Ojha D. K., 2001, MNRAS, 322, 426

Oort J. H., 1932, Bulletin of the Astronomical Institutes of the Netherlands, 6, 249

Oort J. H., 1960, Bulletin of the Astronomical Institutes of the Netherlands, 15, 45

Peebles P. J. E., 1965, ApJ, 142, 1317

Penzias A. A., Wilson R. W., 1965, ApJ, 142, 419

Percival W. J., Reid B. A., Eisenstein D. J., Bahcall N. A., Budavari T., Frieman J. A., Fukugita M., Gunn J. E., Ivezić Ž., Knapp G. R., Kron R. G., et al 2010, MNRAS, 401, 2148

Peter A. H. G., 2011, Physics Reviews B, 83, 125029

Pham H., 1997, in Hipparcos - Venice '97 Vol. 402 of ESA Special Publication, Estimation of the Local Mass Density from an F-Star Sample Observed by HIPPARCOS. pp 559–562

Quinn P. J., Goodman J., 1986, ApJ, 309, 472

Quinn P. J., Hernquist L., Fullagar D. P., 1993, ApJ, 403, 74

Rasia E., Ettori S., Moscardini L., Mazzotta P., Borgani S., Dolag K., Tormen G., Cheng L. M., Diaferio A., 2006, MNRAS, 369, 2013

Read J. I., Lake G., Agertz O., Debattista V. P., 2008, MNRAS, 389, 1041

Read J. I., Mayer L., Brooks A. M., Governato F., Lake G., 2009, MNRAS, 397, 44

Refsdal S., 1964a, MNRAS, 128, 295

Refsdal S., 1964b, MNRAS, 128, 295

Roeser S., Demleitner M., Schilbach E., 2010, AJ, 139, 2440

Rosati P., Borgani S., Norman C., 2002, Annual Review of Astronomy and Astrophysics, 40, 539

Rubin V. C., Ford W. K. J., . Thonnard N., 1980, ApJ, 238, 471

Saha P., 2003, Principles of Data Analysis. Great Malvern: Cappella Archive

Sánchez-Salcedo F. J., Flynn C., Hidalgo-Gámez A. M., 2011, ApJL, 731, L35+

Sanders J., 2012, ArXiv e-prints

Schlegel D. J., Finkbeiner D. P., Davis M., 1998, APJ, 500, 525

Schneider P., 2006, in Meylan G., Jetzer P., North P., Schneider P., Kochanek C. S., Wambsganss J., eds, Saas-Fee Advanced Course 33: Gravitational Lensing: Strong, Weak and Micro Part 3: Weak gravitational lensing. pp 269–451

Seabroke G. M., Gilmore G., 2007, MNRAS, 380, 1348

Shafieloo A., Souradeep T., 2004, Phys. Rev. D, 70, 043523

Siebert A., Bienayme O., Binney J., Bland-Hawthorn J., Campbell R., Freeman K. C., Gibson B. K., Gilmore G., Grebel E. K., Helmi A., Munari U., Navarro J. F., Parker 2008, MNRAS, 391, 793

Simon J. D., Bolatto A. D., Leroy A., Blitz L., Gates E. L., 2005, ApJ, 621, 757

Simon J. D., Geha M., 2007, ApJ, 670, 313

Skrutskie M. F., Cutri R. M., Stiening R., Weinberg M. D., Schneider S., Carpenter J. M., Beichman C., Capps R. e. a., 2006, AJ, 131, 1163

Smith M. C., Whiteoak S. H., Evans N. W., 2012, ApJ, 746, 181

Smith M. C., Wyn Evans N., An J. H., 2009, ApJ, 698, 1110

Smoot G. F., Bennett C. L., Kogut A., Wright E. L., Aymon J., Boggess N. W., Cheng E. S., de Amici G., Gulkis S., Hauser M. G., et al 1992, ApJL, 396, L1

Sofue Y., Honma M., Omodaka T., 2009, Publications of the Astronomical Society of Japan, 61, 227

Soucail G., Fort B., Mellier Y., Picat J. P., 1987, A&A, 172, L14

Spagna A., Lattanzi M. G., Lasker B. M., McLean B. J., Massone G., Lanteri L., 1996, A&A, 311, 758

Stäckel 1895, C. R. Acad. Sci. Paris, 121, 489

Stadel J. G., 2001, PhD thesis, University of Washington

Statler T. S., 1989, ApJ, 344, 217

Steinmetz M., 2003 Vol. 298, RAVE: the RAdial velocity experiment. p. 381

Steinmetz M., Zwitter T., Siebert A., Watson F. G., Freeman K. C., Munari U., 2006, AJ, 132, 1645

Tegmark M., Blanton M. R., Strauss M. A., Hoyle F., Schlegel D., Scoccimarro R., Vogeley M. S., Weinberg D. H., Zehavi I., SDSS Collaboration 2004, ApJ, 606, 702

Tegmark M., Zaldarriaga M., 2002, Phys. Rev. D, 66, 103508

Tisserand P., Le Guillou L., Afonso C., Albert J. N., Andersen J., Ansari R., Aubourg É., Bareyre P., Beaulieu J. P., Charlot X., Coutures C., Ferlet R., Fouqué P., EROS-2 Collaboration 2007, A&A, 469, 387

van Albada T. S., Bahcall J. N., Begeman K., Sancisi R., 1985, ApJ, 295, 305

Villumsen J. V., Freudling W., da Costa L. N., 1997, ApJ, 481, 578

Walker M. G., Mateo M., Olszewski E. W., Gnedin O. Y., Wang X., Sen B., Woodroofe M., 2007, ApJL, 667, L53

Walsh D., Carswell R. F., Weymann R. J., 1979, Nature, 279, 381

Weber M., de Boer W., 2010, A&A, 509, 25

Widrow L. M., Dubinski J., 2005, ApJ, 631, 838

Widrow L. M., Pym B., Dubinski J., 2008, ApJ, 679, 1239

Wilkinson M. I., Evans N. W., 1999, MNRAS, 310, 645

Willman B., Dalcanton J. J., Martinez-Delgado D., West A. A., Blanton M. R., Hogg D. W., Barentine J. C., Brewington H. J., Harvanek M., Kleinman S. J., Krzesinski J., Long D., Neilsen Jr. E. H., Nitta A., Snedden S. A., 2005, ApJL, 626, L85

Wyrzykowski L., Skowron J., Kozłowski S., Udalski A., Szymański M. K., Kubiak M., Pietrzyński G., Soszyński I., Szewczyk O., Ulaczyk K., Poleski R., Tisserand P., 2011, MNRAS, 416, 2949

Xue X. X., Rix H. W., Zhao G., Re Fiorentin P., Naab T., Steinmetz M., van den Bosch F. C., Beers T. C., Lee Y. S., Bell E. F., Rockosi C., Yanny B., Newberg H., Wilhelm R., Kang X., Smith M. C., Schneider D. P., 2008, 0801.1232

Yanny B., Rockosi C., Newberg H. J., Knapp G. R., et al. J. K., 2009, AJ, 137, 4377

Zhang L., 2012, in preparation (private communication).

Zhang L., Rix H.-W., van de Ven G., Bovy J., Liu C., Zhao G., 2012, ArXiv e-prints

Zucker D. B., Belokurov V., Evans N. W., Kleyna J. T., Irwin M. J., Wilkinson M. I., Fellhauer M., Bramich D. M., Gilmore G., Newberg H. J., Yanny B., Smith J. A., Hewett P. C. e. a., 2006, ApJL, 650, L41

Zwicky F., 1933, Helvetica Physica Acta, 6, 110

Zwicky F., 1937, ApJ, 86, 217

Zwitter T., Siebert A., Munari U., Freeman K. C., et al. A. S., 2008, AJ, 136, 421

Acknowledgements

I care to express my gratitude to Prof. George Lake and Prof. Justin Read for their precious guidance and support during my PhD. In particular, I thank Justin for all that he taught me, for his patience and interest in our projects, keeping my motivation always alive. And I thank George for the insightful discussions that always improved the quality of my work.

I would like to thank Prasenjit Saha, Jonathan Coles, Hanni Lux, Aaron Boley, Chao Liu, Chris Flynn, Alexander Hobbs, Pascal Steger and David Von Rickenbach, for useful discussions, important support and/or collaboration in my research work. Thanks to Regina and Rajni, for helping me with all the bureaucratic issues during these years.

I acknowledge all the people that shared my working days (and not only those) at the University of Zurich and at the ETH with me, and to the precious friends I met in Switzerland, in particular: Justin, Noelia, Liam, Javiera, Tania, Alex, Pascal, Andrea, Michiel, Maddalena, Hanni, Jonathan, Marina, Raymond, Simone, Lea, Geppina, Elisabetta, Cédric, Silvia, Michela, Valerio, Olga, Karen, Cloé... and I hope I did not forget anyone.

Finally I thank my family and the other important people, for being always close to me, even from distance: in particular my parents, Ruggero (and our little baby), Vera, Chiara, Lucio, Elisa, Francesca, Jessica.

Silvia GARBARI

Personal data

Date of birth : 11th January 1981
Place of birth : Milano, Italy
Nationality : Italian

Education

PhD at the University of Zurich:

Employed as PhD student since 2007
Thesis title: *Dark matter in the Milky Way Disc*
Supervisors: Prof. G. Lake, Prof. J. Read

Master Degree in Astronomy (Laurea Magistrale):

University of Padua (Italy): Oct 1999 - Oct 2006
Title of the thesis: *La Quintessenza Estesa e l'Evoluzione dell'Universo (Extended Quintessence)*
Supervisors: Prof. S. Matarrese, Prof. C. Baccigalupi, Prof. G. Tormen
Mark: 104/110

High School:

Liceo Scientifico G. Bruno, Melzo, Italy
Year of graduation: 1999
Leaving certificate: Maturità Scientifica (mark: 83/100)

Languages

Italian	Native language
English	Fluent
French	Basic
German	Basic

Teaching

WS 11	T.A. for “Mathematical methods for physicists I”, lecturer Prof. Ph. Jetzer
WS 09	T.A. for “Mathematical methods for physicists I”, lecturer Prof. Ph. Jetzer
SS 09	T.A. for “Mathematical methods for physicists II”, lecturer Prof. G. Lake
SS 08	T.A. for “Theoretical Cosmology”, lecturer Prof. U. Seljak
WS 07	T.A. for “Thermodynamics”, lecturer Prof. Dr. G. Blatter

Publications

Refereed publications

“A new determination of the local dark matter density from the kinematics of K dwarfs”, S. Garbari, C. Liu, J. I. Read, G. Lake, published in MNRAS, Volume 425, pp. 1445-1458 (2012).

“Limits on the local dark matter density”, S. Garbari, J. I. Read, G. Lake, published in MNRAS, Volume 416, Issue 3, pp. 2318-2340 (2011).

Non refereed publications

“Limits on the local dark matter density”, S. Garbari, J. I. Read, G. Lake, published in the proceedings of ”Assembling the Puzzle of the Milky Way”, Le Grand Bornand, France (April 17-22, 2011), C. Reylé, A. Robin, M. Schultheis (eds.), EPJ Web of Conferences, Volume 19, p. 1008.

“Measuring the local dark matter density”, S. Garbari, G. Lake, J. I. Read, published in AIP Conf. Proc. Volume 1240, pp. 411-412 HUNTING FOR THE DARK: THE HIDDEN SIDE OF GALAXY FORMATION.

Conferences

Talks

“Dark Matter in the Milky Way disc”, at the conference “Dark Attack” in Ascona, Switzerland, 15-19 July 2012.

“Limits on the Local Dark Matter Density”, at the “TEVPA Particle Astrophysics Conference” in Stockholm, Sweden, 4 August 2011.

“Limits on the Local Dark Matter Density”, Research Colloquium at ETH Zurich, Switzerland, 24 Feb. 2011.

“Measuring the local dark matter density through kinematics of stars”, at the workshop “Dark Matter in the Sky and Underground”, Zurich, Switzerland, 24 Sept. 2010.

“Local density of Dark Matter”, at the conference “The Milky Way and the Local Group - Now and in the Gaia Era” in Heidelberg, Germany, 4 Sept. 2009.

Posters

“Limits on the Local Density of Dark Matter”, S. Garbari, J. I. Read, G. Lake, conference “Assembling the puzzle of the Milky Way”, Le Grand Bornand, France, 18-22 Apr. 2011.

“Limits on the Local Density of Dark Matter”, S. Garbari, J. I. Read, G. Lake, conference “Hunting for the Dark: The Hidden Side of Galaxy Formation”, Malta, 19-23 Oct. 2009.

“Separating heated and accreted stars in the Milky Way thick disc”, S. Garbari, J. I. Read, G. Lake, conference “Frontiers in Computational Astrophysics: The Origin of Stars, Planets and Galaxies”, Ascona, Switzerland, 13-18 July 2008.

Programming

Python	very good, frequent usage
IDL, C	basic